

A STUDY OF INHIBITOR - SCALE INTERACTION IN CARBON DIOXIDE  
CORROSION OF MILD STEEL

A thesis presented to

the faculty of the

Fritz J. and Dolores H. Russ  
College of Engineering and Technology  
of  
Ohio University

In partial fulfillment

of the requirement for the degree

Master of Science

Kunal K. Chokshi  
June 2004

This thesis entitled  
A STUDY OF INHIBITOR - SCALE INTERACTION IN CARBON DIOXIDE  
CORROSION OF MILD STEEL

by  
Kunal K. Chokshi

has been approved for  
the Department of Chemical Engineering  
and the Russ College of Engineering and Technology by

Srdjan Nesic  
Professor of Chemical Engineering

R. Dennis Irwin  
Dean, Russ College of Engineering and Technology

CHOKSHI, KUNAL K. M.S. JUNE 2004. Chemical Engineering

A Study of Inhibitor-Scale Interaction in Carbon dioxide Corrosion of Mild Steel

(121pp.)

Director of Thesis: Srdjan Nestic

In the present study, the interaction of inhibitor film and iron carbonate scale in CO<sub>2</sub> corrosion has been investigated using electrochemical techniques. The experiments were designed to see the interaction of the inhibitor film and the iron carbonate scale under various stages of iron carbonate scale growth. The inhibitors used were generic imidazoline based inhibitors. The experiments were conducted in a glass cell at an iron carbonate supersaturation range of 7-150. Different inhibitor concentrations were used at various stages of scale formation.

It is observed that the addition of the inhibitor hinders the corrosion rate as well as hampers the precipitation of the iron carbonate scale. This might be due to the lower concentration of Fe<sup>++</sup> at the metal surface and/or scale inhibition properties of the inhibitor. Under the conditions studied, there was no antagonism between the inhibitor and the iron carbonate scale.

Approved: Srdjan Nestic

Professor of Chemical Engineering

## **DEDICATION**

To

Kamal and Ragini Chokshi (my parents)

and

Nakul Chokshi (my brother)

Who suffered many deprivations to make this work a success

## **ACNOWLEDGEMENTS**

I would like to express my gratitude to Dr. Srdjan Nestic for his confidence in me and his immense patience. Thank you for inspiring me to reach for greater heights and always encouraging me in academics as well as sports (squash). This thesis is a tribute to an exceptional man from a student still anxious to learn from him.

I would like to acknowledge my indebtedness to Dr Daniel Gulino, Dr Sandra Henandez and Dr Martin Kordesch for their invaluable advice.

I would also like to thank the technical staff at the Institute for Corrosion and Multiphase Technology, including Mr. Al Schubert, Mr. Bruce Brown and Mr. John Goettge for their assistance in technical matters, and the research students: Wei Sun, Omkar Nafday, Rama Malka and Shilpha Parakala for providing a wonderful research environment.

Vignesh, Praveen and Indranil, it seems eons since I met you. I thank you for the memories that will keep us laughing for the years to come.

I would also like to acknowledge the contribution of consortium of companies whose continuous financial support and technical guidance made this research possible.

## TABLE OF CONTENTS

DEDICATION .....	4
ACNOWLEDGEMENTS.....	5
TABLE OF CONTENTS.....	6
LIST OF TABLES .....	8
LIST OF FIGURES .....	9
CHAPTER 1: INTRODUCTION .....	13
CHAPTER 2: LITERATURE REVIEW .....	16
2.1 CO <sub>2</sub> corrosion.....	16
2.2 Corrosion product film formation.....	17
2.2.1 Types of corrosion product films .....	17
2.2.2 Effect of Supersaturation .....	19
2.2.3 Effect of Temperature .....	20
2.3 Corrosion inhibitors .....	21
2.3.1 Classification of inhibitors.....	21
2.3.2 Formation of micelles .....	23
2.3.3 Adsorption Phenomena.....	25
2.3.4 Mechanisms of inhibitor action .....	27
2.3.5 Modeling of inhibition .....	28
2.3.6 Mechanisms of imidazoline and amine based inhibitors.....	30
2.4 Scale inhibitors.....	36
2.5 Effect of surface films on inhibitor efficiency .....	39
CHAPTER 3: RESEARCH OBJECTIVES AND TEST MATRIX.....	42
3.1 Research objectives.....	42
3.2 Test Matrix.....	42
CHAPTER 4: EXPERIMENTAL SETUP AND PROCEDURE.....	45
4.1 Method of introduction of Fe <sup>++</sup> .....	47
4.2 Measurement Techniques: .....	48
CHAPTER 5: RESULTS AND DISCUSSIONS .....	51
5.1 Experiments done with only inhibitor.....	51
5.1.1 Inhibitor A.....	51
5.1.2 Inhibitor B.....	54
5.2 Baseline Experiments at different supersaturations without inhibitor .....	59

5.2.1 Experiments at supersaturation of 150.....	59
5.2.2 Experiments at supersaturation of 30.....	62
5.2.3 Experiment at supersaturation of 37 .....	65
5.2.4 Experiment at supersaturation of 7 .....	67
5.2.5 Summary of baseline experiments .....	69
5.3 Inhibitor-scale interactions.....	72
5.3.1 Interactions at supersaturation of 150 .....	72
5.3.2 Interactions at supersaturation of 30 .....	80
5.3.3 Interactions at supersaturation of 7 .....	90
5.4 Analysis and Modeling .....	92
5.4.1 Comparison of the experimental results with the OU model.....	92
5.4.2 Modeling of inhibition .....	95
5.4.3 Modeling of inhibitor-scale interaction .....	97
CHAPTER 6: CONCLUSIONS .....	101
CHAPTER 7: FUTURE WORK .....	102
REFERENCES .....	103
APPENDIX A: METHOD OF ADDITION OF Fe <sup>++</sup> .....	107
APPENDIX B: TAFEL SLOPE ANALYSIS.....	109
APPENDIX C: CORROSION RATE MEASUREMENT .....	111
APPENDIX D: EXPERIMENTAL UNCERTAINTY ANALYSIS .....	112

**LIST OF TABLES**

Table 1. Test Matrix for research.....	42
Table 2. Formulation of inhibitor A.....	43
Table 3. Formulation of inhibitor B.....	44
Table 4. Chemical Composition of X-65 (wt.%) (Fe is in balance).....	44
Table 5. Bulk supersaturation of the solution at various pH and Fe <sup>++</sup> concentration.....	70
Table 6. Summary of baseline experiments at supersaturation 7 – 150, T = 80 °C, no inhibitor, stagnant conditions.....	71

## LIST OF FIGURES

Figure 1. Structure of an inhibitor molecule.....	23
Figure 2. A spherical micelle.....	24
Figure 3. A bilayer micelle .....	25
Figure 4. Equivalent circuit of an electrode filmed with an inhibitor. $R_S$ is solution resistance, $R_{pore}$ is the resistance of the pore areas in the inhibitor film, $C_{film}$ is the capacitance of the film, $R_{ct}$ is charge transfer resistance, $C_{dl}$ is the double layer capacitance (Marco <i>et al.</i> , 2002).....	30
Figure 5. Generalized structures of saturated straight chain imidazolines, amides and amines (Jovancicevic <i>et al.</i> , 1999).....	31
Figure 6. Typical imidazoline molecule (Ramachandran <i>et al.</i> , 1996).....	31
Figure 7. Schematic of a glass cell: 1. Reference electrode; 2. Temperature probe; 3. Luggin capillary; 4. Working electrode; 5. Hot plate; 6. Condenser; 7. Bubbler for gas; 8. pH electrode; 9. Counter electrode.....	46
Figure 8. Comparison of experimental and calculated supersaturation due to passage of anodic current at $T = 20\text{ }^\circ\text{C}$ .....	50
Figure 9. Comparison of experimental and calculated supersaturation due to addition of Ferrous chloride salt at $T = 80\text{ }^\circ\text{C}$ , pH 6.60. ....	50
Figure 10. Effect of inhibitor A concentration on the corrosion rate for pH 6.6, $T = 80\text{ }^\circ\text{C}$ , no $\text{Fe}^{++}$ added, stagnant conditions. ....	52
Figure 11. Polarization curves for 50 ppm inhibitor A at pH 6.6, $T = 80\text{ }^\circ\text{C}$ , no $\text{Fe}^{++}$ added, stagnant conditions. ....	53
Figure 12. Pseudo- Polarization curves for 50 ppm inhibitor at pH 6.6, $T = 80\text{ }^\circ\text{C}$ , no $\text{Fe}^{++}$ added, stagnant conditions. ....	53
Figure 13. Change in corrosion rate with time for different pH at $T = 80\text{ }^\circ\text{C}$ , no $\text{Fe}^{++}$ added, stagnant conditions. ....	56
Figure 14. Change in corrosion rate with time for different inhibitor concentrations for pH 6.00, $T = 80\text{ }^\circ\text{C}$ , no $\text{Fe}^{++}$ added, stagnant conditions. Same symbol shapes depict repetitions of the same experiments. ....	56
Figure 15. Change in corrosion rate with time for different inhibitor concentrations for pH 6.60, $T = 80\text{ }^\circ\text{C}$ , no $\text{Fe}^{++}$ added, stagnant conditions. Same symbol shapes depict repetitions of the same experiments.....	57
Figure 16. Polarization curves for 50 ppm inhibitor B showing the tafel slopes, at pH 6.6, $T = 80\text{ }^\circ\text{C}$ , no $\text{Fe}^{++}$ added, stagnant conditions. ....	57
Figure 17. Potentiodynamic Sweeps for different inhibitor concentrations at pH 6.60, $T = 80\text{ }^\circ\text{C}$ , no $\text{Fe}^{++}$ added, stagnant conditions.....	58
Figure 18. Change in corrosion rate with time for pH 6.60, $\text{Fe}^{++} = 50\text{ ppm}$ , no inhibitor, $T = 80\text{ }^\circ\text{C}$ , SS = 150, stagnant conditions.....	60
Figure 19. Average curve for change in corrosion rate with time for pH 6.60, $\text{Fe}^{++} = 50\text{ ppm}$ , no inhibitor, $T = 80\text{ }^\circ\text{C}$ , SS = 150, stagnant conditions.(For SEM of experiment see Figure 20).....	61

Figure 20. Top view (a) and cross-sectional view(b) of the specimen for pH 6.60, $Fe^{++} = 50$ ppm, no inhibitor, SS = 150, T = 80 °C, stagnant conditions. ....	61
Figure 21. Change in corrosion rate with time for pH 6.60, $Fe^{++} = 10$ ppm, T = 80 °C, SS = 30, no inhibitor, stagnant conditions. ....	63
Figure 22. Adjusted graph for change in corrosion rate with time for pH 6.60, $Fe^{++} = 10$ ppm, T = 80 °C, SS = 30, no inhibitor, stagnant conditions. ....	63
Figure 23. Average curve for the change in corrosion rate with time for pH 6.60, $Fe^{++} = 10$ ppm, SS = 30, T = 80 °C, no inhibitor, stagnant conditions.(For SEM of experiment see Figure 24).....	64
Figure 24. The top view (a) and the cross-sectional view (b) of sample at 500X for pH 6.60, $Fe^{++} = 10$ ppm, no inhibitor, T = 80 °C, SS = 30, stagnant conditions. ....	64
Figure 25. Change in corrosion rate with time for pH 6.30, $Fe^{++} = 50$ ppm, T = 80 °C, SS = 37, no inhibitor, stagnant conditions.(For SEM of experiment see Figure 26) ....	66
Figure 26. The top view (a) and the cross-sectional view (b) of sample at 500X for pH 6.30, $Fe^{++} = 50$ ppm, SS = 37, T = 80 °C, no inhibitor, stagnant conditions. ....	66
Figure 27. Change in corrosion rate with time for pH 6.30, $Fe^{++} = 10$ ppm, T = 80 °C, SS = 7, no inhibitor, stagnant conditions.(For SEM of experiment see Figure 28) ....	68
Figure 28. The top view (a) and the cross-sectional view (b) of sample at 500X for pH 6.30, $Fe^{++} = 10$ ppm, SS = 7, T = 80 °C, no inhibitor, stagnant conditions. ....	68
Figure 29. Effect of supersaturation on corrosion rate at T = 80 °C, no inhibitor, stagnant conditions. ....	70
Figure 30. Effect of addition of 25 ppm inhibitor A added initially on corrosion rate for pH 6.60, $Fe^{++} = 50$ ppm, SS = 150, T = 80 °C, stagnant conditions (For SEM of experiment see Figure 31).....	74
Figure 31. The top view (a) and the cross-sectional view (b) of sample with 25 ppm inhibitor A added immediately, for pH 6.60, $Fe^{++} = 50$ ppm, SS = 150, T = 80 °C, stagnant conditions.....	74
Figure 32. Effect of addition of 50 ppm inhibitor A added initially on corrosion rate for pH 6.60, $Fe^{++} = 50$ ppm, SS = 150, T = 80 °C, stagnant conditions.(For SEM of experiment see .....	75
Figure 33. Comparison of Top view for specimen with 50 ppm inhibitor A and without inhibitor at pH 6.60, $Fe^{++} = 50$ ppm, SS = 150, T = 80 °C , stagnant conditions.....	75
Figure 34. Effect of addition of 25 ppm inhibitor A after 5 hours on corrosion rate for pH 6.60, $Fe^{++} = 50$ ppm, SS = 150, T = 80 °C, stagnant conditions.(For SEM of experiment see Figure 35).....	77
Figure 35. The top view (a) and the cross-sectional view (b) of sample with 25 ppm inhibitor A added after 5 hours for pH 6.60, $Fe^{++} = 50$ ppm, SS = 150, T = 80 °C, stagnant conditions.....	77
Figure 36. Effect of addition of 50 ppm inhibitor A after 5 hours on corrosion rate for pH 6.60, $Fe^{++} = 50$ ppm, SS = 150, T = 80 °C, stagnant conditions. (For SEM of experiment see Figure 37).....	78
Figure 37. Comparison of top view for specimen with 50 ppm inhibitor A added after 5 hours and without inhibitor at pH 6.60, $Fe^{++} = 50$ ppm, SS = 150, T = 80 °C, stagnant conditions.....	78

Figure 38. Comparison of Polarization curves with inhibitor A for pH 6.60, T = 80 °C, stagnant conditions.....	79
Figure 39. Effect of addition of 25 ppm inhibitor B added after 0.5 hr. on corrosion rate for pH 6.60, Fe <sup>++</sup> = 10 ppm, SS = 30, T = 80 °C , stagnant conditions. Same symbol shapes depict repetitions of the same experiments. ....	81
Figure 40. Effect of addition of 25 ppm inhibitor B added after 0.5 hr. on corrosion rate for pH 6.60, Fe <sup>++</sup> = 10 ppm, SS = 30, T = 80 °C , stagnant conditions. Same symbol shapes depict repetitions of the same experiments. ....	82
Figure 41. The Front view of sample at 500X when 25 ppm inhibitor B is added after 0.5 hr for pH 6.60, Fe <sup>++</sup> = 10 ppm, SS = 30, T = 80 °C, stagnant conditions. ....	82
Figure 42. Effect of addition of 10 ppm inhibitor B added after 0.5 hr. on corrosion rate for pH 6.60, Fe <sup>++</sup> = 10 ppm, SS = 30, T = 80 °C , stagnant conditions.....	83
Figure 43. The top view (a) and the cross-sectional view (b) of sample with 10 ppm inhibitor B added immediately, for pH 6.60, Fe <sup>++</sup> = 10 ppm, SS = 30, T = 80 °C, stagnant conditions.....	84
Figure 44. Effect of addition of 25 ppm inhibitor B added after 35 hr. on corrosion rate for pH 6.60, Fe <sup>++</sup> = 10 ppm, SS = 30, T = 80 °C, stagnant conditions. Same symbol shapes depict repetitions of the same experiments. ....	85
Figure 45. Effect of addition of 25 ppm inhibitor B added after 35 hr. on corrosion rate for pH 6.60, Fe <sup>++</sup> = 10 ppm, SS = 30, T = 80 °C, stagnant conditions. Same symbol shapes depict repetitions of the same experiments. ....	86
Figure 46. The Front view (a) and the cross-sectional view (b) of sample at 500X when 25 ppm inhibitor B is added after 35 hr for pH 6.60, Fe <sup>++</sup> = 10 ppm, SS = 30, T = 80 °C, stagnant conditions.....	86
Figure 47. Potentiodynamic sweeps for pH 6.60, Fe <sup>++</sup> = 10 ppm, SS = 30, 25 ppm inhibitor B, T=80°C, stagnant conditions. ....	88
Figure 48. Potentiodynamic sweeps for pH 6.60, Fe <sup>++</sup> = 10 ppm, SS = 30, 25 ppm inhibitor, T = 80 °C, stagnant conditions. ....	88
Figure 49. Pseudo polarization plot when 25 ppm inhibitor B is added after 40 hr for pH 6.60, Fe <sup>++</sup> = 10 ppm, SS = 30, T = 80°C, stagnant conditions. ....	89
Figure 50. Change in corrosion rate with time when inhibitor B is added after 47 hours, at pH 6.30, Fe <sup>++</sup> = 10 ppm, SS = 7, T = 80 °C, stagnant conditions. ....	90
Figure 51. The top view (a) and the cross-sectional view (b) of sample at 500X when 25 ppm inhibitor B is added after 47 hr. for pH 6.30, Fe <sup>++</sup> = 10 ppm, SS = 7, T = 80 °C, stagnant conditions.....	91
Figure 52. Comparison of experimental results with OU model at T=80°C.(Data points indicate experimental results and lines indicate OU model) .....	92
Figure 53. Predicted and experimentally measured iron carbonate scale thickness, at pH = 6.60, Fe <sup>++</sup> = 50 ppm, SS = 150, no inhibitor, T = 80°C. ....	93
Figure 54. Predicted and experimentally measured iron carbonate scale thickness, at pH = 6.60, Fe <sup>++</sup> = 10 ppm, SS = 30, no inhibitor, T = 80°C. ....	93
Figure 55. Predicted and experimentally measured iron carbonate scale thickness, at pH = 6.30, Fe <sup>++</sup> = 50 ppm, SS = 37, no inhibitor, T = 80°C. ....	94

Figure 56. Predicted and experimentally measured iron carbonate scale thickness, at pH = 6.30, $\text{Fe}^{++} = 10$ ppm, SS = 7, no inhibitor, T = 80°C. ....	94
Figure 57. Comparison of the experimental results for inhibitor, with the generalized and simplified Frumkin isotherm.....	96
Figure 58. $\text{Fe}^{++}$ concentration profile with and without the inhibitor obtained using the OU model at pH 6.60, $\text{Fe}^{++} = 50$ ppm, SS = 150, T = 80 °C. ....	99
Figure 59. pH profile with and without the inhibitor obtained using the OU model at pH 6.60, $\text{Fe}^{++} = 50$ ppm, SS = 150, T = 80 °C.....	99
Figure 60. Comparison of the iron carbonate scale obtained (a) with and (b) without inhibitor using the OU model at pH 6.60, $\text{Fe}^{++} = 50$ ppm, T = 80 °C.....	100
Figure 61. A typical linear polarization curve obtained in experiments before scale formation.....	115
Figure 62. A typical linear polarization curve obtained in experiments after scale formation.....	116
Figure 63. Comparison of the calculated and the experimental error at supersaturation of 150 and T = 80 °C.....	120
Figure 64. Comparison of the calculated and the experimental error at supersaturation of 30 and T = 80 °C.....	121

## CHAPTER 1: INTRODUCTION

Carbon dioxide corrosion is a major problem in the oil and gas production industry and can occur at all stages of production from downhole to surface equipment. Corrosion has a huge impact on the oil and gas industry in terms of its effect on capital and operational expenditures and health, safety and environment (Kermani and Morshed, 2003). Hence, one of the major decisions to be made before the well is drilled is the selection for the material of construction for the pipeline. Although there have been many developments in corrosion resistant alloys over the past few decades, mild steel still constitutes an estimated 99% of the material used in the oil industry. It is usually the most cost effective option, being a factor of 3 to 5 times cheaper than stainless steels. Yet, its corrosion resistance is poor in aggressive environments, and the cost savings can only be realized by adding a corrosion inhibitor to the environment or applying a protective coating to the steel. (Roberge, 1999).

A corrosion inhibitor is a chemical substance that, when added in small concentrations to an environment reduces the corrosion rate (Roberge, 1999). Commercial corrosion inhibitors consist of at least one of the following compounds: fatty acids, amides, fatty amides, diamines, fatty amido amines or imidazolines, oxyalkylated amines, quaternary amines, other amine derivatives, and oxygen, sulfur or phosphorus containing compounds (Durnie *et al.*, 2001).

Nitrogen based organic compounds such as imidazolines, amides, amido amines, and amines and their salts have been used successfully as inhibitors in oil field applications. Imidazoline containing products have been used commonly to protect mild

steel in oil and gas wells and pipelines from carbon dioxide corrosion. Despite extensive use of imidazoline inhibitors in continuous and batch oilfields treatments, the mechanism of inhibition remains poorly understood (Jovancicevic *et al.*, 1999).

The key issues regarding the structure-performance relationships of imidazolines and corresponding amides are: the role of the hydrocarbon relative to the imidazoline head group and pendant amine group in film formation, thickness of the imidazoline film (monolayer / bilayer vs. multilayer), stability and persistency of the imidazoline film, solution composition and hydrolysis of imidazoline, interaction of the inhibitor with the iron carbonate scale formed, microstructure dependency on adsorption of imidazoline on steel, flow conditions, operational parameters etc.

Some of these issues have been studied recently using electrochemical techniques like potentiodynamic sweeps, linear polarization resistance (LPR) (Nesic *et al.*, 1995), and electrochemical impedance spectroscopy (EIS) (Tan *et al.*, 1996), adsorption studies (Durnie *et al.*, 2001, Nesic *et al.*, 1995, Zhang *et al.*, 2001, Ramachandran *et al.*, 2001), surface science techniques (second harmonic generation [SHG], time of flight secondary ion mass spectrometry [TOF-SIMS]) (Durnie *et al.*, 2001, Edwards *et al.*, 1994) and molecular modeling (Edwards *et al.*, 1994, Ramachandran *et al.*, 2001).

However, little research has been done to find out the efficiency of the inhibitor in the presence of the iron carbonate scale that is formed due to the change in the operational conditions. Both Nesic *et al.* (1995) and Malik (1995) agreed that the state of the metal surface due to precorrosion was an important factor determining performance of an inhibitor.

It remains to be seen if the interaction of the inhibitor with the scale happens generally in a synergistic fashion and decrease the corrosion rate or whether two seemingly corrosion retarding mechanisms can sometimes interact in an antagonistic fashion and fail to decrease the corrosion rate.

Hence, this project aims at studying the effect of addition of a corrosion inhibitor on the growth of iron carbonate scale and vice-versa, and its effect on the corrosion rate.

## CHAPTER 2: LITERATURE REVIEW

### 2.1 CO<sub>2</sub> corrosion

Carbon dioxide corrosion or “sweet corrosion” of carbon steel is a major problem in the oil and gas industry. The presence of dry CO<sub>2</sub> gas or only oil is itself not corrosive. However, it is the contact of the aqueous phase with the surface of the metal that leads to corrosion and subsequent failures. The basic CO<sub>2</sub> corrosion reactions have been well understood and accepted through the work done in the past few decades. The major chemical reactions include CO<sub>2</sub> dissolution and hydration to form carbonic acid,



It then dissociates into bicarbonate and carbonate ions in two steps:



CO<sub>2</sub> corrosion is an electrochemical reaction with the overall reaction given by:



Thus, CO<sub>2</sub> corrosion leads to the formation of a corrosion product, FeCO<sub>3</sub>, which when precipitated could form a protective or a non-protective scale depending on the environmental conditions.

The electrochemical reactions at the steel surface include the anodic dissolution of iron:



and two cathodic reactions. The cathodic reactions are proton reduction reaction and the direct reduction of carbonic acid.



Despite more than three decades of intense research, it is still not known which of the two reactions actually prevails on the surface. Hence, many have taken the net cathodic current to be the sum of the currents of the two reactions (Gray *et al.*, 1997). It has been suggested (Gray *et al.*, 1990) that the direct reduction of bicarbonate ion becomes important at higher pH.

Having outlined the mechanism, one can anticipate that there are many environmental factors such as solution chemistry, flow velocity, temperature, pressure, pH etc., which determine the corrosion rate of the metal. The formation of the corrosion product scales due to the environmental conditions or presence of the inhibitor film could also have a significant impact on the corrosion rate of the metal.

## **2.2 Corrosion product film formation**

### **2.2.1 Types of corrosion product films**

CO<sub>2</sub> corrosion of a metal is strongly dependent on the type of corrosion product film formed on the surface of the metal during the corrosion process. The stability, protectiveness, precipitation rate and the adherence of these films determine the nature of (localized/ uniform) and the rate of corrosion. Depending on the environmental factors, corrosion films can be divided into following major classes:

a) Iron carbide ( $Fe_3C$ ):

Iron carbide is the undissolved component of the metal, which is left behind after the corrosion process. It is an electronic conductor. Such films are very porous and non-protective (Jasinski, 1986). Iron carbide films can significantly affect the corrosion process by either decreasing the corrosion rate by acting as a diffusion barrier or increasing the corrosion due to (Gulbrandsen *et al.*, 1998):

1. Galvanic coupling of the film to the metal.
2. Increase in the true specimen surface area
3. Acidification of the solution inside the corrosion product film

b) Iron carbonate ( $FeCO_3$ ):

The reaction for formation of solid iron carbonate is given by:



The precipitation of solid iron carbonate occurs when the product of concentrations of  $Fe^{2+}$  and  $CO_3^{2-}$  exceed a certain limit known as the solubility limit. However, the rate of precipitation of iron carbonate is so slow that most often the precipitation kinetics comes into consideration rather than the thermodynamics.

The equation for the rate of precipitation of the iron carbonate ( $R_{FeCO_3(s)}$ ) is given as (Van Hunnik *et al.*, 1996):

$$R_{FeCO_3(s)} = \frac{A}{V} \cdot f(T) \cdot K_{sp} \cdot f(SS) \quad (2-9)$$

Where Supersaturation is defined as:

$$SS = \frac{C_{Fe^{2+}} C_{CO_3^{2-}}}{K_{sp}} \quad (2-10)$$

Since  $CO_3^{2-}$  ion concentration is dependent on the pH, it can be deduced that:

$$SS = f(Fe^{2+}, pH) \quad (2-11)$$

When iron carbonate precipitates at the steel surface, it decreases the corrosion rate by:

- Presenting a diffusion barrier for the species involved in the corrosion process
- Blocking a portion of the steel and preventing electrochemical reactions from occurring (Nesic *et al.*, 2004).

The most important factors affecting the precipitation of iron carbonate are supersaturation and the temperature.

### 2.2.2 Effect of Supersaturation

During the transport the oil and gas in the pipeline, the water phase will accumulate much  $Fe^{++}$  due to corrosion of the pipe wall. So there can be considerable amount of  $Fe^{++}$  in the downstream portion of the pipeline, which could have an influence on the formation of the iron carbonate scale. Increased  $Fe^{++}$  concentration can lead to higher supersaturation, which could not only increase the precipitation rate of iron carbonate but also lead to more protective scale formation.

The increase in pH leads to the increase in the  $CO_3^{2-}$  ion concentration. This in turn leads to the increase in the saturation index that could lead to formation of iron carbonate film (given that the solution is supersaturated).

Hence an increase in the  $Fe^{++}$  ion concentration or pH can lead to a higher supersaturation value that in turn could increase the precipitation rate of iron carbonate and decrease the corrosion rate.

### 2.2.3 Effect of Temperature

The growth of iron carbonate is a very slow temperature dependent process (Johnson and Tomson, 1991, Dugstad, 1992). Increasing in the temperature decreases the solubility of iron carbonate. The precipitation rate increases significantly with temperature. The increase in temperature also leads to acceleration of all the other processes involved in corrosion i.e. electrochemical reactions, chemical reactions, transport of species etc. which leads to increase in the corrosion rate.

The following paragraphs give a brief introduction of the corrosion inhibitors. The work done in the present thesis does not require a deep understanding of the workings of an inhibitor. However, the literature review aims to enlighten the reader with some basics about corrosion inhibitors and make him/her aware of the complications involved in working with inhibitors.

### **2.3 Corrosion inhibitors**

Corrosion inhibitors are widely used in the industry to control corrosion. There are two basic concepts that need to be well understood in order to explain the majority of observed phenomena. These are adsorption of an inhibitor on a surface and the formation of micelles in the solution. These two phenomena differentiate an inhibitor from other chemical entities. The adsorption on the metal surfaces is responsible for the surface-active properties like dispersion and the micelles are responsible for the bulk properties like viscosity and solubility. These two phenomena are introduced in the following paragraphs followed by a literature review on the mechanisms of imidazoline and amine based inhibitors.

#### **2.3.1 Classification of inhibitors**

Various authors have classified inhibitors differently. Some authors, for example, prefer to group inhibitors by their chemical functionality. However, by far the most popular organization scheme consists of grouping corrosion inhibitors in a functionality scheme as follows (Roberge, 1999):

a) Passivating inhibitors

They cause a large anodic shift of the corrosion potential, forcing the metallic surface into the passivation range. Their disadvantage is that they can cause pitting and can accelerate corrosion when the concentration goes beyond the passivation range.

b) Cathodic inhibitors

Cathodic inhibitors either slow the cathodic reaction itself or selectively precipitate on cathodic areas to increase the surface impedance and limit the diffusion of reducible species to these areas.

c) Organic inhibitors

Both anodic and cathodic effects are sometimes observed in the presence of organic inhibitors; however, as a general rule, organic inhibitors affect the entire surface of a corroding metal when present in sufficient concentration. Organic inhibitors, usually designated as 'film-forming', protect the metal by forming a hydrophobic film on the metal surface. The effectiveness of these inhibitors depends on the chemical composition, their molecular structure, and their affinities for the metal surface.

d) Precipitation inhibitors

Precipitation inducing inhibitors are film-forming compounds that have a general action over the metal surface, blocking both anodic and cathodic sites indirectly. Precipitation inhibitors are compounds that cause the formation of precipitates on the surface of the metal, thereby providing a protective film. However, protection is not always reliable and depends heavily on pH and a saturation index that depends on water composition and temperature

#### e) Volatile corrosion inhibitors

These are also called vapor phase inhibitors. They are organic compounds characterized by small vapor pressures from 0.013 to 66.66 Pa. They include inhibitors for steam and vapor zones in closed systems. On contact with the metal surface, the vapor of this inhibitor condenses and moisture hydrolyzes it to liberate protective ions. It is desirable, for an efficient volatile corrosion inhibitor, to provide inhibition rapidly while lasting for long periods. Both qualities depend on the volatility of these compounds, since fast action requires high volatility while enduring protection requires low volatility.

#### 2.3.2 Formation of micelles

An inhibitor is a surface-active agent. A surface-active molecule consists of two parts with opposing characteristics (Figure 1). One part is hydrophilic and the other is hydrophobic. All the characteristic properties of an inhibitor originate from the fact that a hydrophobic group (usually a hydrocarbon chain) is forced to dissolve into water by the hydrophilic group that is attached to the same molecule. Inhibitor molecules have a tendency to associate with one another at the interfaces and in the solution.

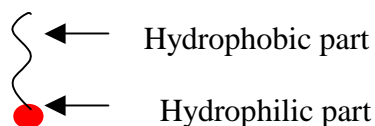


Figure 1. Structure of an inhibitor molecule.

When the inhibitor concentration is very low, the inhibitor molecules tend to remain isolated as monomers in the solution. As the inhibitor concentration increases, the monomers tend to aggregate at the interfaces that include metal-water and oil-water or air-water. This results in a lower surface tension. There is some repulsion between charged hydrophilic groups. Due to repulsion, they tend to move away from each other. As the amount of inhibitor increases, since they cannot move away from each other due to space limitations, they aggregate into spherical structures called micelles (Figure 2). The concentration at which these micelles form is called the Critical Micelle Concentration (CMC). The interior of the micelle resembles the hydrophobic part of the molecule and the exterior part is the hydrophilic part.

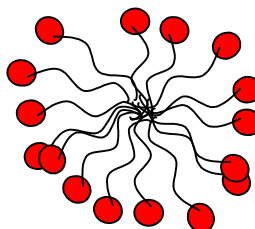


Figure 2. A spherical micelle.

As the CMC is achieved, the concentration of the individual, nonaggregated molecules is at its maximum value, since any additional inhibitor molecules that may be added to the system will be incorporated into micelles. Above the CMC there is an abrupt change in most of the properties of the liquids, such as surface tension, solubility of oils in the aqueous phase, and viscosity. The CMC marks an effective boundary condition

below which inhibitor concentration is typically below the monolayer level on the metal surface, and above which adsorption at the metal surface consists of multiple layers of inhibitor.

Usually just above the CMC micelles are common structures, but as the concentration goes on increasing, since the available space decreases further, the shape of the structures changes to different forms like lamellar, cylindrical, bilayers, and inverted. Some of the factors on which the shape of the micelle depends are the relative sizes of the hydrophobic and hydrophilic group, cohesive energy of the molecules and the concentration of the inhibitor (Israelachvili, 1985, Arie Ben-Naim, 1980, Porter, 1991).

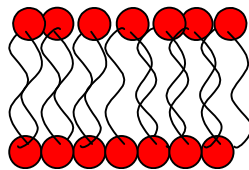


Figure 3. A bilayer micelle

### 2.3.3 Adsorption Phenomena

It is generally assumed that the first stage in the action mechanism of the inhibitor in acid media is the adsorption of the inhibitors onto the metal surface. The process of adsorption is influenced by the nature and the surface charge of the metal, by the chemical structure of the organic inhibitor, and by the type of the electrolyte. Adsorption occurs because of the interaction energy between inhibitor and the metal surface is higher than interaction energy between water molecules and the metal surface. The principal

types of interaction between an organic inhibitor and the metal surface are (Mansfeld 1987):

a) Physical (electrostatic) adsorption

Physical adsorption is the result of the electrostatic attractive forces between inhibiting organic ions or dipoles and electrically charged surface of the metal. Inhibiting species that undergo physical adsorption interact rapidly with the surface, however they can also be removed easily from the surface. Physical adsorption is relatively independent of temperature. It depends on:

- Structural parameters, such as hydrocarbon chain length and the nature and position of substituents in aromatic ring.
- Electrical characteristics of inhibitors. i.e. charge of the hydrophilic group.
- Type of ions present in the solution
- Potential of the metal

b) Chemisorption.

This process involves charge sharing or charge transfer from inhibitor molecules to the metal surface in order to form a coordinate bond. The chemisorption process takes place more slowly than the physical adsorption and with higher activation energy. It depends on the temperature. It is specific for certain metals, and it is not completely reversible. There are many theories postulated to explain this phenomenon.

#### 2.3.4 Mechanisms of inhibitor action

When inhibitor is adsorbed, it retards the cathodic, anodic or both the reactions. This action occurs by following mechanisms (Mansfeld 1987):

a) Changes in the electrical double layer:

Corrosion inhibition related to changes in the structure of the electrical double layer at the metal/solution interface takes place because of electrostatic adsorption of ionized inhibiting species.

b) Formation of a physical barrier

Inhibitors are able to form a multimolecular layer on the metal surface. The resulting barrier action is independent of the nature of the adsorption forces between inhibitor molecules and the metal surface. The formed layer slows down diffusion of the ions to and from the metal surface. The hindering of the mass transport causes inhibition of the corrosion reaction.

c) Reduction of metal reactivity

According to this mechanism, the inhibitor adsorbs on sites active with respect to the partial electrochemical reactions. A reduction of either the anodic or the cathodic reaction or both arises from blockage of the corresponding sites.

d) Participation of inhibitors in reactions

According to this mechanism, the adsorbed inhibitor may participate in the intermediate formation, promoting a decrease or stimulation of the electrode reaction depending on the stability of the adsorbed surface complex.

### 2.3.5 Modeling of inhibition

Inhibitors are usually modeled by the following ways:

#### a) Adsorption Isotherms

Adsorption isotherms are used to describe the efficiency of the inhibitors. This is an extremely useful method for assessing the suitability of inhibitors to be used under specific conditions.

Adsorption isotherms mostly used to characterize inhibitor performance are (Ramachandran *et al.*, 2001):

- Langmuir :

Langmuir isotherm is given by the following equation :

$$Kc = \frac{\theta}{1 - \theta} \quad (2-13)$$

Where,  $\theta$  -surface coverage

K- Equilibrium constant

c - Concentration of inhibitor

The Langmuir adsorption isotherm assumes that only monolayer coverage is possible and there are no interactions taking place between adjacent molecules. Both of these conditions are not strictly satisfied for the corrosion inhibitors .Yet this adsorption isotherm has been used often in modeling of inhibitors.

- Temkin.

Temkin isotherm is given by the following equation :

$$Kc = \exp(-g\theta) \quad (2-14)$$

Where , g- characterizing inhibitor interaction with each other.

- Flory-Huggins

Flory-Huggins isotherm is given by the following equation :

$$Kc = \frac{\theta}{(1-\theta)^x} \quad (2-15)$$

Where- x-number of desorbed water molecules replaced by inhibitor

- Frumkin.

Frumkin isotherm is given by the following equation :

$$Kc = \frac{\theta}{(1-\theta)} \times e^{-f\theta} \quad (2-16)$$

Where f- characterizing inhibitor interaction with each other.

#### b) Equivalent circuits

Electrochemical impedance spectroscopy (EIS) is also used by some researchers to study film formation and destruction and the corrosion protection mechanism of a corrosion inhibitor. It involves simulation of the impedance characteristics of the electrode surface by an electrical circuit. Tan *et al.* (1996) and Marco *et al.* (2002) have also reported that it could prove to be a valuable technique for evaluating the film persistency of corrosion inhibitor. An example of an equivalent circuit is shown in Figure 4.

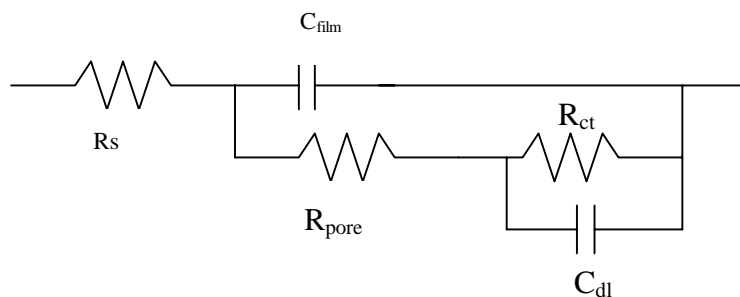


Figure 4. Equivalent circuit of an electrode filmed with an inhibitor.  $R_s$  is solution resistance,  $R_{pore}$  is the resistance of the pore areas in the inhibitor film,  $C_{film}$  is the capacitance of the film,  $R_{ct}$  is charge transfer resistance,  $C_{dl}$  is the double layer capacitance (Marco *et al.*, 2002).

### 2.3.6 Mechanisms of imidazoline and amine based inhibitors.

The most commonly used inhibitors for protecting mild steel oil and gas pipelines are nitrogen-based organic surfactants, such as imidazolines, amides, and amines and their salts (Jovancicevic *et al.*, 1999). The structure of imidazolines, amides, and the amines are shown in the Figure 5.

The imidazoline molecule consists of the following: (i) an imidazoline head group, (ii) a long hydrocarbon tail group, and (iii) a short pendent group. It is illustrated in the Figure 6

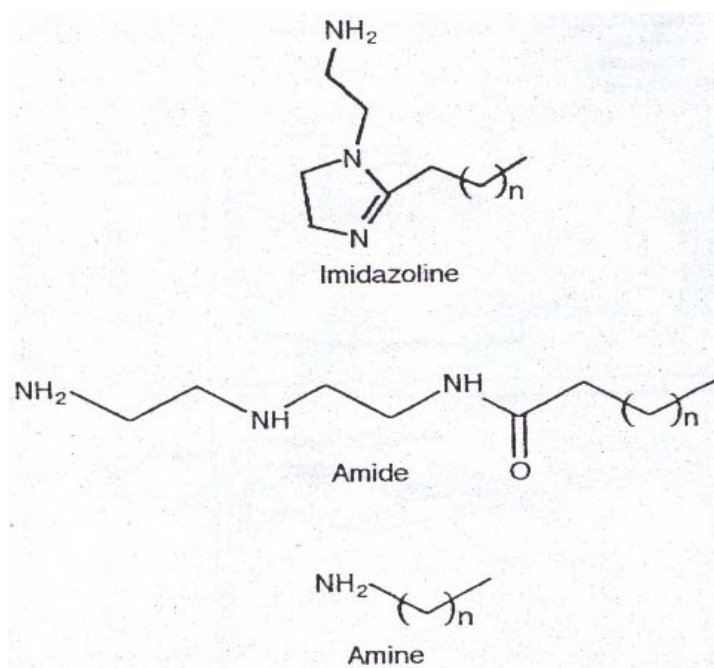


Figure 5. Generalized structures of saturated straight chain imidazolines, amides and amines (Jovancicevic *et al.*, 1999).

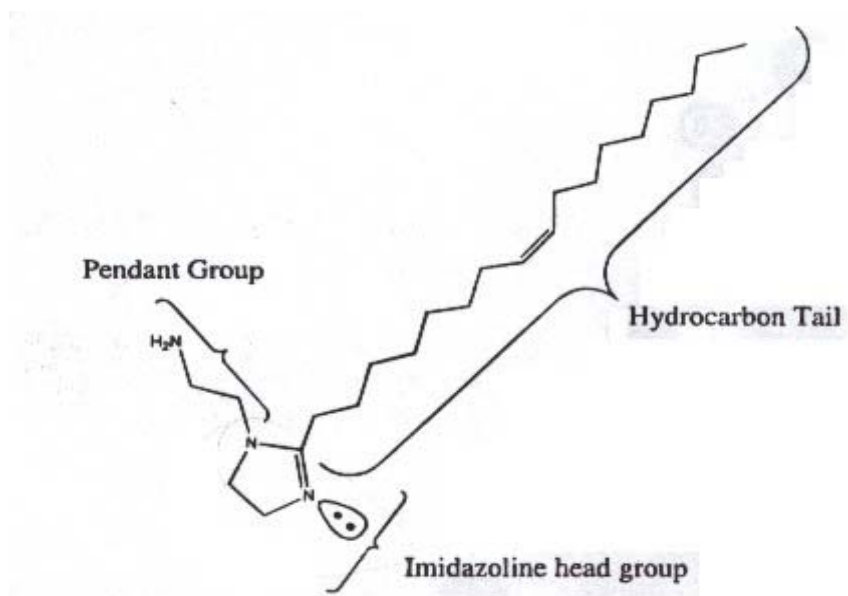


Figure 6. Typical imidazoline molecule (Ramachandran *et al.*, 1996).

Researchers have observed that many aliphatic amines act as corrosion inhibitors. Hence, the prevalent theory on the mechanisms of imidazolines as a corrosion inhibitor proposed that the lone pair of electrons on the amine group on the pendent side chain was determining the molecule adsorption and anchoring it to the surface. The ring structure was potentially opening to provide a second amine to bond with the surface thereby explaining the better corrosion inhibition over single amine inhibitor. The long hydrocarbon chain was interpreted as being hydrophobic in nature and driving the molecule to the surface as well as acting as barrier to water and corrosion products (Edwards *et al.*, 1994).

a) Effect of Hydrocarbon chain

Almost all the researchers seem to believe that the long hydrocarbon chain is playing a major role in the role of imidazolines and amines as corrosion inhibitors. Jovancicevic *et al.* (1999) showed through experiments that hydrocarbon chain length was extremely important over a range of C<sub>8</sub> – C<sub>20</sub> in the corrosion inhibition of imidazolines. This was in sharp contrast with the results of Ramachandran *et al.* (1996) where little effect of hydrocarbon chain length above C<sub>12</sub> on corrosion inhibition was found. He explained this effect of hydrophobic group on the inhibitor film formation by a substantial increase in the bilayer cohesive energy with the hydrocarbon chain length above C<sub>8</sub>. The low activity of C<sub>8</sub> imidazoline could be rationalized in terms of the formation of small spherical micelles in the solution and the formation of a non-uniform

film. Because of its low cohesive energy, C<sub>8</sub> imidazoline would not be expected to form a bilayer.

b) Effect of Branching

Edwards *et al.* (1994) investigated the effect of packing of the chain by branching it. However, they found out that the branched chain was just as effective as straight chained imidazoline. They wrote “the presence of the two short chains caused through mutual repulsion, a large volume to be occluded by the chains when compared to the single chain on imidazoline. From this it was inferred that the larger swept volume of the branched chain causes more of a barrier per head group than the straight chain version.” It was predicted that a marginally lower concentration would be required to form a monolayer. However Ramachandran *et al.* (1996) wrote in contrast, that Alkane chains are the closest packed and hence they would prevent ingress of the water molecules. Edwards *et al.* (1994) also concluded that the hydrocarbon chain does not drive molecules to the surface since it was found that strength and the rate of adsorption was similar for different chain lengths.

c) Effect of Pendent Group

“The pendent side chain was thought to be anchoring the molecule to the metal surface through the lone pair of electron on the nitrogen in the amine group and was therefore thought to be an integral to the mechanism of the adsorption of the molecule” (Edwards *et al.*, 1994). Most imidazolines corrosion inhibitors have a short pendent group, e.g. -CH<sub>2</sub>-CH<sub>2</sub>-X, where X is polar (X= NH<sub>2</sub> or OH). These polar groups can

form donor-acceptor bond (this involves a lone pair of O or N coordinating to the Fe). However, replacement of the amine group by an alkyl group did not decrease the inhibition efficiency. From this it was concluded by Edwards *et al.* (1994) that pendent side chain is required to improve the effectiveness of the molecule. Hence, from the changes made to the pendent side chain, it was shown that although a pendent chain was necessary, its size, in terms of number of carbon atoms, and the actual chemistry did not play a crucial role in the effectiveness of the inhibitor. So it was inferred that the five-membered ring was playing a major part in the adsorption of the molecule to the surface (Edwards *et al.*, 1994).

Ramachandran *et al.* (1997) noticed that the replacement of the pendent group with an alkyl group works nearly as well as an amine group, but replacement by H leads to a dramatic decrease in the corrosion inhibitor efficiency. Since the change in the binding energy did not lead to the large decrease in the inhibition efficiency, the reason cited for this effect was that effect of the pendent group might be to restrict the conformation of the hydrocarbon chain. "Free motion of the tail made it easier for the water to diffuse into a position on the surface between two adsorbed tails. Attachment of the pendent group to an inhibitor molecule drastically restricts the rotation of the hydrocarbon chain. Thus with the pendent group, an inhibitor molecule bound to a surface has its tail locked into position. This could be important for corrosion inhibition." (Ramachandran *et al.*, 1997)

#### d) Effect of Head Group

It was found that under the same conditions, imidazoline was substantially less effective in terms of MEC (Minimum Effective concentration-the concentration at which corrosion rate reached a steady-state plateau is reached) than amide and amine. However in long-term tests, the differences in the activity was expected to be much smaller (Jovancicevic *et al.*, 1999). Edwards *et al.* (1994) showed that cyclised version is a better performer than the uncyclised. The ring structure was obviously playing an important part in the mechanism of imidazoline. Edwards *et al.* also proposed that the ring lay flat on the surface and bonded to the metal through the nitrogen in the ring. This was supported by the fact that removal or substitution of the pendent side group did not affect the adsorption process or corrosion efficiency to a significant extent.

\* \* \*

In summary, there is little doubt that the inhibitors are widely used, since corrosion causes enormous industrial expense leading to a large market for corrosion inhibitors. Formulations using inhibitors, particularly mixtures of inhibitors have been devised by trial and error, and theory has followed to explain the observed results. After nearly half a century of intensive research on inhibitors, the mechanism by which these chemical compounds prevent corrosion is not understood. The experimental evidence in support of specific mechanisms becomes difficult because of the complexity of the general corrosion process and due to small amounts in which inhibitors are added.

## 2.4 Scale inhibitors

From the experimental results obtained, it was speculated that the inhibitor could be behaving as both a corrosion inhibitor as well as a scale inhibitor. Hence a brief literature review of the scale inhibitors is presented.

Scale inhibitors are chemicals that, when added, can effectively retard the precipitation of sparingly soluble salts from highly supersaturated solutions. As for corrosion inhibitors, the mechanisms of workings of scale inhibitors are not yet understood. However, some mechanisms proposed over a past few decades are briefly described in the following paragraphs

A few mechanisms proposed to explain the inhibition of precipitation and crystal habit modification for the precipitation of strontium sulfate in presence of inhibitors were:

- Adsorption growth-sites theory (Miura et al.)
- The stationary model of adsorption on active centers (Otani, 1960) and
- The more sophisticated dynamic adsorption mechanism (Naono 1967).

However, several inconsistencies were found in the above models (Sarig, 1972). A different view of the influence of the minor component on the retardation of crystal growth and its role in crystallization phenomenon in general, was put forward by Glasner et al.(1968).

According to Glasner's so-called mechanism of active hetero-nucleators, the active minor component acts as a nucleator either in a form of a complex or a polymeric species. This means that the nuclei of the main component are held together around the

inhibitor species by Coulombic attraction without forming a covalent bond. This small entity is known as an ion pair. The deposition of an additional ion pair requires less energy than the energy of formation of entirely new three-dimensional nucleus, and is therefore preferred. The whole supersaturation is condensed in such nuclei. The number of nuclei and their mean size is thus determined by the concentration of the inhibitors. These nuclei consisting of several hundreds or thousands of ion pairs do not precipitate; they form a solution of nuclei and thus the supersaturation is stabilized (Sarig, 1974).

Scale inhibition due to the formation of complexes of the inhibitors with the cations present in aqueous media, which impeded the supersaturation and consequently reduced the nucleation and crystal growth, was proposed by Zielinski (1981). However, Amjad (1987) dismissed the mechanism of an inhibitor forming a stable complex by stating that even at the highest inhibitor concentration, the percentage of the metal ion complexed accounted to less than 5% of the total metal. Based on his findings he concluded that the decrease in the rate of precipitation must be due to surface adsorption at active growth sites

It has generally been accepted that the inhibition of scale formation is influenced by both location of adsorbed inhibitor at the crystal surface and the extent of chemical bonding of the surface (Zhang et al., 1990, Zieba et al., 1996). The inhibitor may be adsorbed on the crystal either generally or at the active growth sites. If the size of the inhibitor is similar to the growth unit, three types of crystal surface sites, having different binding energies, are available for adsorbing inhibitor molecules. In the order of decreasing bond strength, they are kinks, steps and terraces. When occupied by inhibitors,

kinks are at least temporarily poisoned or inactivated. Lattice ions cannot be integrated into these kinks until inhibitor molecules are desorbed. This decrease in the number of active kink sites leads to the decrease in the integration controlled growth rate.

Some researchers (Xyla et. al., 1991, Shiliang et al., 1999, Mueller et. al., 1993) also concluded that this mechanism resulted in retardation of the rates of precipitation and longer nucleation periods (time elapsed between the creation of supersaturation and the first appearance of a new phase (Shiliang et al., 1995)). Shiliang et al. (1995) inferred that the reduction in the precipitation rate was due to the increase of interfacial tension between the salt and the solution. Based on their study, Zieba et al. (1996) stated that the degree of protonation of the inhibitors was important in determining their influence on crystal growth.

From the above discussion, it is observed that fundamentals of scale inhibition mechanism are inadequately understood (Shiliang et al., 1999) and literature provides very little guidance on the expected performance of a scale inhibitor.

## 2.5 Effect of surface films on inhibitor efficiency

The surface of the metal is not always clean when the inhibitor is applied. In CO<sub>2</sub> corrosion, there is formation of either some iron carbide films or iron carbonate scale on the surface due to the corrosion process. Hence, depending on the time when the inhibitor is added, the presence of the corrosion films could affect the working of the inhibitor. In spite of this, very little research has been devoted to study of corrosion inhibition of the metal covered with corrosion product layers. The work done can be divided into two categories:

### a) Effect of carbide films on Inhibitor efficiency

Gulbrandsen *et al.*, (1998) observed that inhibitor performance was impaired with increasing precorrosion time and increasing temperature. The inhibitor problems were attributed to the presence of the iron carbide layer at the steel surface. Hence, the longer the precorrosion time, the thicker the iron carbide film would grow and more severely the inhibitor performance was impaired. However, the failure of the inhibitor was not due to transportation of the inhibitor to the metal surface. One reason cited for inhibitor failure was that the high metal dissolution rates locally due to the corrosion process could prevent the slowly adsorbing inhibitors from adsorbing onto the metal surface and protect it from corrosion. This phenomenon is described by the electromechanical inhibitor desorption model of Drazic V. and Drazic D. (1990).

b) Effect of iron carbonate scales on Inhibitor efficiency

Nesic *et al.*, (1995) observed that in the presence of iron carbide as well as iron carbonate films the performance of an imidazoline-based inhibitor was very poor. They concluded that it was the changes in the metal surface due the precorrosion, which was responsible for the weaker performance of the inhibitor rather than the film itself acting as a diffusion barrier for the inhibitor. Malik (1995) conducted a study to see the effect of an amine based inhibitor on the surface films. He found that in the presence of iron carbonate films, lower concentrations of inhibitor seemed to work better than the higher concentrations. He also found that in the presence of inhibitor, there was a transformation of the surface structure of iron carbonate. However, his study also had a few inconsistencies. All the experiments were done at room temperature, where the precipitation rate of iron carbonate is very slow. Hence, the surface of the metal would have been dominated by iron carbide films rather than iron carbonate films. To explain his results, he assumed local acidification due to the hydrolysis of  $Fe^{++}$  to form hydrogen ions. However, from the Pourbaix diagrams (Jones, 1996), the  $Fe^{++}$  concentration required at a given pH for hydrolysis reaction of  $Fe^{++}$  to  $FeOH^+$  to be thermodynamically feasible, is given by:

$$\log(Fe^{++}) = 13.3 - 2pH \quad (2-17)$$

From the above equation, it can be calculated that at the pH 6.5, Malik was working with, it would require more than 100,000 ppm of  $Fe^{++}$  for this reaction to take place. Hence, the subsequent mechanism proposed is not valid.

From the preceding discussion, a lack of understanding regarding the interaction between the iron carbonate scale and inhibitor is evident. In addition, the necessity to investigate the effect of presence of iron carbonate scale on inhibitor film and vice versa is realized.

## CHAPTER 3: RESEARCH OBJECTIVES AND TEST MATRIX

### 3.1 Research objectives

Based on the previous research, the principal questions that need to be asked are:

1. How do iron carbonate scale and the inhibitor film interact with each other?

Would there be any conditions under which scale and inhibitor film would antagonize each other and fail to decrease the corrosion rate, or would scale and the inhibitor film act synergistically?

2. What is the effect of the inhibitor film on iron carbonate scale formation and vice versa.

### 3.2 Test Matrix

The following test matrix was defined to answer the above questions.

Table 1. Test Matrix for research

Steel Type	X-65
Solution	1% NaCl
T (°C)	80
P <sub>CO2</sub> (bar)	0.54
Rotational velocity (rpm)	0
pH	6.0 – 6.6
Fe <sup>++</sup> concentration (ppm)	10 – 50

The experiments were designed to see the interaction under different iron carbonate precipitation rates and different inhibitor concentration. The supersaturation was varied from 7 to 150 by selecting various pH and the Fe<sup>++</sup> concentrations.

The chemical composition of the X-65 used for all the experiments is shown in Table 4. Two types of inhibitors were used for the experiments (Table 2 and Table 3). The inhibitors chosen were generic inhibitors with known formulation and were decided by the consortium of companies sponsoring research at the Institute for Corrosion and Multiphase Technology, and were provided to us by Champion Technologies Inc.

Table 2. Formulation of inhibitor A

<b>Compound</b>	<b>Composition (by weight)</b>
Methanol	25%
Water	25%
Imidazoline acetate salts	25% (1:1 DETA/Tall oil imidazoline neutralized to pH 5.0)
Benzyl dimethyl coco-quat chloride	25%

Table 3. Formulation of inhibitor B

<b>Compound</b>	<b>Composition (by weight)</b>
Isopropyl alcohol	35%
Water	35%
Imidazoline acetate salts	30% (1:1 DETA/Tall oil imidazoline neutralized to pH 5.0)

Table 4. Chemical Composition of X-65 (wt.%) (Fe is in balance)

Al	As	B	C	Ca	Co	Cr	Cu	Mn	Mo	Nb
0.0032	0.005	0.0003	0.050	0.004	0.006	0.042	0.019	1.32	0.031	0.046
Ni	P	Pb	S	Sb	Si	Sn	Ta	Ti	V	Zr
0.039	0.013	0.020	0.002	0.011	0.31	0.001	0.007	0.002	0.055	0.003

## CHAPTER 4: EXPERIMENTAL SETUP AND PROCEDURE

The experiments were done in a glass cell (Figure 7). A saturated Ag/AgCl reference electrode used externally was connected to the cell via a Luggin capillary and a porous wooden plug. A concentric platinum ring was used as a counter electrode. Each glass cell was filled with 2 liters of distilled water and 1% wt. NaCl. The solution was then heated to 80 °C and purged with 1.0 bar CO<sub>2</sub> gas. After the solution was deoxygenated, the pH was increased from the equilibrium pH 4.18 to the desired pH by adding a deoxygenated sodium bicarbonate solution. Later the required amounts of Fe<sup>2+</sup> were added in the form of a deoxygenated ferrous chloride salt (FeCl<sub>2</sub>·4H<sub>2</sub>O) solution. Then the working electrode was inserted into the solution and the measurements were taken. Prior to immersion, the carbon steel specimen surfaces were polished with 240, 400 and 600 grit SiC paper, rinsed with alcohol and degreased using acetone.

Electrochemical corrosion measurements were performed by using a potentiostat connected to a PC. Corrosion rates were measured by using the linear polarization resistance (LPR) method. The coupon with the iron carbonate scale on it was observed using Scanning Electron Microscopy (SEM).

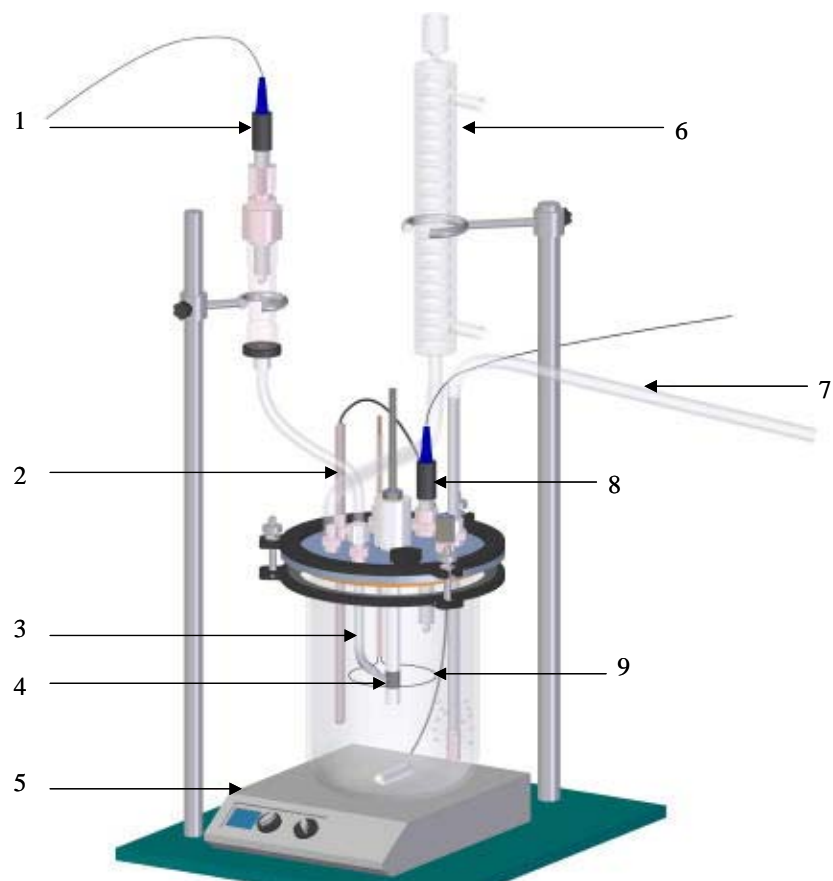


Figure 7. Schematic of a glass cell: 1. Reference electrode; 2. Temperature probe; 3. Luggin capillary; 4. Working electrode; 5. Hot plate; 6. Condenser; 7. Bubbler for gas; 8. pH electrode; 9. Counter electrode

#### 4.1 Method of introduction of Fe<sup>++</sup>

As discussed in the literature review, the rate of precipitation of iron carbonate is slow and the precipitation kinetics is important. Hence, it would take a lot of time to form an iron carbonate film under lower supersaturations. So a method for increasing the rate of iron carbonate precipitation was needed.

The equation for the rate of precipitation of the iron carbonate is shown in equation (2-9). From the equation (2-10), it is seen that to increase the precipitation rate either the Fe<sup>++</sup> concentration or CO<sub>3</sub><sup>2-</sup> concentration or both need to be increased in a controlled way.

Nesic and Lee (2002) tried to use steel wool in their experiments to increase the Fe<sup>++</sup> concentration, however the concentration of Fe<sup>++</sup> in the solution cannot be controlled by using this method, since the exact amount of Fe<sup>++</sup> that dissolves in the solution is not known.

Another method to increase the Fe<sup>++</sup> concentration was by artificially corroding the mild steel sample by passing anodic current through it. The amount of Fe<sup>++</sup> released was calculated using the equation given by Faraday's Law.

$$m = \frac{Ita}{nF} \quad (3-1)$$

where,

$m$  is mass in gram,  $I$  is current in Amperes,  $a$  is atomic weight,  $n$  is number of equivalents exchanged (For Fe<sup>++</sup>,  $n=2$ ),  $F$  is Faraday's constant (96500 coulombs/equivalent).

The amount of  $\text{Fe}^{++}$  can be indirectly determined by measuring the change in the pH of the solution. From the experiments, it was found that this method could only be used until a certain level of supersaturation ( $\approx 10$ ) and pH (5.5) is attained (Figure 8). Beyond which an iron carbonate film is formed on the surface of the sample and the release of the  $\text{Fe}^{++}$  ions can neither be controlled nor predicted.

Finally, the method that worked for us was to introduce ferrous chloride salt ( $\text{FeCl}_2 \cdot 4\text{H}_2\text{O}$ ). In this way, very large supersaturations could be achieved in a controlled manner. From the Figure 9, it is seen that below supersaturations of 1000, the  $\text{Fe}^{++}$  ions added in the solution (method of addition is shown in Appendix A) is approximately equal to the  $\text{Fe}^{++}$  ions measured using the cuvettes. Since higher supersaturations could be achieved using this method, this method of addition of  $\text{Fe}^{++}$  ions was used.

#### **4.2 Measurement Techniques:**

All corrosion potential and rate measurements were made using a Gamry PC4 monitoring system and analyzed using the accompanying software. The electrochemical methods used to measure the corrosion rate are as follows:

- The linear polarization resistance (LPR) technique is used to monitor the *in-situ* corrosion rate. The equations used to calculate the corrosion rate using LPR are shown in Appendix C. The sample was polarized at  $\pm 5$  mV around the corrosion potential during the LPR measurement. The resistance measured using the LPR technique was the total resistance and it needs to be compensated for the solution resistance by using the electrochemical impedance spectroscopy (EIS) technique.

- In the potentiodynamic polarization technique, the metal electrode is polarized over a larger potential (200 mV and 600 mV above and below the corrosion potential) at a constant rate (0.2 mV/s).

The experimental uncertainty analysis due to the inherent error in the instrument was done. The comparison of the calculated error and the experimental error is shown (Uncertainty analysis is explained in detail in appendix D).

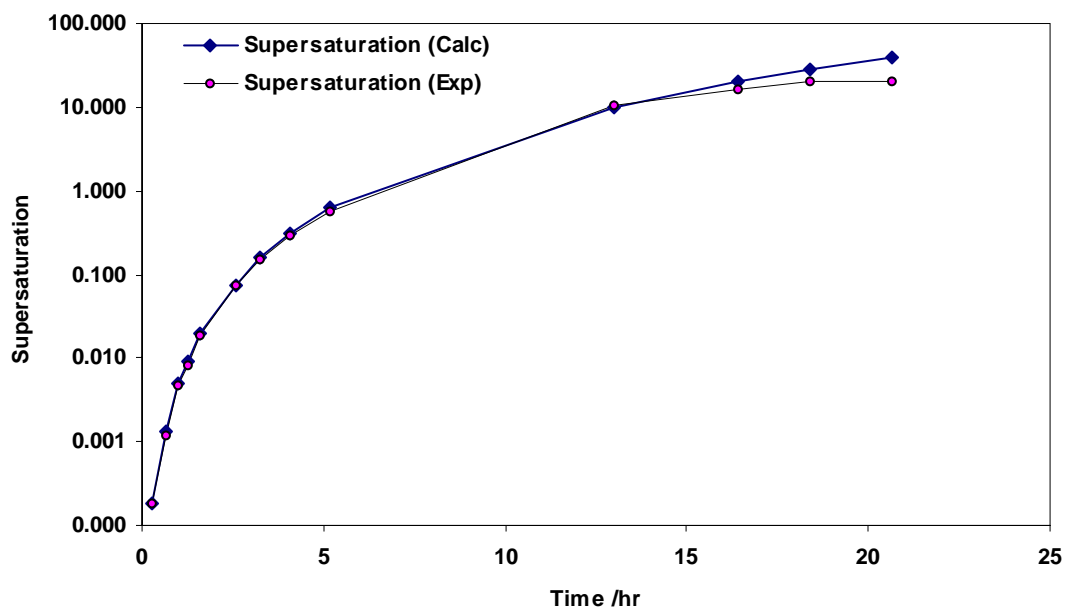


Figure 8. Comparison of experimental and calculated supersaturation due to passage of anodic current at  $T = 20\text{ }^{\circ}\text{C}$ .

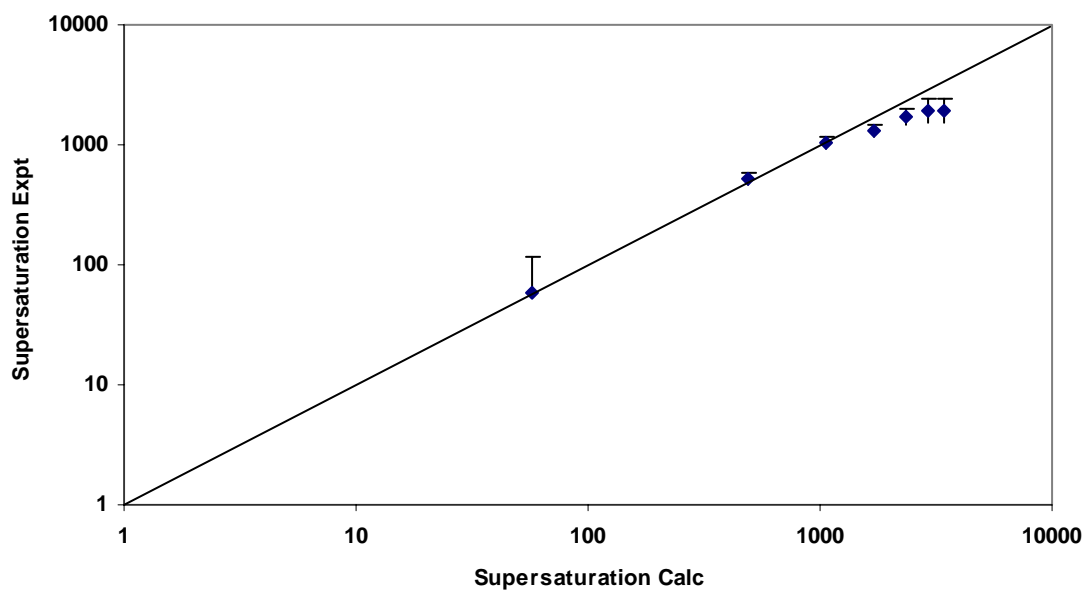


Figure 9. Comparison of experimental and calculated supersaturation due to addition of Ferrous chloride salt at  $T = 80\text{ }^{\circ}\text{C}$ , pH 6.60.

## CHAPTER 5: RESULTS AND DISCUSSIONS

The experimental results obtained are presented below in the following manner:

- Experiments done with only inhibitor A and inhibitor B and no  $\text{Fe}^{++}$  added.
- Experiments done at different supersaturations and no inhibitor added.
- Experiments done at different supersaturations with addition of inhibitors.
- Interpretation of results.
- Modeling.

### 5.1 Experiments done with only inhibitor

These set of experiments were designed to see the effect of inhibitor concentration on the corrosion rate under non-scaling conditions.

#### 5.1.1 Inhibitor A

The effect of inhibitor A concentration on the corrosion rate is shown in Figure 10. From the figure, it can be seen that at 25 ppm the inhibitor is partially protective, while it decreases the corrosion rate by more than 80% at 50 ppm.

From the potentiodynamic sweeps (Figure 11), the values of the Tafel slopes were measured to be  $\beta_a = 62$  mV/decade,  $\beta_c = 98$  mV/decade and the 'B' value was calculated to be 16.4 mV. From the sweeps, it can be seen that the inhibitor slows down the anodic reaction as well as the cathodic reaction.

Figure 12 shows the "pseudo polarization" plot in which the corrosion potential is plotted against the corrosion current on the top of the potentiodynamic sweeps. From

this plot, it can be seen that as soon as 50 ppm inhibitor A is added, initially there is a jump in the potential accompanied by a small decrease in the corrosion current. Subsequently the corrosion current decreases while the potential is almost the same. Hence, it can be concluded that initially inhibitor A retards the anodic reaction more than the cathodic, without much effect on the corrosion rate followed by a retardation of both reactions leading to a decrease in the corrosion rate.

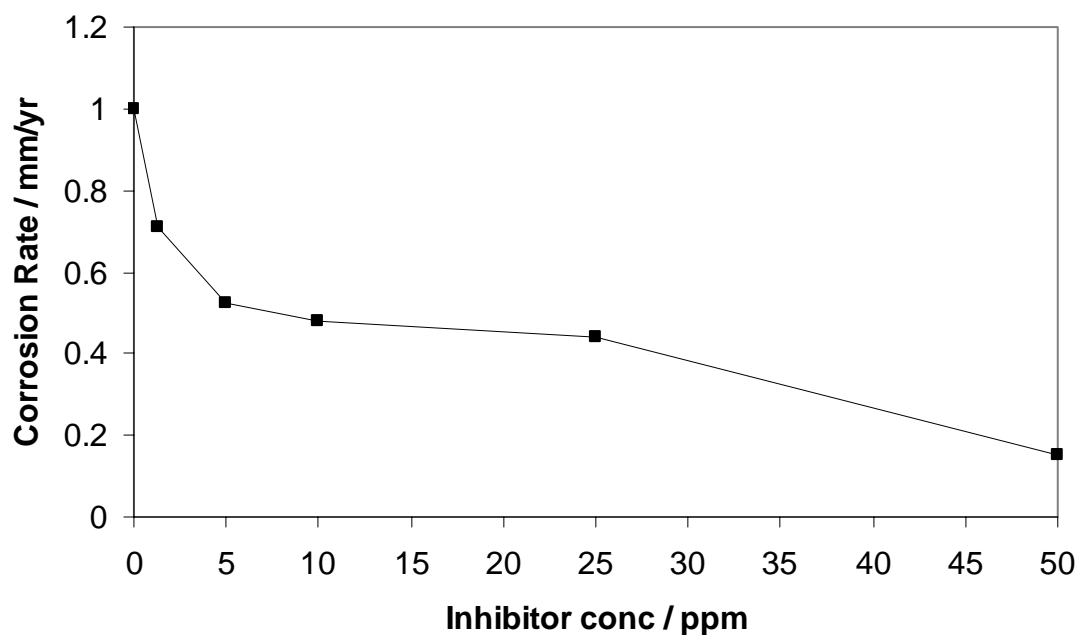


Figure 10. Effect of inhibitor A concentration on the corrosion rate for pH 6.6, T = 80 °C, no Fe<sup>++</sup> added, stagnant conditions.

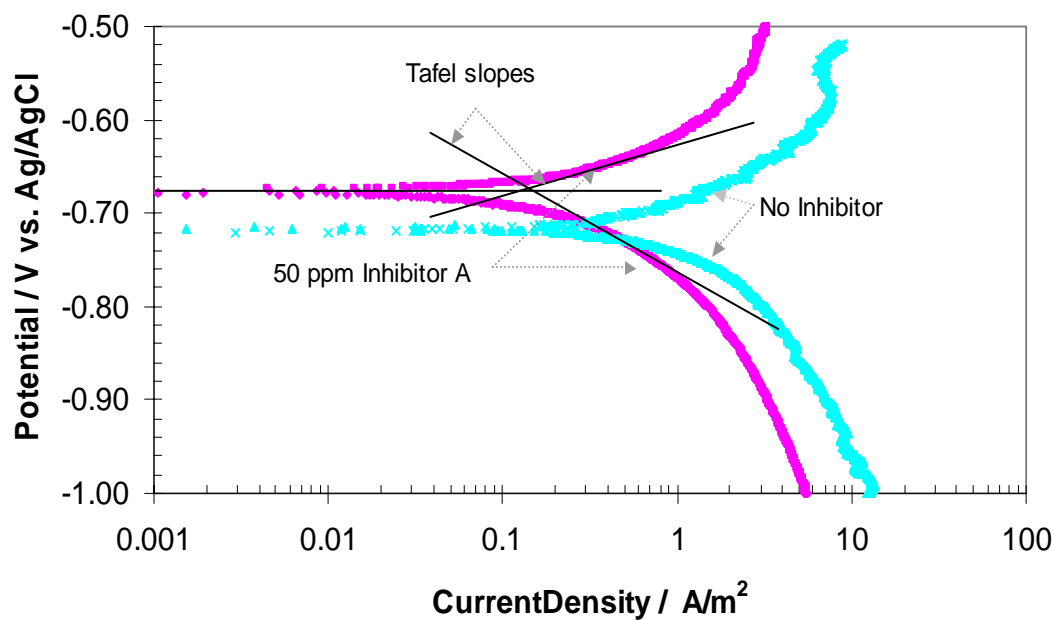


Figure 11. Polarization curves for 50 ppm inhibitor A at pH 6.6,  $T = 80\text{ }^{\circ}\text{C}$ , no  $\text{Fe}^{++}$  added, stagnant conditions.

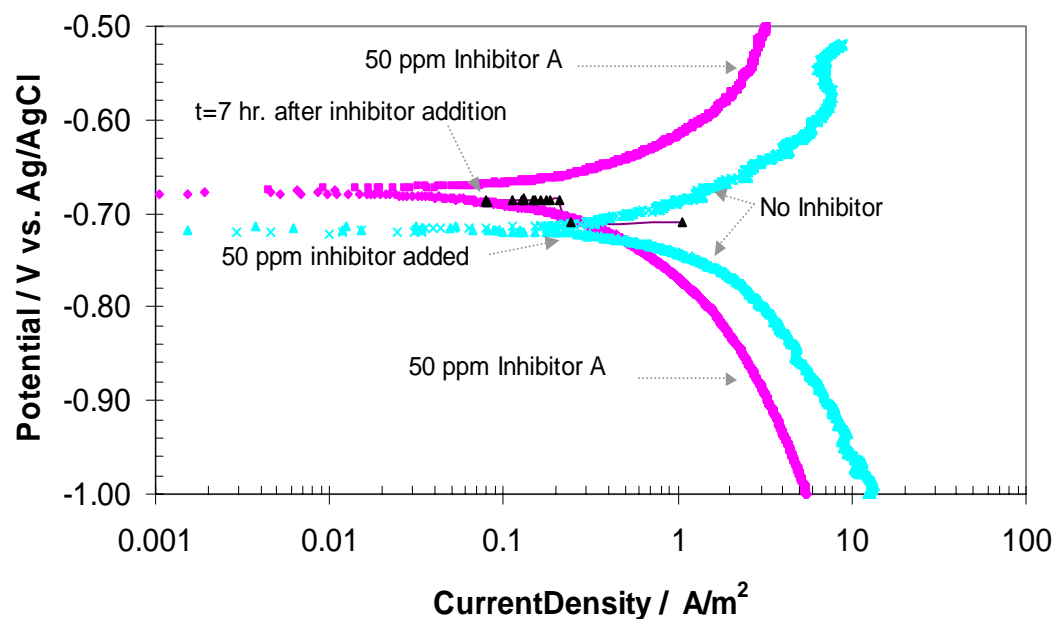


Figure 12. Pseudo-Polarization curves for 50 ppm inhibitor at pH 6.6,  $T = 80\text{ }^{\circ}\text{C}$ , no  $\text{Fe}^{++}$  added, stagnant conditions.

### 5.1.2 Inhibitor B

Inhibitor B which was supplied to us by Champion Technologies Inc. six months after the research with inhibitor A, had started had an even simpler formulation than Inhibitor A, since one compound (Benzyl dimethyl coco-quat chloride) was removed from the inhibitor A formulation. Hence it was used for most of the experiments performed.

Figure 13 shows the effect of pH on corrosion rate at the inhibitor B concentration of 50 ppm. From the graph, it is seen that as the pH is increased from 4 to 6.6 the final corrosion rate decreases. Hence, since the inhibitor is not very efficient at lower pH, experiments at lower pH's were not done.

Figure 14 and Figure 15 show the change in corrosion rate vs. time for different inhibitor concentrations at pH 6.0 and pH 6.6, respectively. These graphs were used to find out the inhibitor efficiency at different concentrations.

To study the nature of the inhibitor, the potentiodynamic sweeps for the experiments were done at pH 6.60. The sweeps were done in the cathodic direction initially. Then after waiting for sometime for the potential to stabilize the anodic sweep was carried out. From the sweeps (Figure 16), the anodic and the cathodic Tafel slopes for inhibitor B were calculated to be 60 mV/decade and 120 mV/decade respectively and the 'B' value was calculated to be 17.36 mV. The value of 'B' value obtained from textbook calculations averaged over a temperature range of 20 °C - 80 °C (shown in Appendix B) was found to be 16.6 mV. Hence, value of 17 mV was used for all the experiments.

From the graph shown in Figure17, it is seen that when 10 ppm of inhibitor is added, the cathodic reaction is inhibited, and the anodic is not inhibited. When the inhibitor concentration is increased to 25 ppm, the anodic as well as the cathodic reaction is inhibited. As the inhibitor concentrations are increased to 35 ppm and 50 ppm, it was observed that the inhibition in the cathodic reaction remains practically unchanged, while the inhibition in the anodic reaction increases with the inhibitor concentration. A rise of the potential in the anodic direction with the increases in the inhibitor concentration was also observed. Thus from the potentiodynamic sweeps, it can be concluded that the inhibitor B inhibits both reactions, although anodic more than the cathodic.

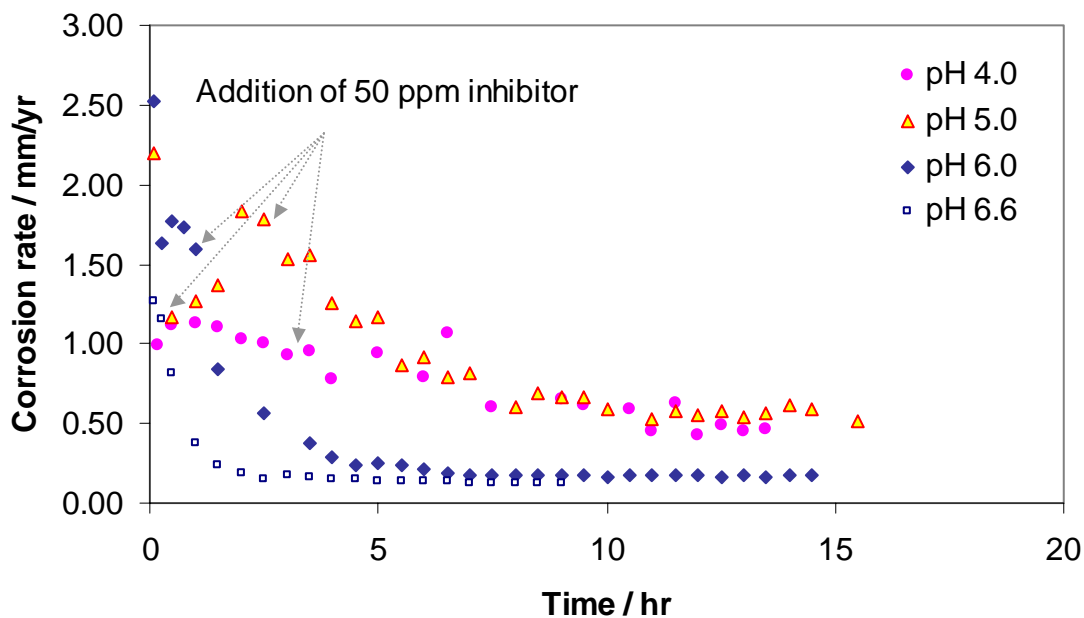


Figure 13. Change in corrosion rate with time for different pH at  $T = 80\text{ }^{\circ}\text{C}$ , no  $\text{Fe}^{++}$  added, stagnant conditions.

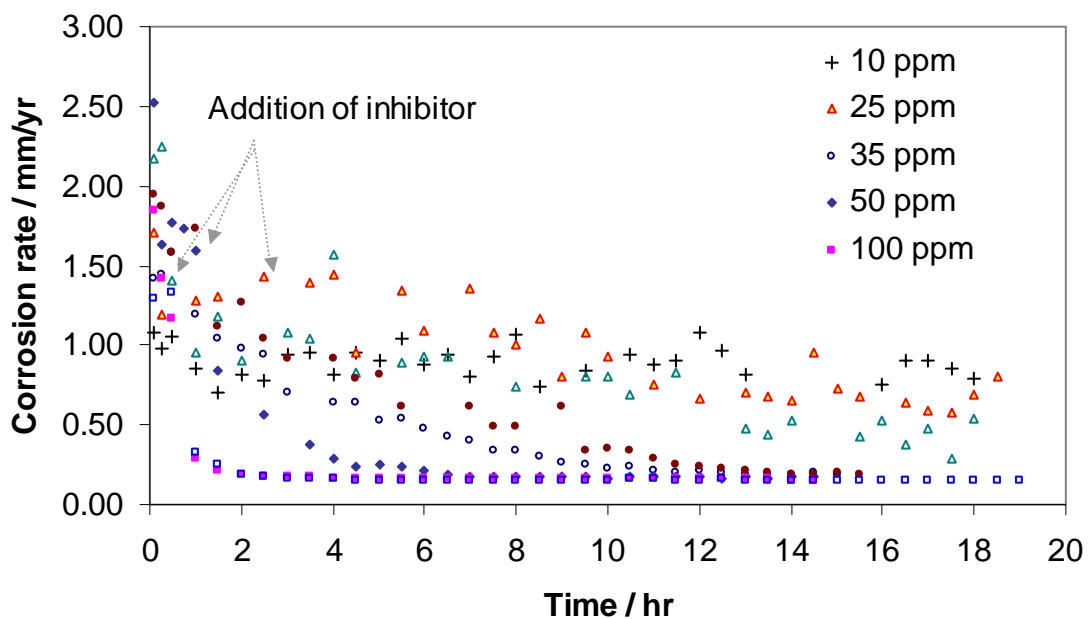


Figure 14. Change in corrosion rate with time for different inhibitor concentrations for pH 6.00,  $T = 80\text{ }^{\circ}\text{C}$ , no  $\text{Fe}^{++}$  added, stagnant conditions. Same symbol shapes depict repetitions of the same experiments.

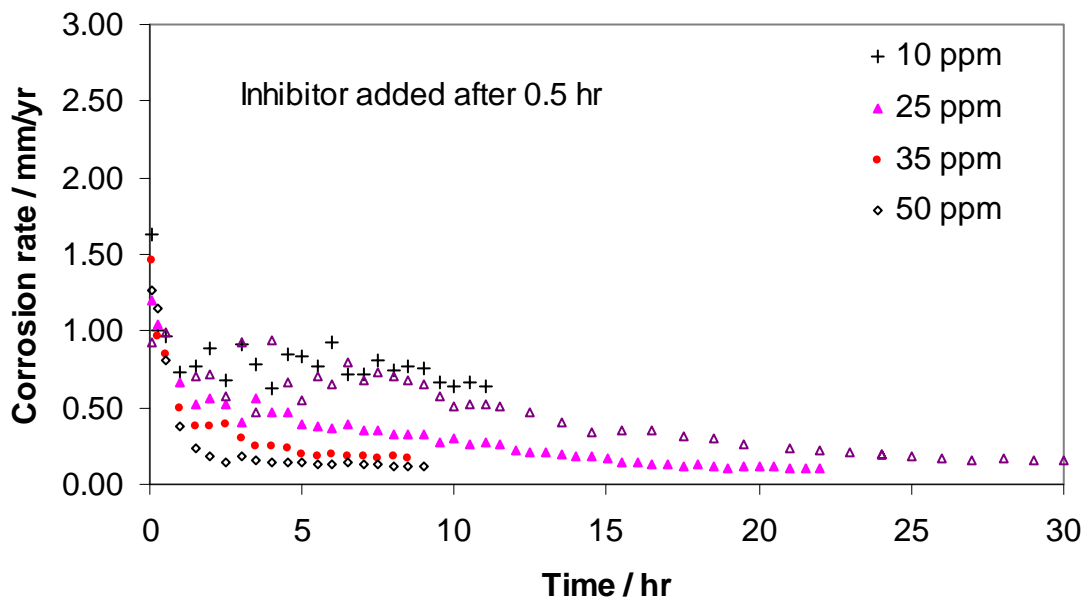


Figure15. Change in corrosion rate with time for different inhibitor concentrations for pH 6.60, T = 80 °C, no Fe<sup>++</sup> added, stagnant conditions. Same symbol shapes depict repetitions of the same experiments.

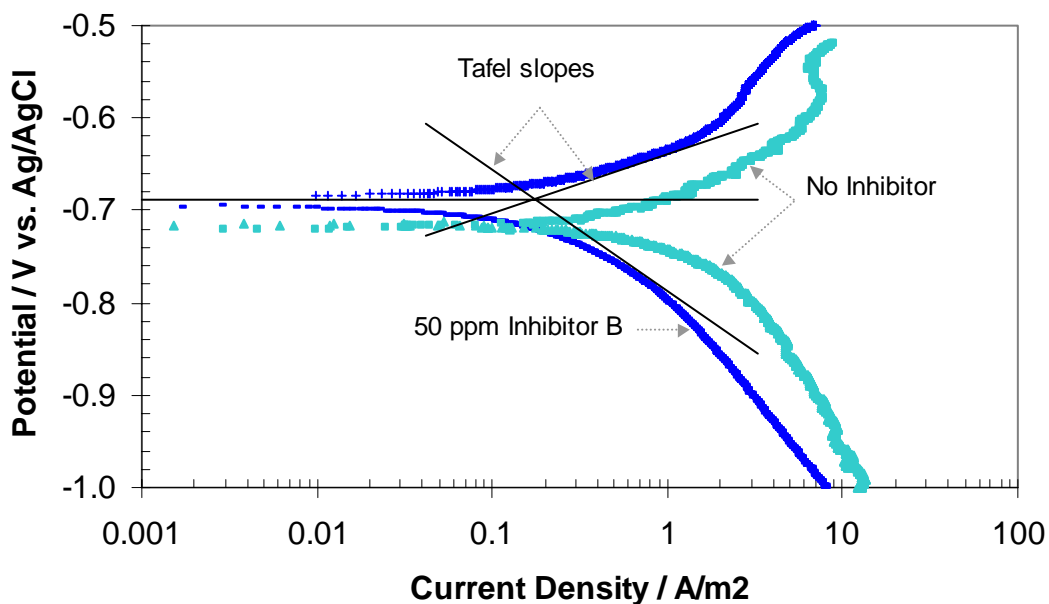


Figure 16. Polarization curves for 50 ppm inhibitor B showing the tafel slopes, at pH 6.6, T = 80 °C, no Fe<sup>++</sup> added, stagnant conditions.

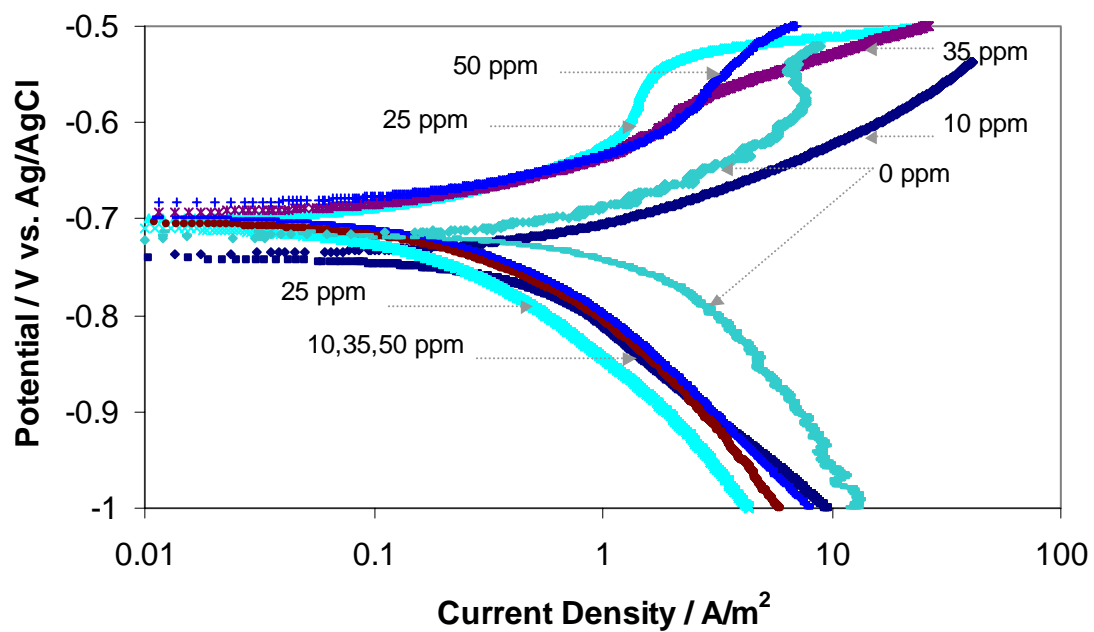


Figure17. Potentiodynamic Sweeps for different inhibitor concentrations at pH 6.60, T = 80 °C, no Fe<sup>++</sup> added, stagnant conditions.

## 5.2 Baseline Experiments at different supersaturations without inhibitor

These set of experiments were designed to see the effect of iron carbonate scale formation at various supersaturations, on the corrosion rate. The supersaturation was varied from 7 to 150 by changing the pH and the  $\text{Fe}^{++}$  concentration. The  $\text{Fe}^{++}$  was added in the system in the form of  $\text{FeCl}_2 \cdot 4\text{H}_2\text{O}$  salt solution.

### 5.2.1 Experiments at supersaturation of 150

At 80 °C, a supersaturation of 150 is achieved at pH 6.60 and by adding 50 ppm of  $\text{Fe}^{++}$  initially. Figure 18 depicts the change of corrosion rate with time at supersaturation of 150. Figure 19 consists of the trend that was obtained by compiling results of this investigation with that of Wei Sun (2003) and Omkar Nafday (2003). The error bar on the curve was obtained by finding the maximum and the minimum values of the experiments. Under these conditions, a drastic drop in the corrosion rate to less than 0.2 mm/yr in approximately 8 – 10 hours is observed.

Figure 20 shows the top view and the cross-sectional view of the sample obtained from the previous experiment at 500X. In this figure, a dense iron carbonate film of thickness 15-20 $\mu\text{m}$ , formed after 20 hours, is observed.

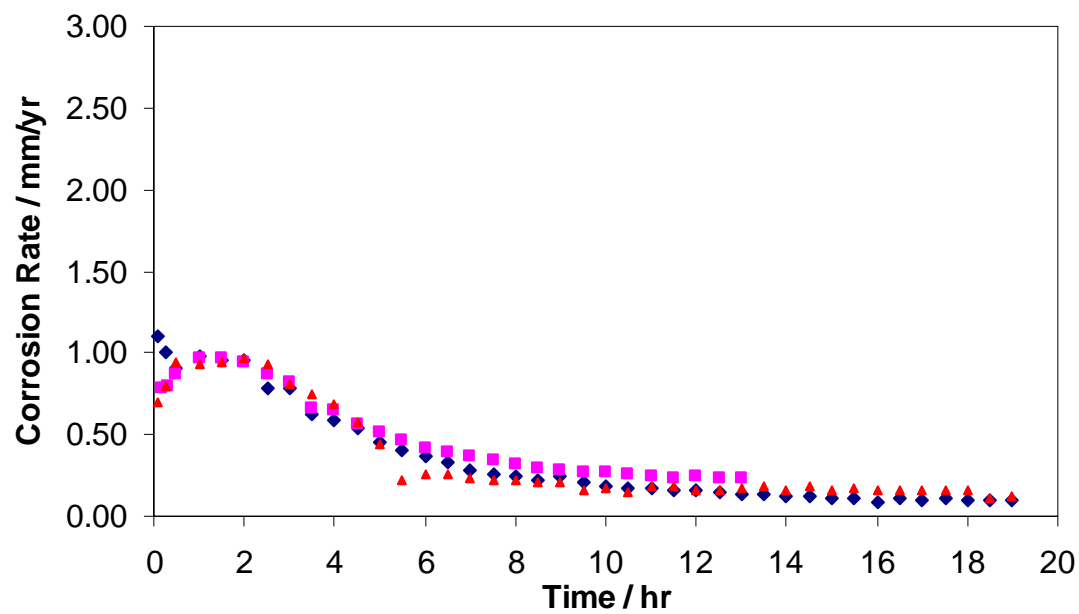


Figure 18. Change in corrosion rate with time for pH 6.60,  $\text{Fe}^{++} = 50$  ppm, no inhibitor,  $T = 80$  °C, SS = 150, stagnant conditions.

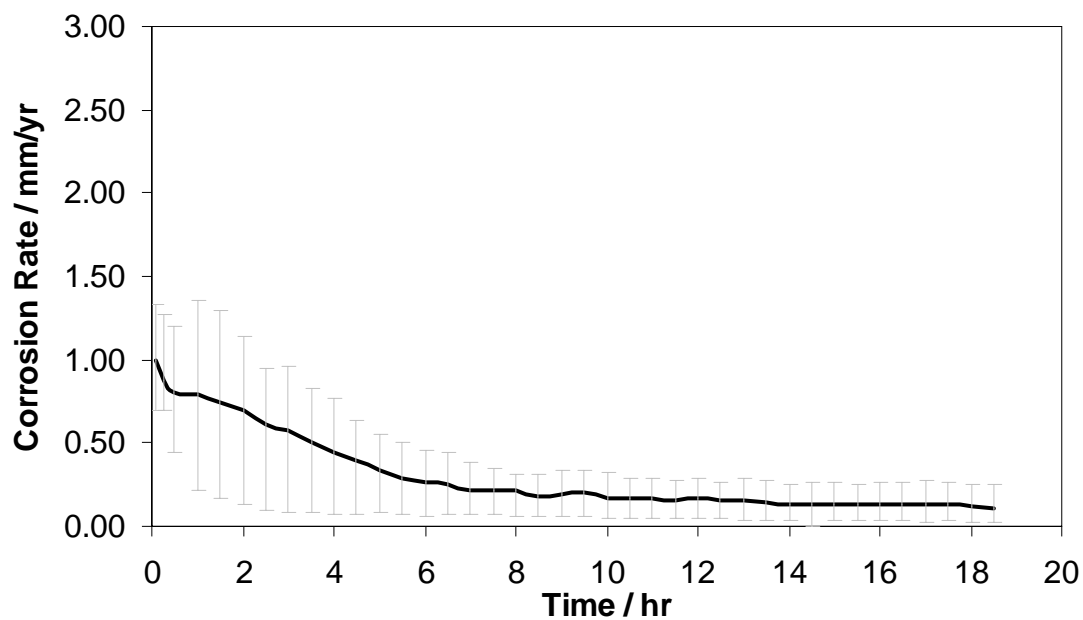


Figure 19. Average curve for change in corrosion rate with time for pH 6.60,  $Fe^{++} = 50$  ppm, no inhibitor,  $T = 80$  °C, SS = 150, stagnant conditions. (For SEM of experiment see Figure 20)

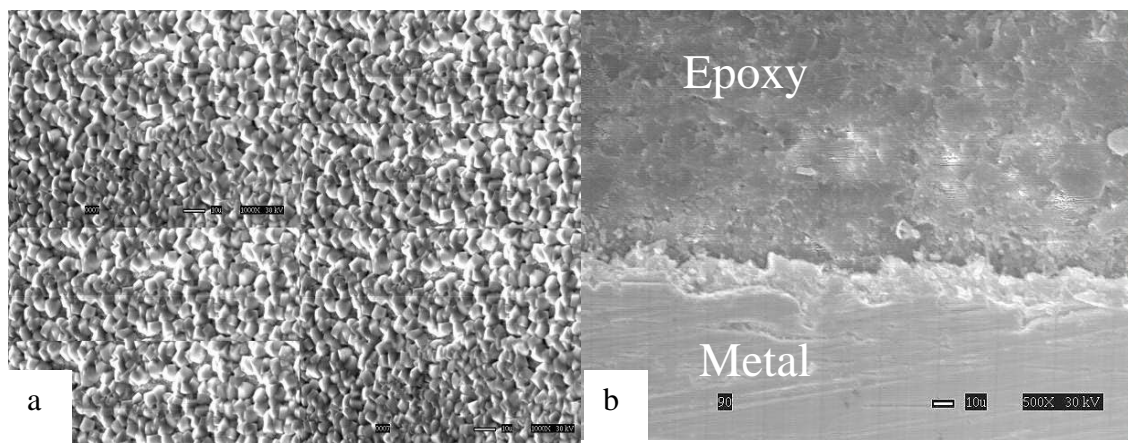


Figure 20. Top view (a) and cross-sectional view (b) of the specimen for pH 6.60,  $Fe^{++} = 50$  ppm, no inhibitor, SS = 150,  $T = 80$  °C, stagnant conditions.

### 5.2.2 Experiments at supersaturation of 30

Figure 21 shows the results from experiments done at pH 6.6 by adding  $\text{Fe}^{++}=10$  ppm, resulting in a supersaturation of 30. From the graph, it is seen that the corrosion rate starts between 1.00-1.50 mm/yr and gradually decreases to 0.1 mm/yr in approximately 45-50 hours.

Recall that, the entire precipitation process consists of two steps, nucleation and crystal growth. Nucleation process is very sensitive to the surface of the metal, and hence is very difficult to control. It is the nucleation step which triggers the crystal growth of iron carbonate. From Figure 22, it can be seen that once the nucleation step is adjusted for in a couple of experiments by moving the time scale by approximately 5 hours forward/backward, the precipitation kinetics is similar for all the experiments. As the data shown in the figure are repetitions of the same experiments, the average curve from all the experiments was found out and the error bar on the curve was obtained by finding the maximum and minimum values of all the experiments (Figure 23). The top view and the cross-sectional view of one of the experiments are shown in Figure 24. A dense iron carbonate scale of thickness of 30-40 $\mu\text{m}$  is obtained.

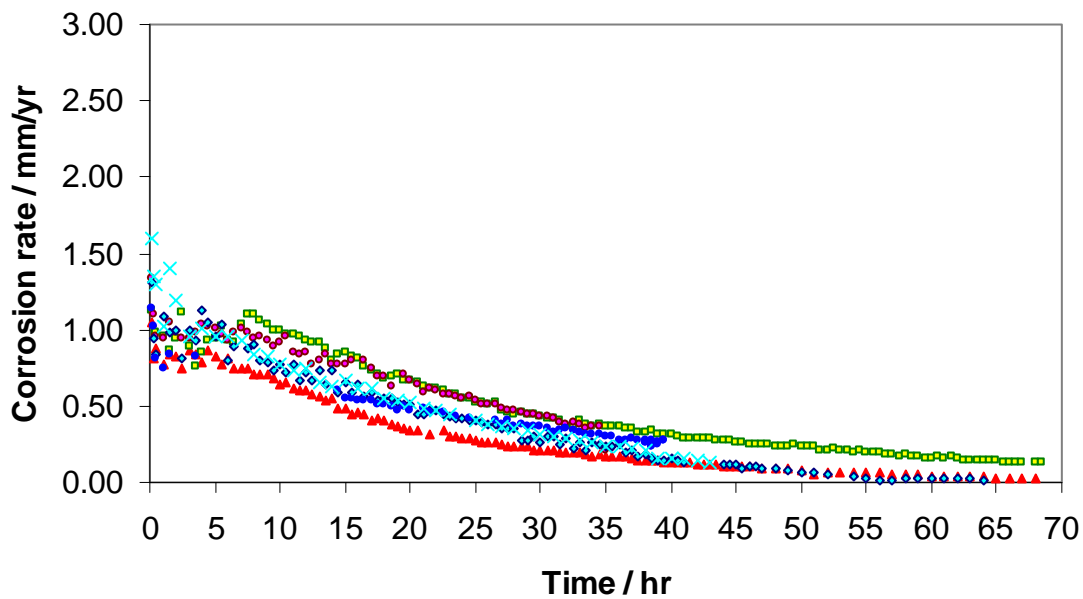


Figure 21. Change in corrosion rate with time for pH 6.60,  $Fe^{++} = 10$  ppm,  $T = 80$  °C, SS = 30, no inhibitor, stagnant conditions.

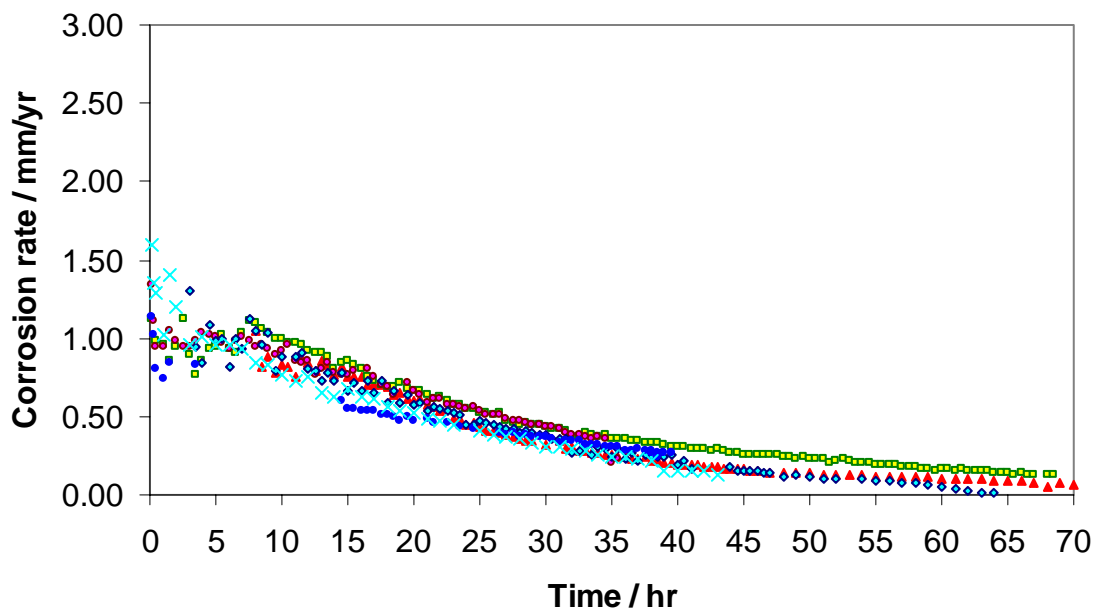


Figure 22. Adjusted graph for change in corrosion rate with time for pH 6.60,  $Fe^{++} = 10$  ppm,  $T = 80$  °C, SS = 30, no inhibitor, stagnant conditions.

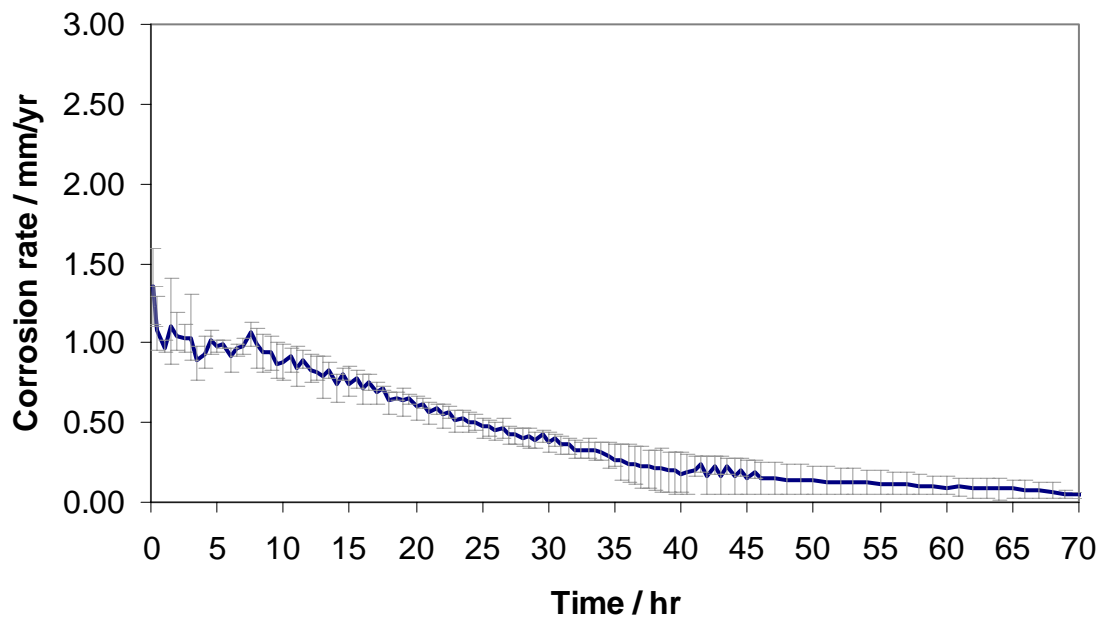


Figure 23. Average curve for the change in corrosion rate with time for pH 6.60,  $\text{Fe}^{++} = 10$  ppm, SS = 30,  $T = 80^\circ\text{C}$ , no inhibitor, stagnant conditions. (For SEM of experiment see Figure 24)

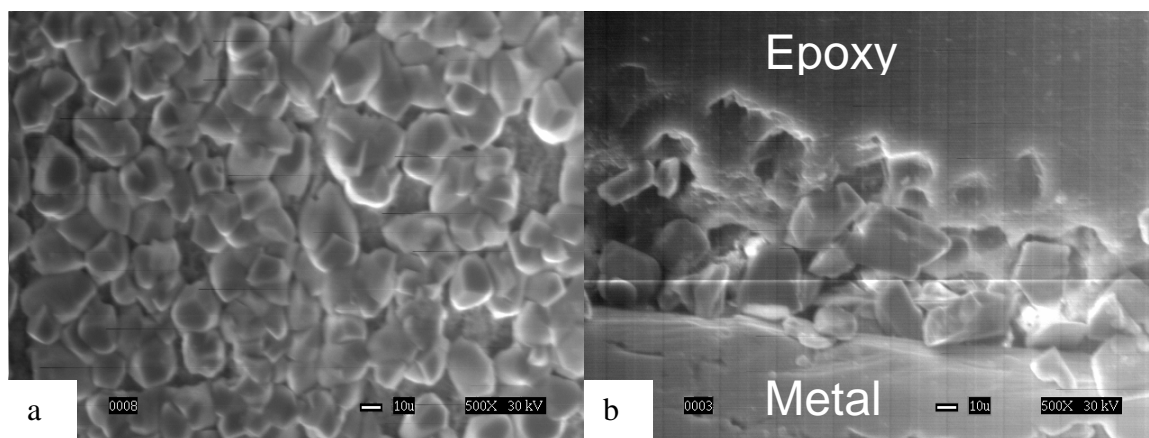


Figure 24. The top view (a) and the cross-sectional view (b) of sample at 500X for pH 6.60,  $\text{Fe}^{++} = 10$  ppm, no inhibitor,  $T = 80^\circ\text{C}$ , SS = 30, stagnant conditions.

### 5.2.3 Experiment at supersaturation of 37

Figure 25 shows the results from experiments done at pH 6.3 by adding  $\text{Fe}^{++}=50$  ppm, resulting in a supersaturation of 37. From the graph, it is seen that the corrosion rate starts between 1.50-2.00 mm/yr and gradually decreases to 0.2 mm/yr in approximately 70 hours.

The top view and the cross-sectional view of one of the experiments are shown in Figure 26. A dense iron carbonate scale of thickness of 30-40 $\mu\text{m}$  is obtained.

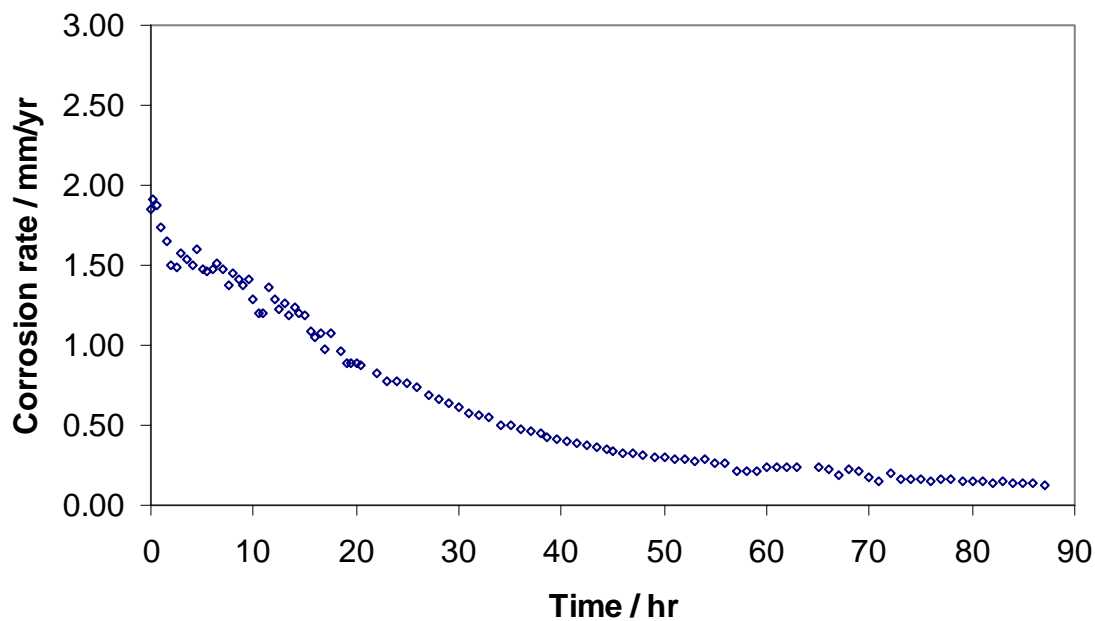


Figure 25. Change in corrosion rate with time for pH 6.30,  $\text{Fe}^{++} = 50$  ppm,  $T = 80$  °C, SS = 37, no inhibitor, stagnant conditions. (For SEM of experiment see Figure 26)

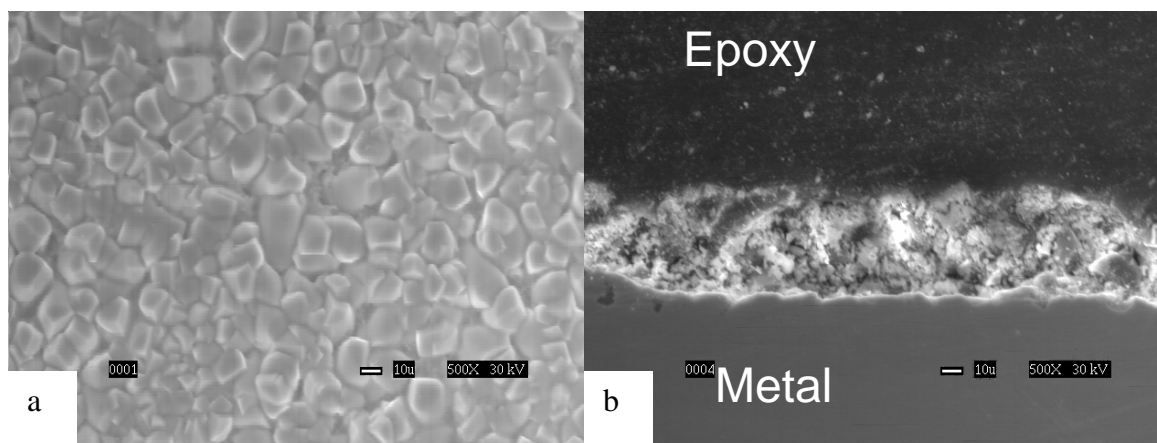


Figure 26. The top view (a) and the cross-sectional view (b) of sample at 500X for pH 6.30,  $\text{Fe}^{++} = 50$  ppm, SS = 37,  $T = 80$  °C, no inhibitor, stagnant conditions.

#### 5.2.4 Experiment at supersaturation of 7

Figure 27 shows the results from experiments done at pH 6.3 by adding  $\text{Fe}^{++}=10$  ppm, resulting in a supersaturation of 7. From the graph, it is seen that the corrosion rate starts between 1.00-1.50 mm/yr and gradually starts decreasing after 25 hours, due to formation of the iron carbonate scale.

The top view and the cross-sectional view of one of the experiments are shown in Figure 28. A porous iron carbonate scale of thickness of  $10\mu\text{m}$  is obtained after 45 hours.

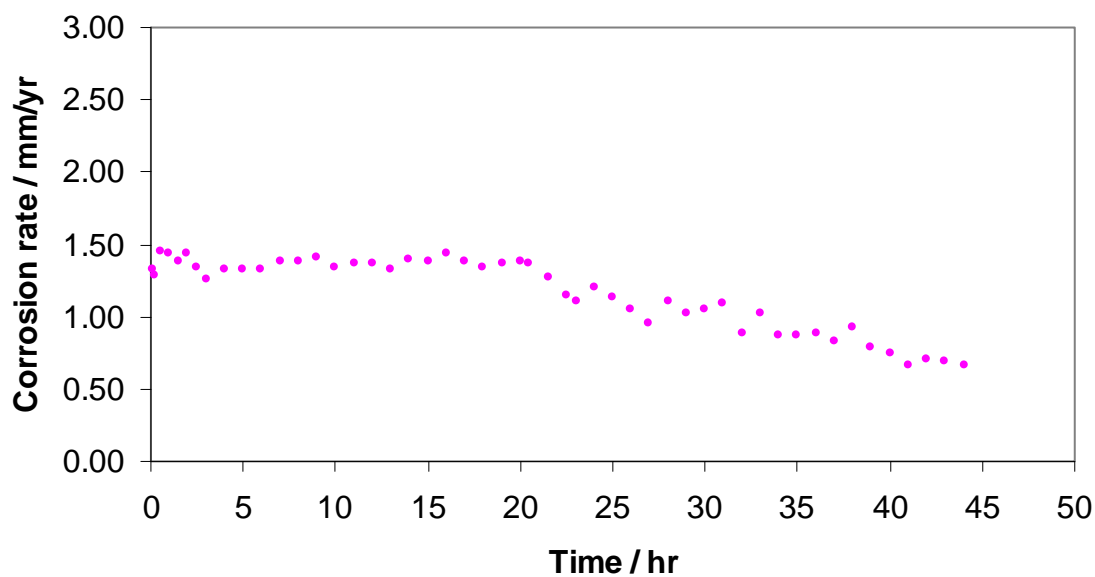


Figure 27. Change in corrosion rate with time for pH 6.30,  $\text{Fe}^{++} = 10$  ppm,  $T = 80$  °C, SS = 7, no inhibitor, stagnant conditions. (For SEM of experiment see Figure 28)

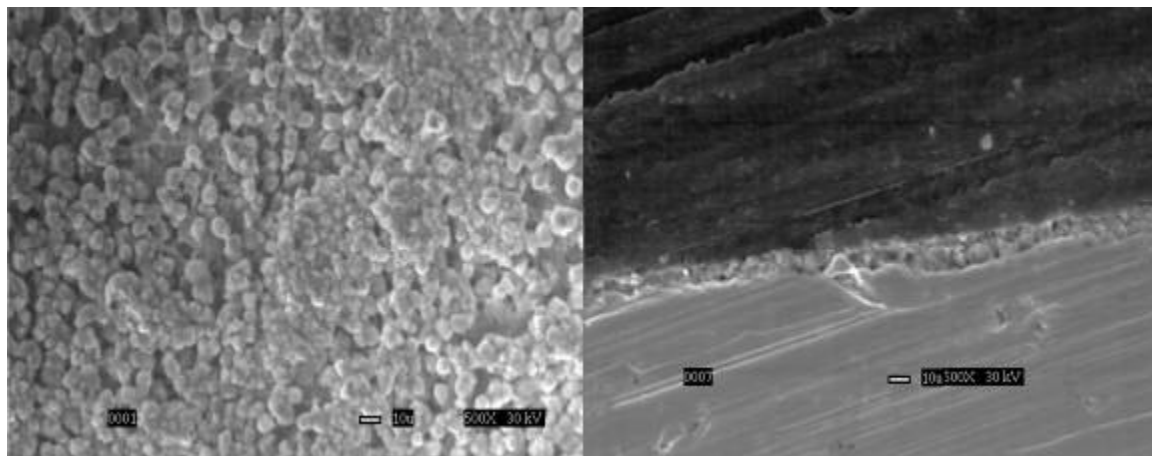


Figure 28. The top view (a) and the cross-sectional view (b) of sample at 500X for pH 6.30,  $\text{Fe}^{++} = 10$  ppm, SS = 7,  $T = 80$  °C, no inhibitor, stagnant conditions.

### 5.2.5 Summary of baseline experiments

The effect of change in supersaturation on the precipitation of iron carbonate and the consequent change in the corrosion rate is shown in Figure 29. Table 5 shows the conditions under which these supersaturations were obtained. The supersaturations were varied from a range of 7 to 150 by varying the pH from 6.0 - 6.6 and the iron concentration from 10 - 50 ppm. Increase in the precipitation rate of iron carbonate is observed in the Figure 29, due to the increase in supersaturation of the solution with respect to iron carbonate. This increase in the precipitation rate, results in a subsequent fall in the corrosion rate of the metal, since the scale blocks a part of the metal surface and prevents it from corroding and acts as a diffusion barrier for the corroding species.

A comparison of scale thickness, crystal grain size, and final corrosion rate for all the baseline experiments at supersaturation of 7 – 150, are shown in Table 6. It is observed that as the supersaturation is increased, the size of the iron carbonate crystal decreases. This is expected since with higher supersaturation and precipitation rates, higher the number of crystals that would nucleate on the surface of the metal is created. This causes interference in growth of the crystals due to the adjacent crystals. However, at supersaturation of 7, this phenomenon is not observed since the experiment was stopped after 45 hours and the crystals were not allowed to grow further.

Table 5. Bulk supersaturation of the solution at various pH and Fe<sup>++</sup> concentration

Ph	Fe <sup>++</sup> Concentration/ ppm	Supersaturation
6.00	50	9
6.30	10	7
6.30	50	37
6.60	10	30
6.60	50	150

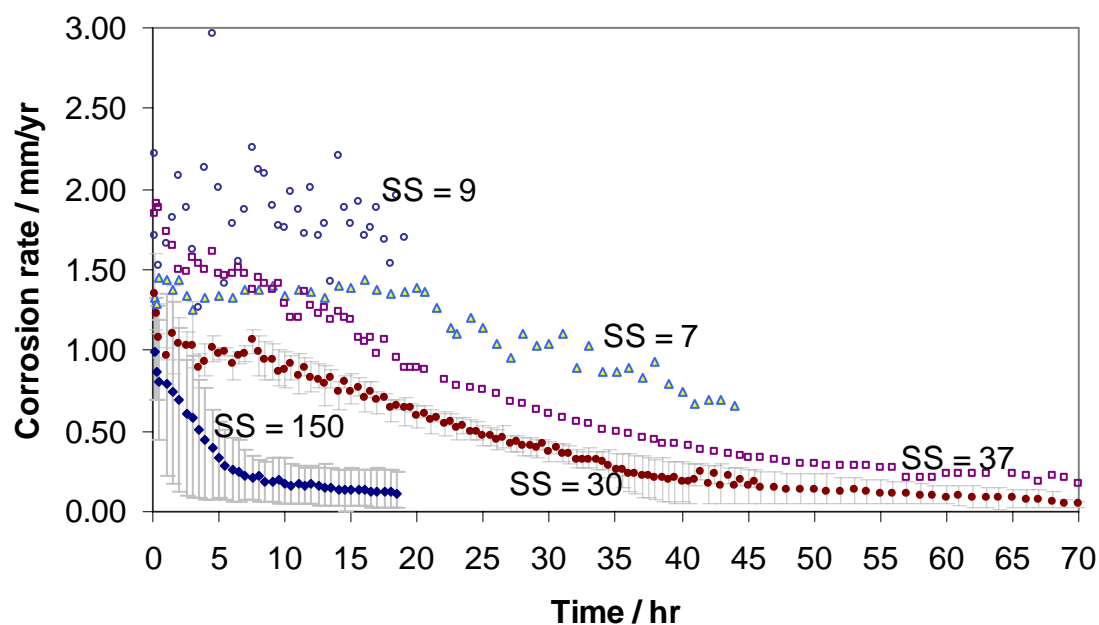


Figure 29. Effect of supersaturation on corrosion rate at T = 80 °C, no inhibitor, stagnant conditions.

Table 6. Summary of baseline experiments at supersaturation 7 – 150, T = 80 °C, no inhibitor, stagnant conditions.

SS	Experimental time/ hr.	Scale thickness / $\mu\text{m}$ .	Crystal grain size / $\mu\text{m}$ .	Final corrosion rate / mm/yr.
7	45	10	10	0.65
9	19	No scale formed	No scale formed	1.8
30	85	30 – 40	15 - 25	0.027
37	87	30 - 40	15 - 25	0.13
150	19	15 - 25	5	0.1

### 5.3 Inhibitor-scale interactions

Based on the previous experiments, in this set of experiments various concentrations of inhibitor was added under different scale-forming conditions.

#### 5.3.1 Interactions at supersaturation of 150

In this set of experiments selected concentration of inhibitor A was added to the solution that is at an initial supersaturation of 150 w.r.t. iron carbonate. From Figure 10, it can be seen that at 25 ppm, inhibitor A is partially protective. So, 25 ppm was chosen as the concentration to start the testing. In order to study the effect of more protective inhibitor film, 50 ppm was added in subsequent experiments.

#### Inhibitor A added at the beginning

These experiments were designed to see the interaction of the inhibitor and the iron carbonate scale when both the processes would compete for adsorption on the metal surface.

In the experiment shown in Figure 30, a supersaturation of 150 was achieved in the beginning by adjusting the pH to 6.60 and adding 50 ppm of  $\text{Fe}^{++}$ , and 25 ppm inhibitor A was added after 15 minutes of starting the experiment. The trend for the 25 ppm inhibitor in Figure 30, denotes the average value of all the repeated experiments, and the error bars are the maximum and the minimum values. It can be seen that in the presence of the 25 ppm inhibitor, the corrosion rate decrease is similar to that of experiment without inhibitor. All the points of the 25 ppm experiment lie within the error

range of the experiments having no inhibitor. Hence, it could be concluded that the inhibitor had no effect on scale formation and the corrosion rate. From Figure 31, It is seen that a dense carbonate scale of thickness 20-30 $\mu\text{m}$  is formed in the presence of the inhibitor is similar to one formed in the absence of inhibitor (Figure 20). Therefore, it seems that the protection the metal is mainly due to the iron carbonate scale.

Figure 32 shows of the experiment in which a supersaturation of 150 was achieved in the beginning and then 50 ppm inhibitor was added 15 minutes after starting the experiment. From the figure, it can be seen that although the corrosion rate drops to 0.2 mm/yr in less than two hours, the final corrosion rate is the same as that without the inhibitor. It can be observed that for this experiment, the inhibitor dominates the iron carbonate scale from the beginning. From the front view of the sample (

Figure **33**), it can be seen that very little iron carbonate is seen on the surface of the metal. Therefore, it seems that the metal surface is mainly protected due to the presence of the inhibitor and 50 ppm of inhibitor seems to hamper the growth of iron carbonate on the surface of the metal.

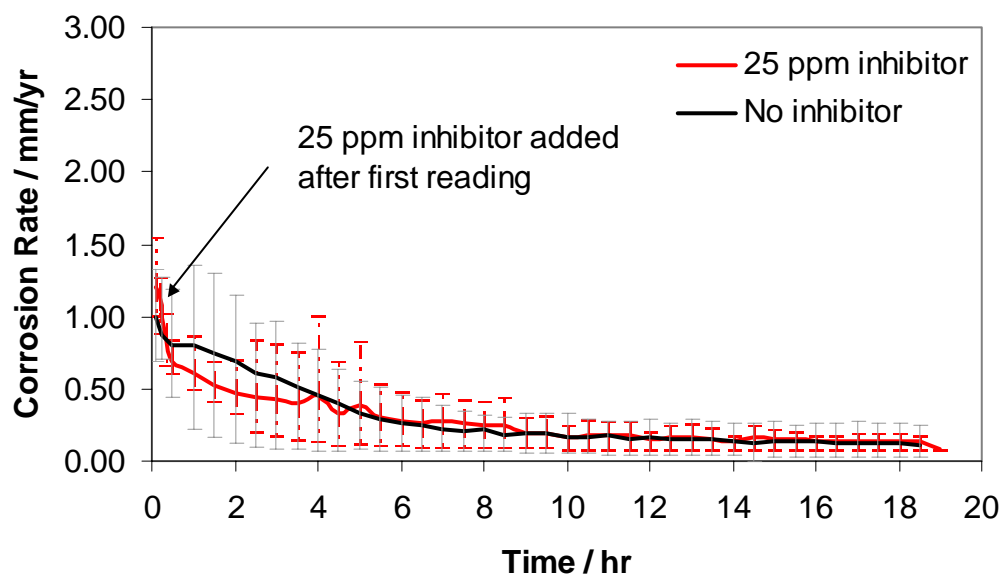


Figure 30. Effect of addition of 25 ppm inhibitor A added initially on corrosion rate for pH 6.60,  $\text{Fe}^{++} = 50$  ppm, SS = 150,  $T = 80$  °C, stagnant conditions (For SEM of experiment see Figure 31)

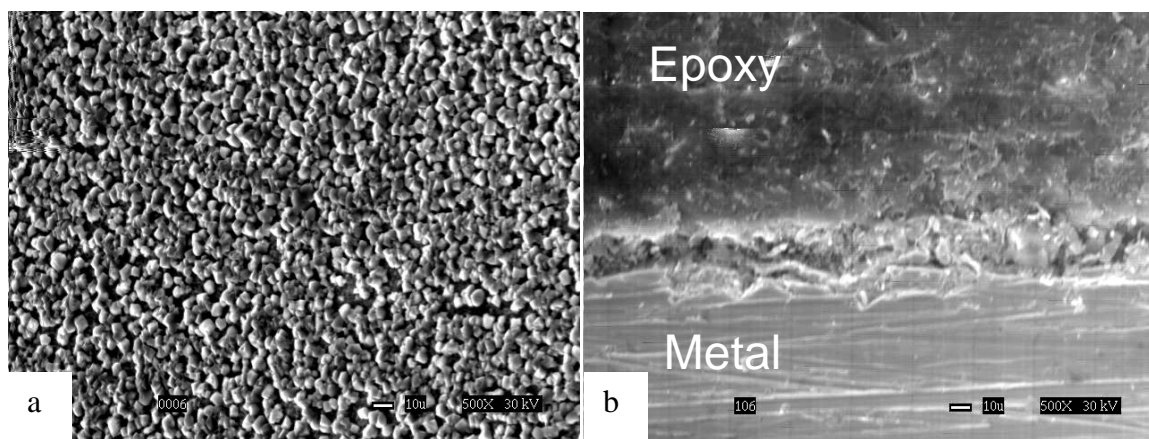


Figure 31. The top view (a) and the cross-sectional view (b) of sample with 25 ppm inhibitor A added immediately, for pH 6.60,  $\text{Fe}^{++} = 50$  ppm, SS = 150,  $T = 80$  °C, stagnant conditions.

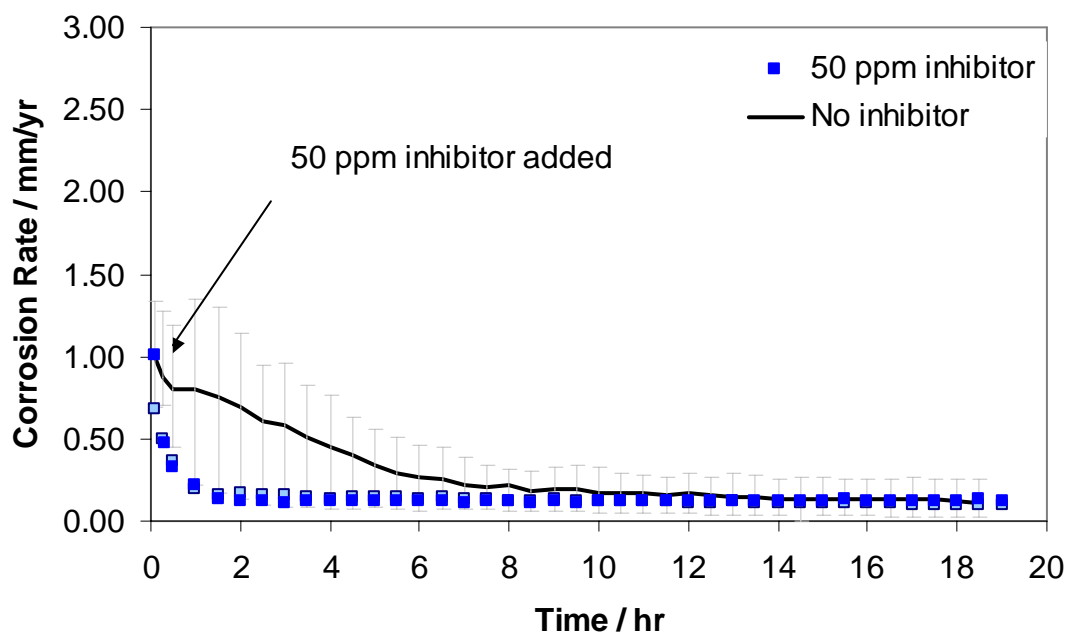


Figure 32. Effect of addition of 50 ppm inhibitor A added initially on corrosion rate for pH 6.60,  $Fe^{++} = 50$  ppm, SS = 150,  $T = 80$  °C, stagnant conditions.(For SEM of experiment see

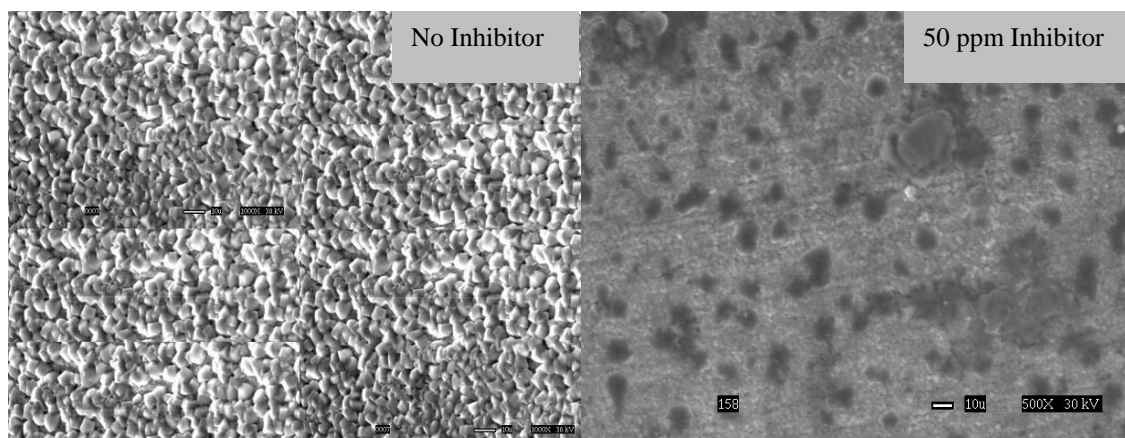


Figure 33).

Figure 33. Comparison of Top view for specimen with 50 ppm inhibitor A and without inhibitor at pH 6.60,  $Fe^{++} = 50$  ppm, SS = 150,  $T = 80$  °C , stagnant conditions.

*Inhibitor A added after 5 hours.*

In these set of experiments, the inhibitor was added after 5 hours. These experiments were designed to see the interaction of the inhibitor and the iron carbonate scale when the latter is partially formed.

In the experiment shown in Figure 34, a supersaturation of 150 was achieved in the beginning by adjusting the pH to 6.60 and adding 50 ppm of  $\text{Fe}^{++}$ . Subsequently, 25 ppm inhibitor A was added after 5 hours. The experiment was repeated 3 times. It is observed that the inhibitor had no effect on the corrosion rate since all the points lie within the error range of the experiment without any inhibitor. From the top view and the cross-sectional view (Figure 35), a dense iron carbonate film of 30  $\mu\text{m}$  is observed. The corrosion rate is mainly reduced due to the formation of the iron carbonate scale.

Figure 36 consists of the experiment in which a supersaturation of 150 was achieved in the beginning, and subsequently 50 ppm inhibitor was added 5 hours after starting the experiment. In this experiment, it can be seen that as soon as the inhibitor is added, the corrosion rate drops rapidly. From the top view of the specimen in Figure 37, It is seen that there are only a few crystals of iron carbonate formed on the surface of the metal. These iron carbonate crystals might have formed before the addition of the inhibitor and subsequently, the inhibitor hampered the growth of the iron carbonate.

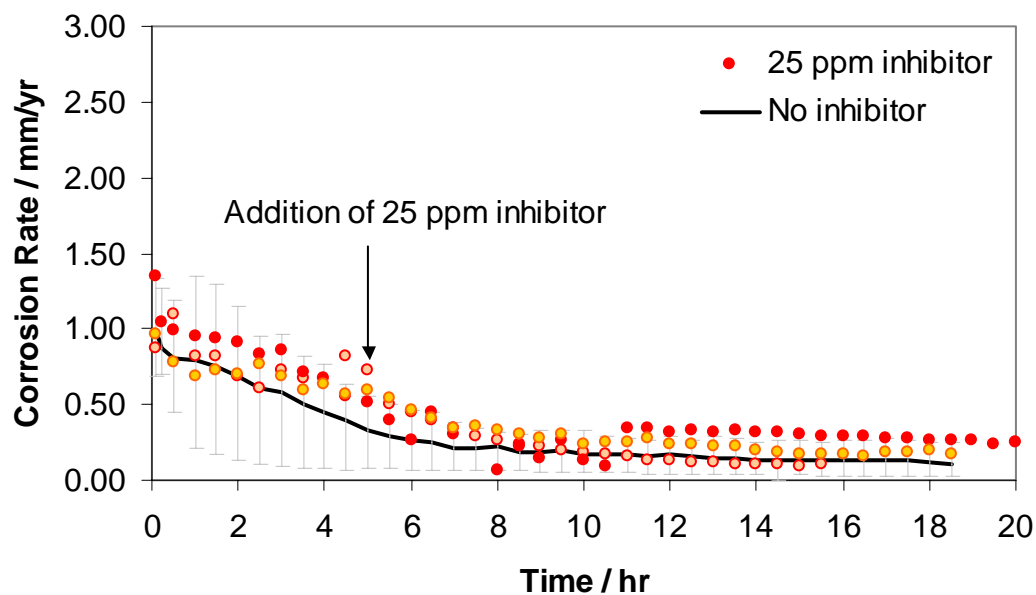


Figure 34. Effect of addition of 25 ppm inhibitor A after 5 hours on corrosion rate for pH 6.60,  $Fe^{++} = 50$  ppm, SS = 150,  $T = 80$  °C, stagnant conditions. (For SEM of experiment see Figure 35).

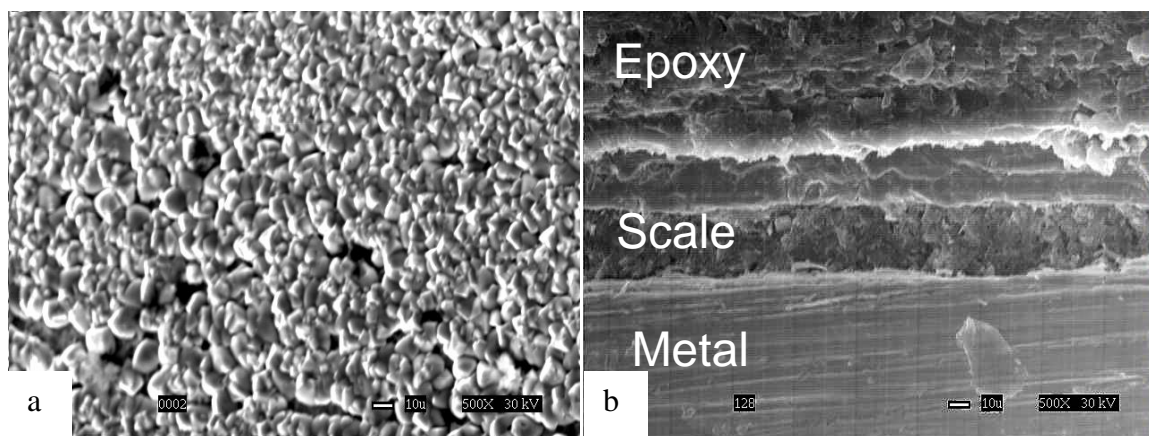


Figure 35. The top view (a) and the cross-sectional view (b) of sample with 25 ppm inhibitor A added after 5 hours for pH 6.60,  $Fe^{++} = 50$  ppm, SS = 150,  $T = 80$  °C, stagnant conditions.

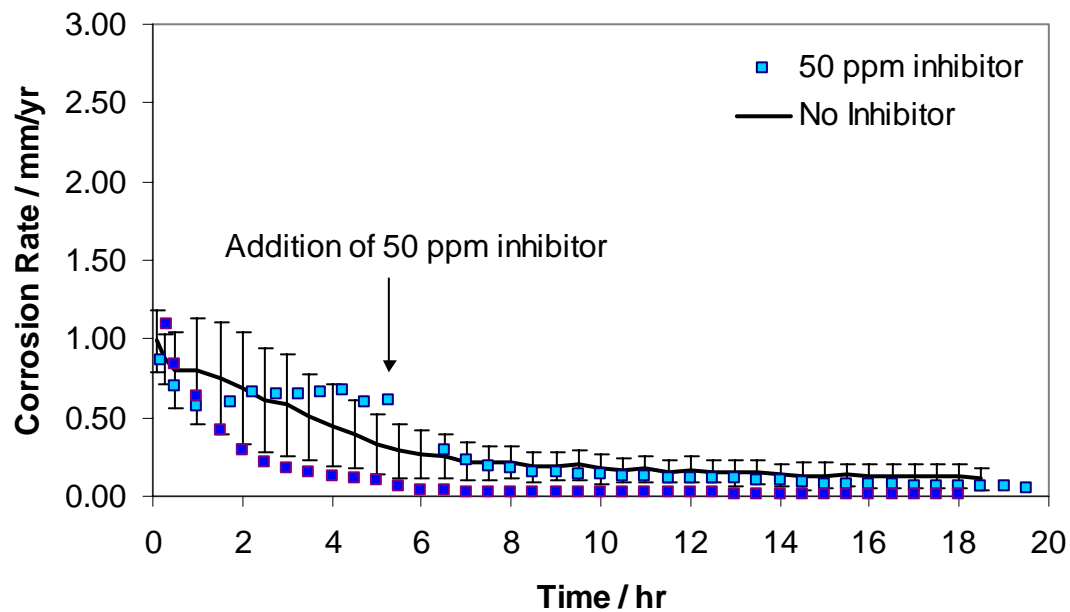


Figure 36. Effect of addition of 50 ppm inhibitor A after 5 hours on corrosion rate for pH 6.60,  $\text{Fe}^{++} = 50$  ppm, SS = 150,  $T = 80$  °C, stagnant conditions. (For SEM of experiment see Figure 37).

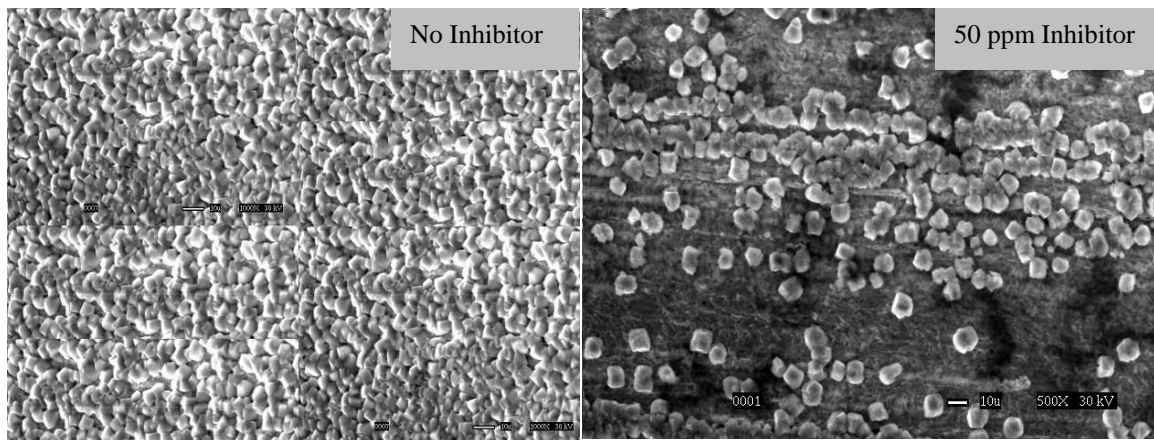


Figure 37. Comparison of top view for specimen with 50 ppm inhibitor A added after 5 hours and without inhibitor at pH 6.60,  $\text{Fe}^{++} = 50$  ppm, SS = 150,  $T = 80$  °C, stagnant conditions.

Figure 38 shows the potentiodynamic sweeps for the solution with

- No inhibitor and no scale,
- 50 ppm inhibitor added
- 25 ppm inhibitor and iron carbonate scale.

The sample with 25 ppm inhibitor and iron carbonate scale was polarized 20 hours after inhibitor and  $\text{Fe}^{++}$  were added. In the case of 50 ppm inhibitor, the sample was polarized for 2 hours after the inhibitor was added. This was to ensure that the inhibitor had fully acted on the sample. From the sweeps, it can be seen that the inhibitor slows down the anodic reaction as well as the cathodic reaction while the presence of the iron carbonate scale retards only cathodic reaction.

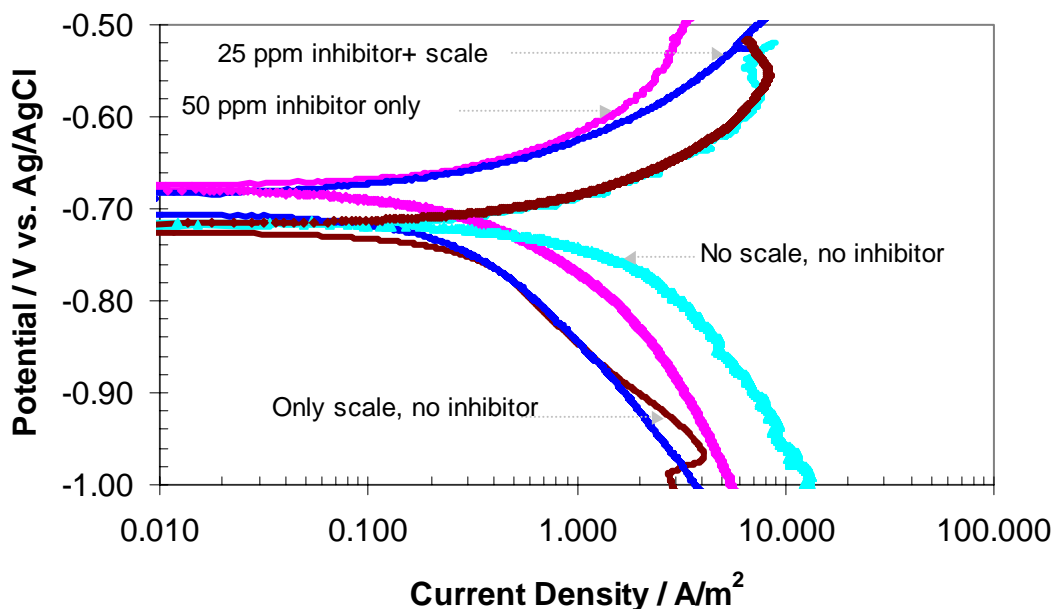


Figure 38. Comparison of Polarization curves with inhibitor A for pH 6.60, T = 80 °C, stagnant conditions.

### 5.3.2 Interactions at supersaturation of 30

The supersaturation of the solution was lowered to test the inhibitor scale interaction under lower iron carbonate precipitation rates. In this set of experiments, 25 ppm of inhibitor B is added to the solution that is at an initial supersaturation of 30. Since we were in search of a potential antagonistic interaction between the inhibitor and the scale, a concentration of inhibitor that was partially protective was chosen. From Figure 15, it is seen that 25 ppm of inhibitor B fitted our criteria very well.

#### *Inhibitor B added at the beginning*

These experiments were designed to see the interaction of the inhibitor and the iron carbonate scale when both the processes would compete for adsorption on the metal surface.

In the experiment shown in Figure 39, a supersaturation of 30 was achieved in the beginning by adjusting the pH to 6.60 and adding 10 ppm of  $\text{Fe}^{++}$ . Subsequently 25 ppm inhibitor B was added after 30 minutes. The figure shows the comparison between the experiments with

- Only 25 ppm inhibitor B
- Only iron carbonate scale
- 25 ppm inhibitor added under scaling conditions.

It can be seen that when 25 ppm inhibitor added under scaling conditions, decrease in the corrosion rate is faster than seen in the other two conditions. However, from the logarithmic graph of the above experiment (Figure 40), it is noticed that the final corrosion rate is similar to that without the inhibitor.

From the top view of the sample (Figure 41), it can be seen that very little iron carbonate is seen on the surface of the metal. Therefore, it seems that the metal surface is mainly protected due to the presence of the inhibitor. Adding 25 ppm of inhibitor B seems to hamper the growth of iron carbonate on the surface of the metal.

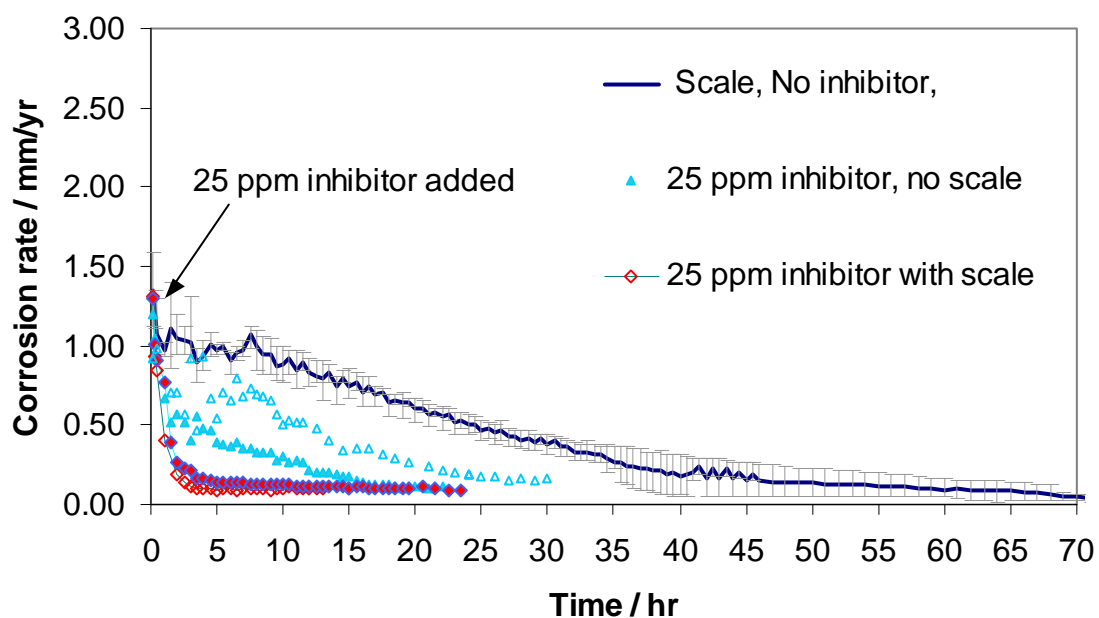


Figure 39. Effect of addition of 25 ppm inhibitor B added after 0.5 hr. on corrosion rate for pH 6.60,  $Fe^{++} = 10$  ppm, SS = 30, T = 80 °C, stagnant conditions. Same symbol shapes depict repetitions of the same experiments.

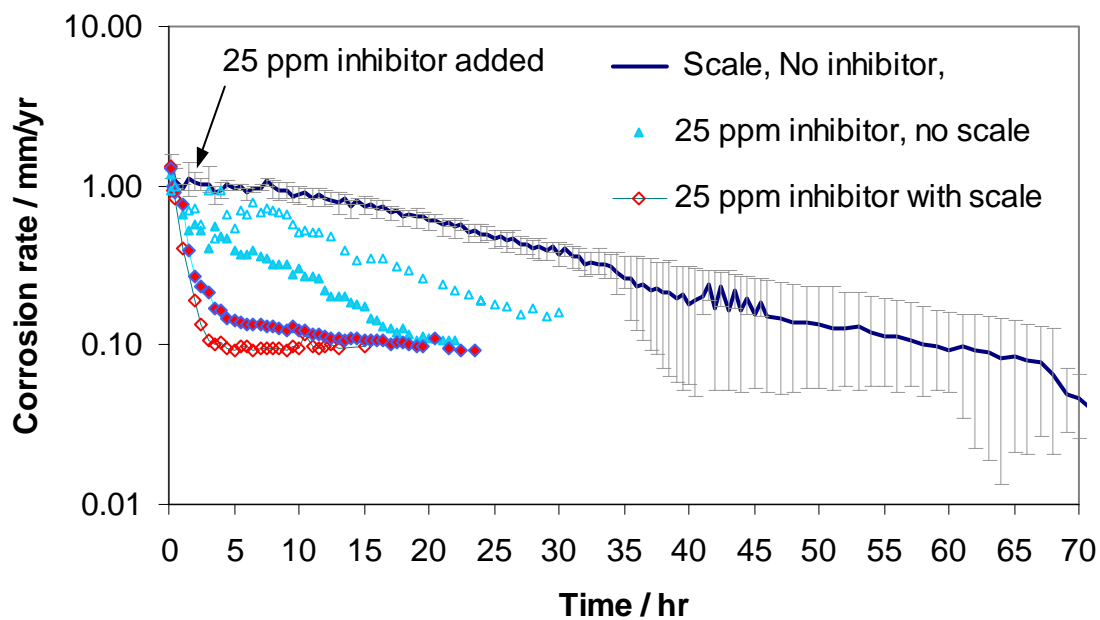


Figure 40. Effect of addition of 25 ppm inhibitor B added after 0.5 hr. on corrosion rate for pH 6.60,  $\text{Fe}^{++} = 10$  ppm, SS = 30,  $T = 80$  °C, stagnant conditions. Same symbol shapes depict repetitions of the same experiments.

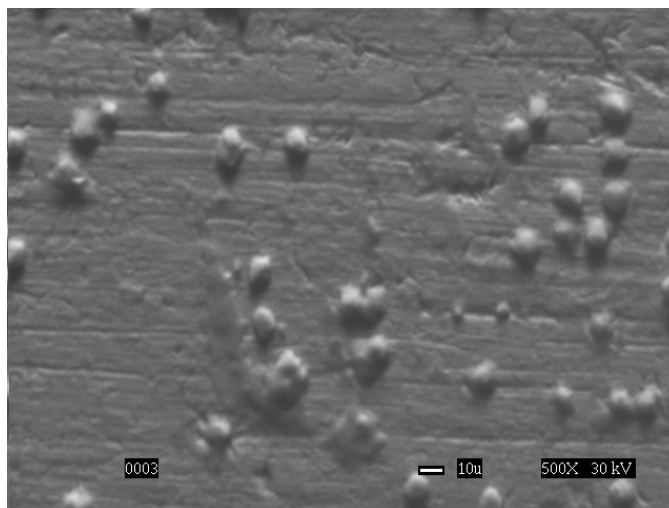


Figure 41. The Front view of sample at 500X when 25 ppm inhibitor B is added after 0.5 hr for pH 6.60,  $\text{Fe}^{++} = 10$  ppm, SS = 30,  $T = 80$  °C, stagnant conditions.

As it was observed that when the inhibitor is added in the beginning, the inhibitor hampers the precipitation of the scale, it was decided to study the effect of the inhibitor at an even lower concentration, to see whether it could prevent the scale formation while at the same time not inhibit corrosion. This condition could be a catastrophic scenario for the pipeline. Hence, an experiment was conducted in which 10 ppm of inhibitor B was added to the solution initially at supersaturation of 30. From the logarithmic graph shown in the Figure 42, it is observed that there is no corrosion inhibition due to the inhibitor, and the inhibitor has no affect on the scale formation. The same conclusion could be reached by observing the top and cross-sectional view of the scale (Figure 43). The sudden drop in the corrosion rate after 50 hours could not be explained.

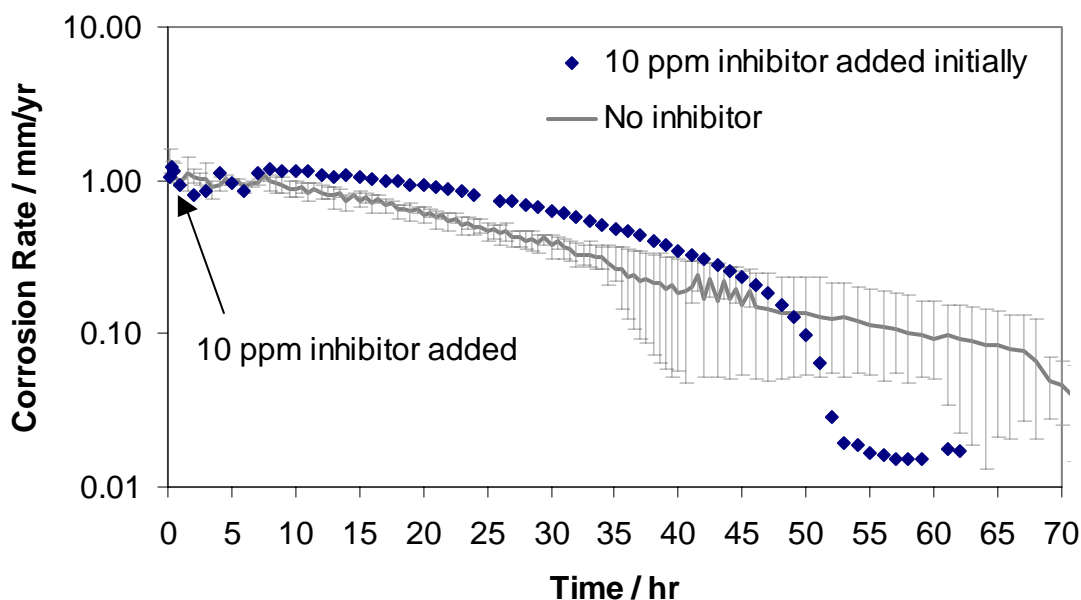


Figure 42. Effect of addition of 10 ppm inhibitor B added after 0.5 hr. on corrosion rate for pH 6.60,  $Fe^{++} = 10$  ppm, SS = 30, T = 80 °C , stagnant conditions.

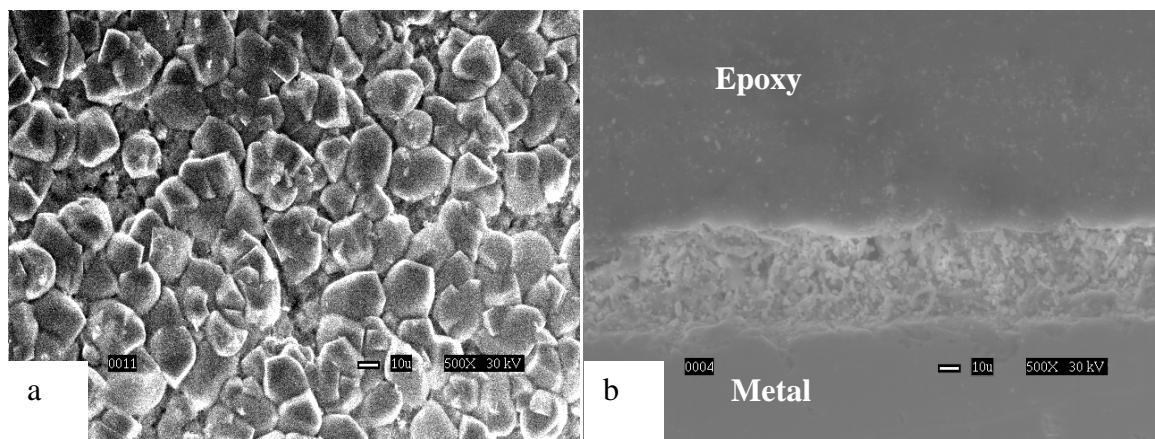


Figure 43. The top view (a) and the cross-sectional view (b) of sample with 10 ppm inhibitor B added immediately, for pH 6.60,  $\text{Fe}^{++} = 10$  ppm, SS = 30,  $T = 80$  °C, stagnant conditions.

Inhibitor B added after 35 hours

In these set of experiments, 25 ppm of inhibitor was added after 35 – 40 hours of starting the experiment that was at an initial supersaturation of 30. Comparison of the experiments with and without inhibitor is shown in Figure 44. It is seen that as soon as the inhibitor is added, the corrosion rate decreases drastically. However, from the logarithmic graph of the same experiment (Figure 45), it is noticed that the final corrosion rate remains similar. From the top and the cross-sectional view of the sample Figure 46, a porous iron carbonate scale of thickness 10  $\mu\text{m}$  is observed.

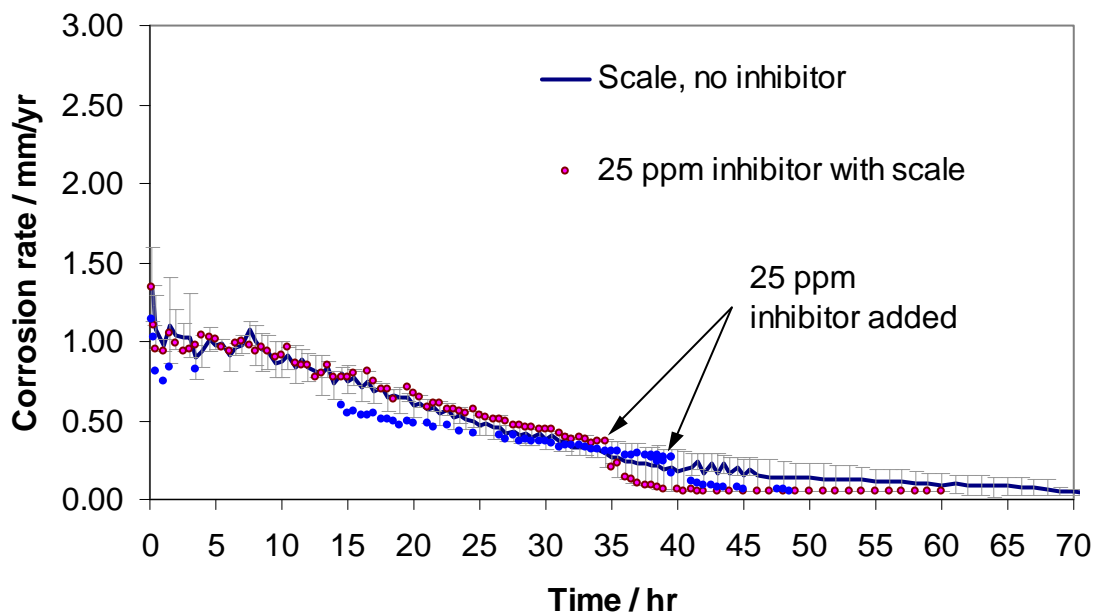


Figure 44. Effect of addition of 25 ppm inhibitor B added after 35 hr. on corrosion rate for pH 6.60,  $\text{Fe}^{++} = 10$  ppm, SS = 30, T = 80 °C, stagnant conditions. Same symbol shapes depict repetitions of the same experiments.

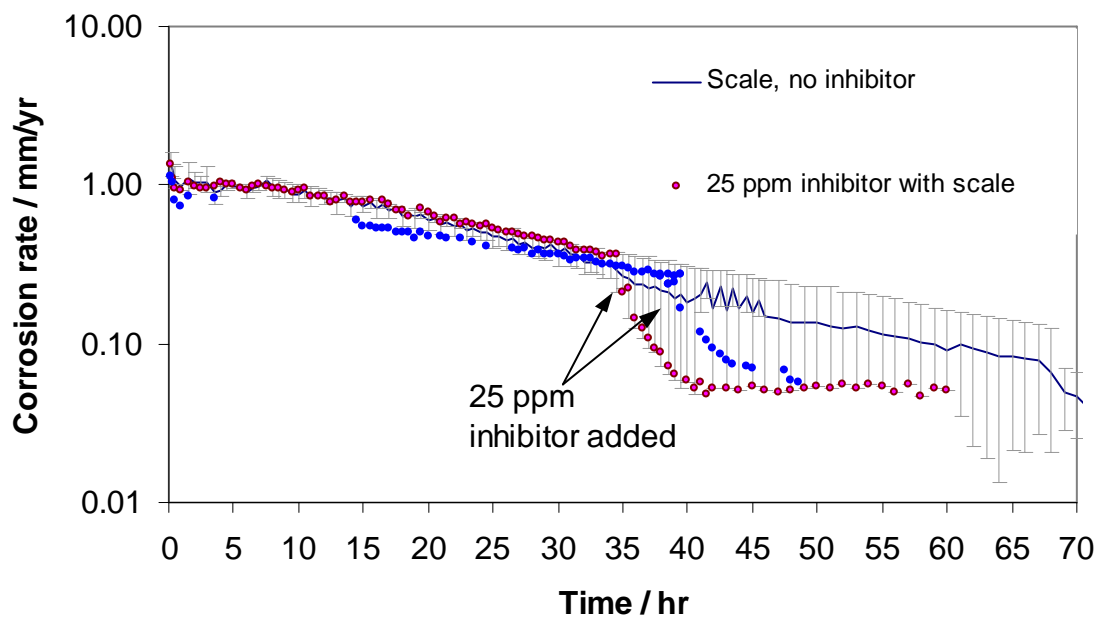


Figure 45. Effect of addition of 25 ppm inhibitor B added after 35 hr. on corrosion rate for pH 6.60,  $\text{Fe}^{++} = 10$  ppm, SS = 30,  $T = 80$  °C, stagnant conditions. Same symbol shapes depict repetitions of the same experiments.

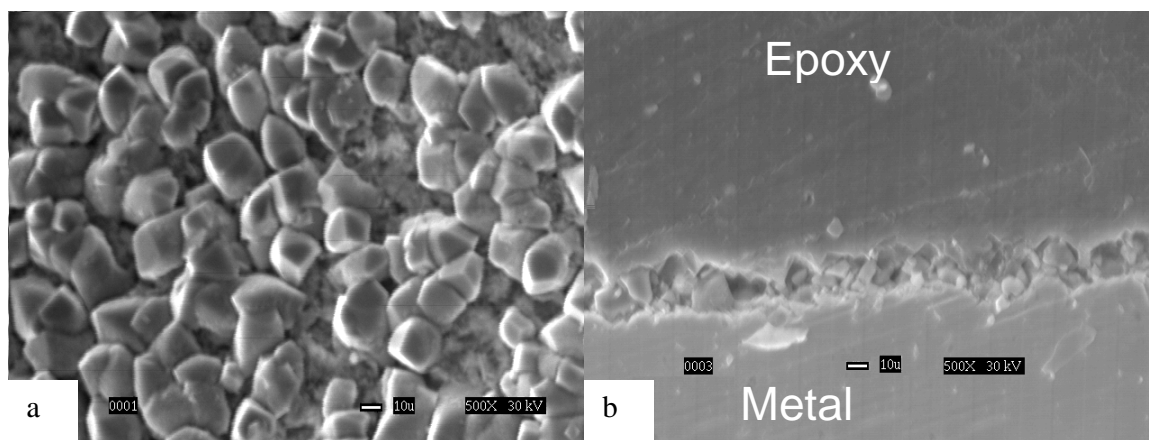


Figure 46. The Front view (a) and the cross-sectional view (b) of sample at 500X when 25 ppm inhibitor B is added after 35 hr for pH 6.60,  $\text{Fe}^{++} = 10$  ppm, SS = 30,  $T = 80$  °C, stagnant conditions.

The potentiodynamic sweeps for the experiments done at the supersaturation of 30 are shown in Figure 47 & Figure 48. In the presence of the only iron carbonate scale the corrosion rate is decreased mainly due to the inhibition of the cathodic reaction, while the anodic reaction is not inhibited as much. In presence of only inhibitor B, both the cathodic and the anodic reactions are inhibited. When inhibitor and the iron carbonate scale both are present, both reactions are inhibited and the sweep is similar to one with only inhibitor.

Pseudo polarization plot of experiment in which inhibitor was added after 40 hours is shown in Figure 49. It is seen that in the absence of the inhibitor, the potential decreases steadily with time, but after 40 hours when the inhibitor is added, the potential jumps up initially and subsequently decreases the corrosion rate.

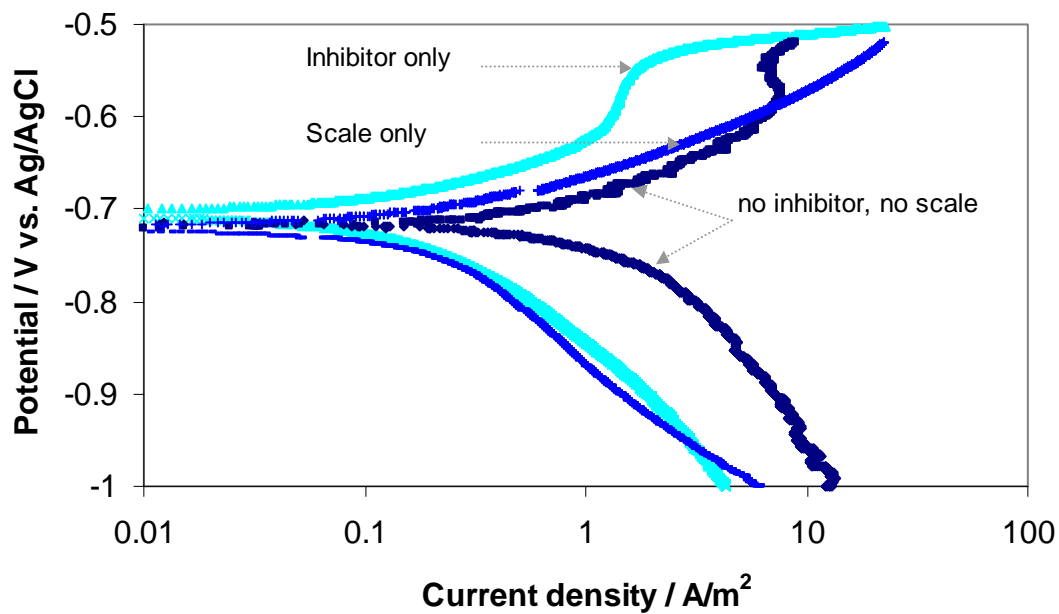


Figure 47. Potentiodynamic sweeps for pH 6.60,  $\text{Fe}^{++} = 10$  ppm, SS = 30, 25 ppm inhibitor B,  $T=80^\circ\text{C}$ , stagnant conditions.

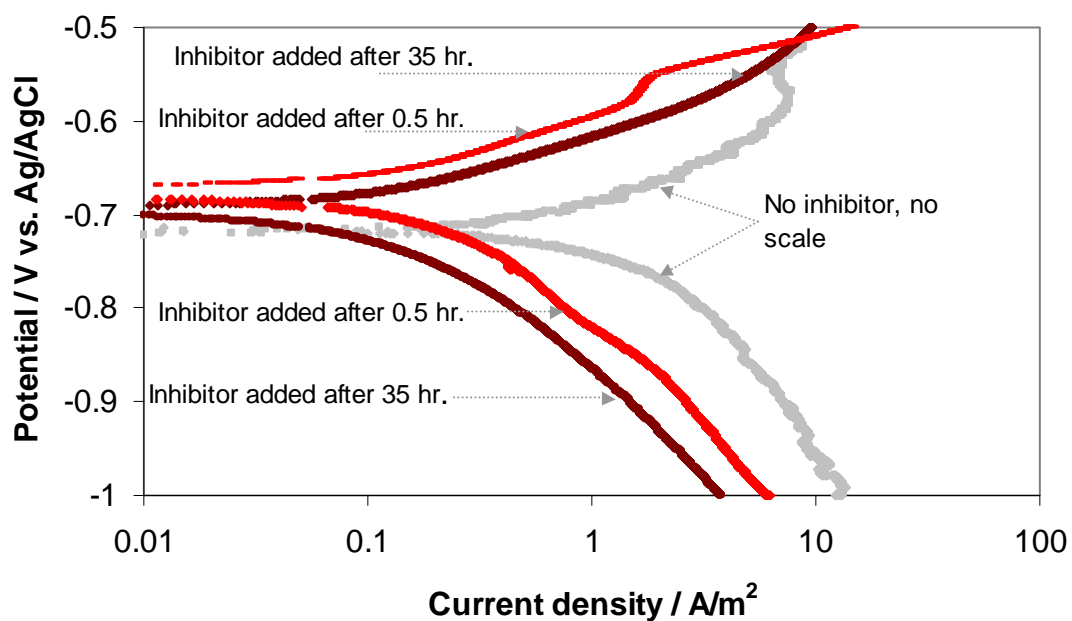


Figure 48. Potentiodynamic sweeps for pH 6.60,  $\text{Fe}^{++} = 10$  ppm, SS = 30, 25 ppm inhibitor,  $T = 80^\circ\text{C}$ , stagnant conditions.

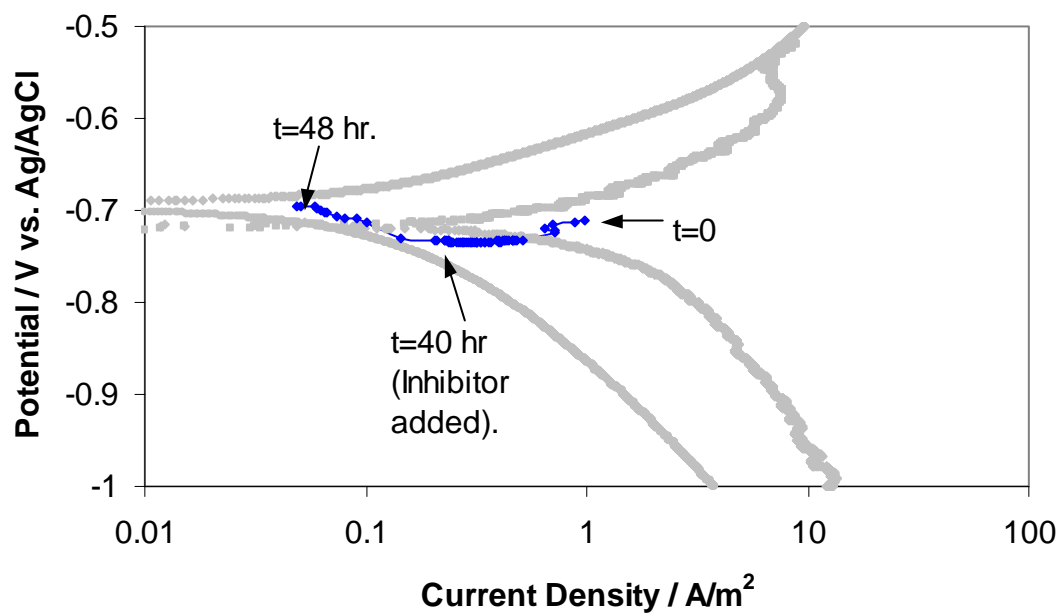


Figure 49. Pseudo polarization plot when 25 ppm inhibitor B is added after 40 hr for pH 6.60, Fe<sup>++</sup> = 10 ppm, SS = 30, T = 80°C, stagnant conditions.

### 5.3.3 Interactions at supersaturation of 7

Experiments at supersaturation of 7 were done to test the inhibitor-scale interaction at even slower iron carbonate precipitation rate. In this experiment, the inhibitor was added after creating a very porous iron carbonate scale (Figure 28). Supersaturation of 7 was achieved in the beginning by adjusting the pH to 6.30 and adding 10 ppm of  $\text{Fe}^{++}$ . Subsequently, 25 ppm inhibitor B was added after 47 hours. From the comparison of the experiments with and without inhibitor (Figure 50), it is seen that as soon as the inhibitor is added, the corrosion rate decreases and no antagonistic behavior is observed. On observing the scale (Figure 51), it was found that the porosity of the scale was very similar to that of one without inhibitor.

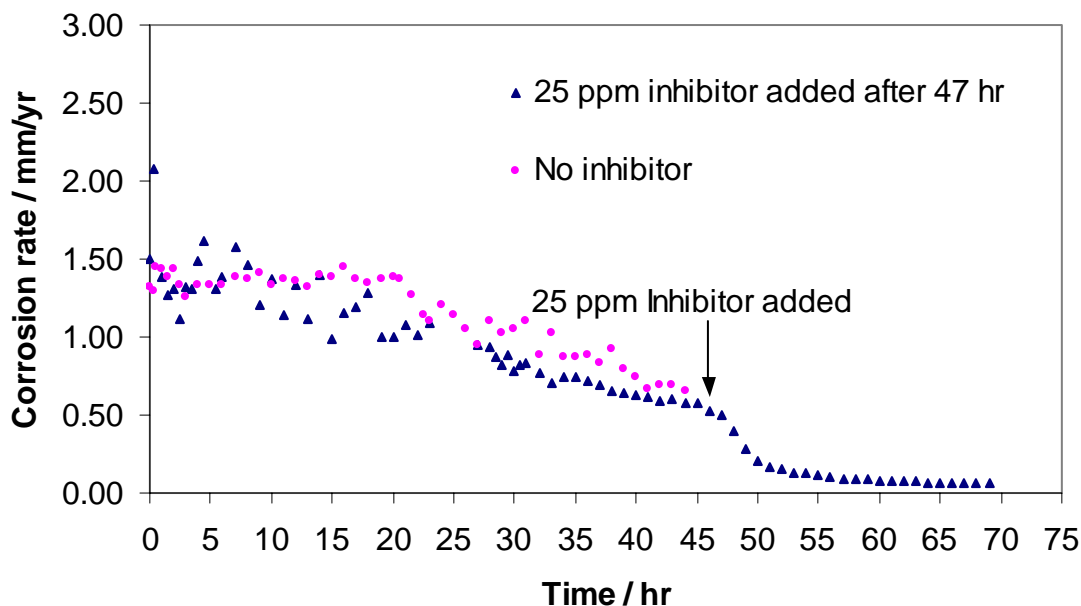


Figure 50. Change in corrosion rate with time when inhibitor B is added after 47 hours, at pH 6.30,  $\text{Fe}^{++} = 10$  ppm, SS = 7, T = 80 °C, stagnant conditions.

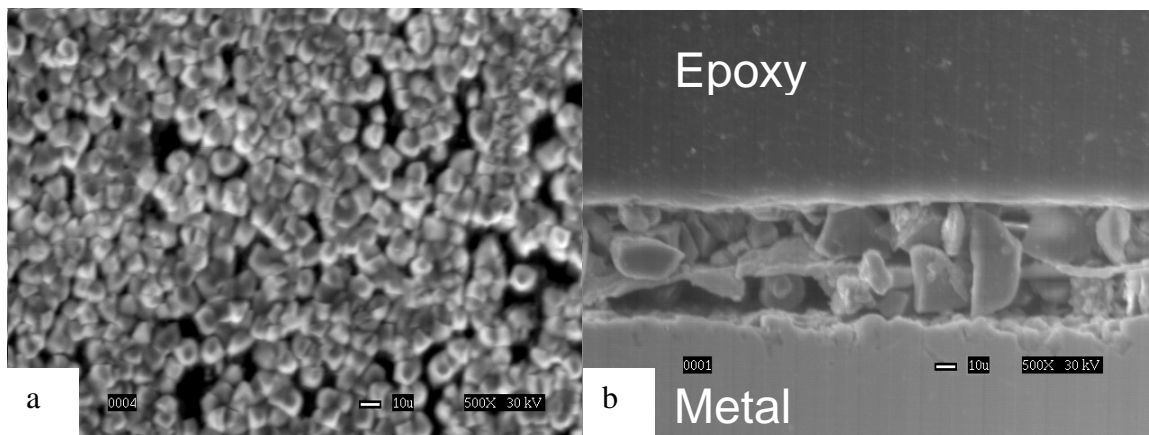


Figure 51. The top view (a) and the cross-sectional view (b) of sample at 500X when 25 ppm inhibitor B is added after 47 hr. for pH 6.30,  $Fe^{++} = 10$  ppm, SS = 7, T = 80 °C, stagnant conditions.

## 5.4 Analysis and Modeling

### 5.4.1 Comparison of the experimental results with the OU model

The results seen in Figure 29 were simulated using the OU model. The results obtained are shown in Figure 52. It is seen that although the model has a higher initial corrosion rate, the trend shown by the model and the final corrosion rate is in good agreement. The OU model was also used to predict the thickness of the iron carbonate scale for different conditions. Figure 53 - Figure 56 show the comparison between the predicted and the experimental results for different conditions. It is seen that the results were in good agreement with each other.

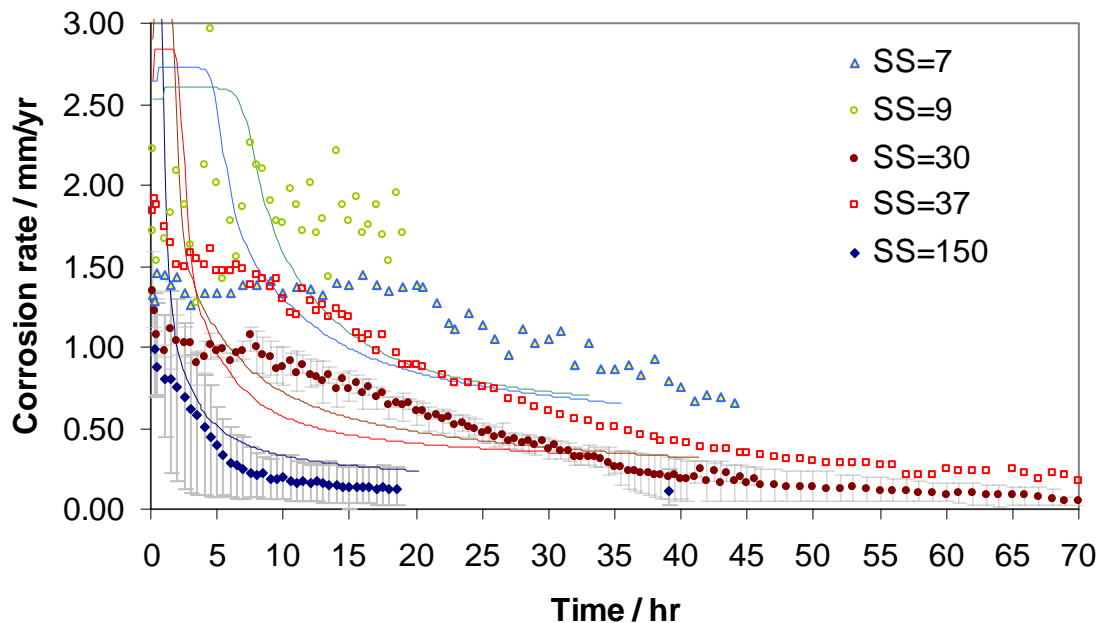


Figure 52. Comparison of experimental results with OU model at  $T=80^{\circ}\text{C}$ . (Data points indicate experimental results and lines indicate OU model)

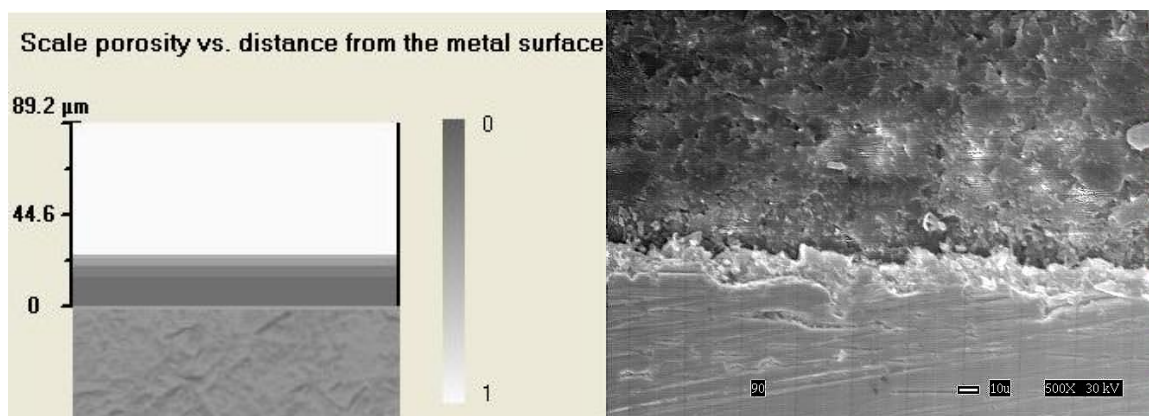


Figure 53. Predicted and experimentally measured iron carbonate scale thickness, at pH = 6.60,  $\text{Fe}^{++} = 50$  ppm, SS = 150, no inhibitor, T = 80°C.

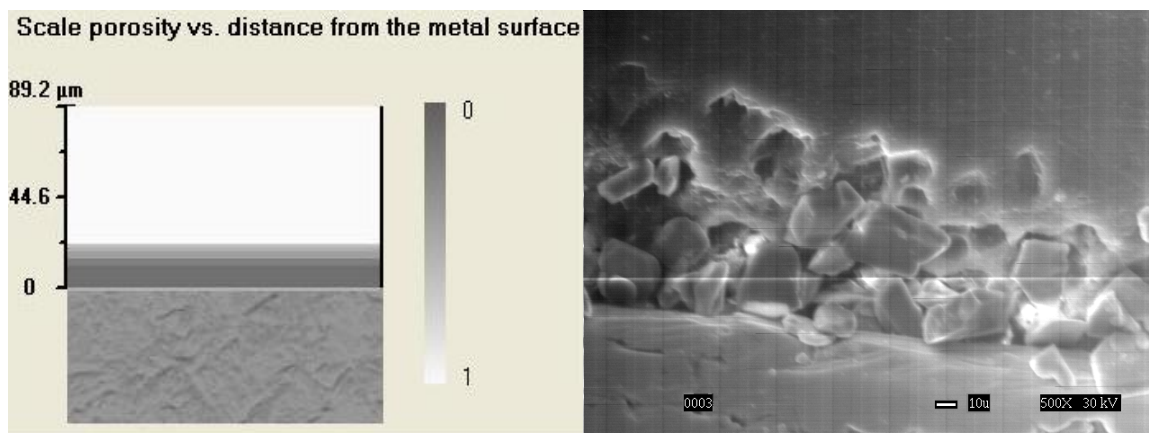


Figure 54. Predicted and experimentally measured iron carbonate scale thickness, at pH = 6.60,  $\text{Fe}^{++} = 10$  ppm, SS = 30, no inhibitor, T = 80°C.

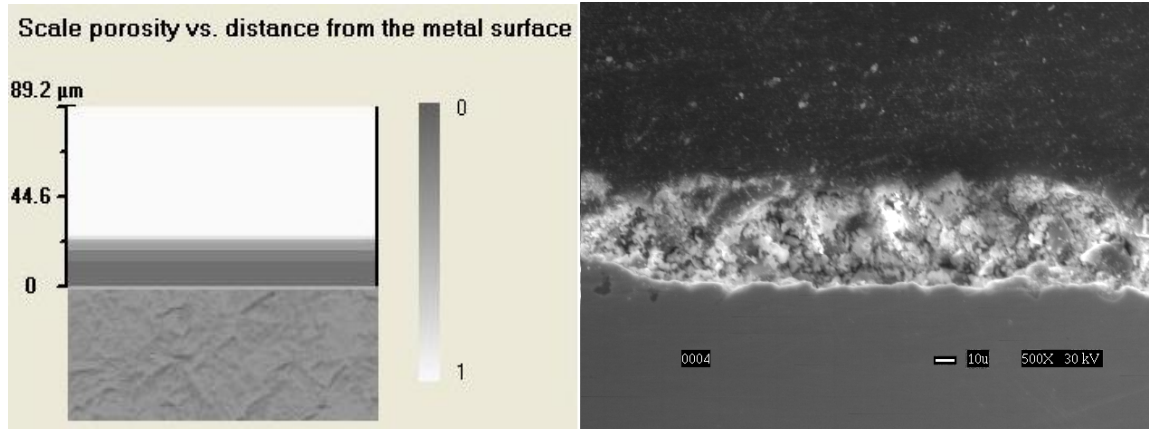


Figure 55. Predicted and experimentally measured iron carbonate scale thickness, at pH = 6.30,  $\text{Fe}^{++} = 50$  ppm, SS = 37, no inhibitor, T = 80°C.

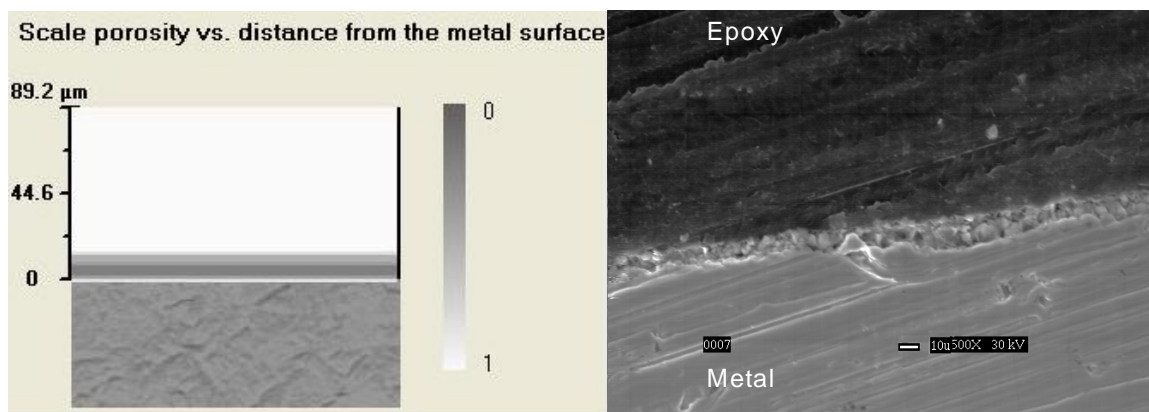


Figure 56. Predicted and experimentally measured iron carbonate scale thickness, at pH = 6.30,  $\text{Fe}^{++} = 10$  ppm, SS = 7, no inhibitor, T = 80°C.

#### 5.4.2 Modeling of inhibition

The inhibition was modeled using the results obtained from the experiments with different concentrations of inhibitors at pH 6.00 and pH 6.60. Based on the final corrosion rate of the metal at a given inhibitor concentration, coverage ( $\theta$ ) was found out using the following equation:

$$\theta = \frac{CR_{uninhibited} - CR_{inhibited}}{CR_{uninhibited}} \quad (5-1)$$

$CR_{uninhibited}$  - Corrosion rate of uninhibited system

$CR_{inhibited}$  - Corrosion rate of inhibited system

Inhibition is most often characterized by the use of adsorption isotherms. Some of the most important isotherms are: Langmuir isotherm, Temkin isotherm, Frumkin isotherm, Flory-Huggins isotherm etc. The Frumkin isotherm for adsorption equilibrium can be represented in a general form as (Drazic and Drazic, 1990) :

$$Kc = \frac{\theta}{n(1-\theta)^n} \exp(-2a\theta) \quad (5-2)$$

where,

$K$  is equilibrium constant,  $c$  is concentration of the inhibitor,  $a$  is constant characterizing the interaction of the adsorbed inhibitor species,  $n$  is number of desorbed water molecules replaced by inhibitor,  $\theta$  is coverage.

This equation can be simplified by assuming exactly one inhibitor molecule replaces desorbed inhibitor ( $n = 1$ ), and there is very high coverage ( $\theta = 1$ ). After simplification we get the following equation:

$$\theta = 1 - \frac{\exp(-2a)}{Kc} \quad (5-3)$$

This simplified Frumkin isotherm has been used in the OU model for prediction of inhibition. The comparison between the general and the simplified Frumkin adsorption isotherm is shown in the Figure 57. Although the general Frumkin isotherm is in a better agreement, it is seen that both type of isotherms predict the experimental results very well.

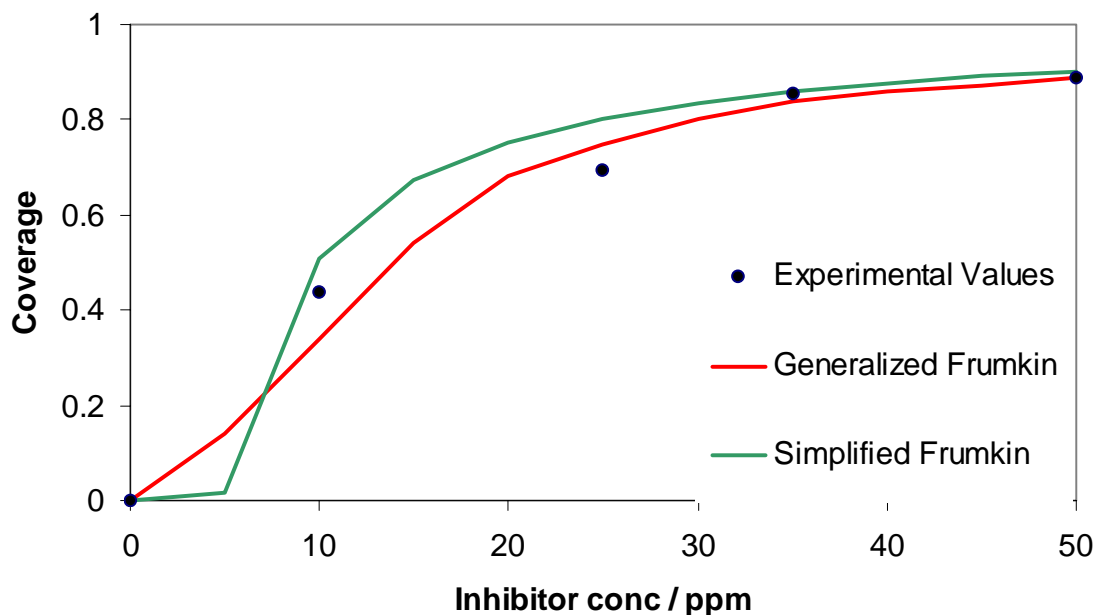


Figure 57. Comparison of the experimental results for inhibitor, with the generalized and simplified Frumkin isotherm

### 5.4.3 Modeling of inhibitor-scale interaction

From the experimental results it was observed that the presence of inhibitors hampered the growth of iron carbonate scale. This was initially attributed to the scale inhibition properties of the inhibitor. A brief literature review of the scale inhibitors was done and presented in Chapter 2. However, on deeper analysis it was found that the scarcity of  $\text{Fe}^{++}$  on the surface of the metal could be one of the major factors affecting scale formation. The analysis is explained in the following paragraphs.

Under all the experimental conditions, the initial supersaturation was in the range of 7 – 150. As soon as the metal surface is exposed to the solution, the iron carbonate starts precipitating on it. Formation of iron carbonate leads to a drop in the concentration of iron and carbonate ions at the metal surface. The corrosion occurring under the porous iron carbonate scale (undermining process) and the diffusing  $\text{Fe}^{++}$  from the bulk solution replenish the lost  $\text{Fe}^{++}$  at the metal surface.

In the presence of the inhibitors, the corrosion rate of the metal decreases and the diffusion of  $\text{Fe}^{++}$  from the bulk solution remains the only source of ions for precipitation at the metal surface. Since, the precipitation of the iron carbonate is much faster than the rate of transportation of  $\text{Fe}^{++}$  from the bulk of the solution to the surface, the precipitation becomes diffusion-controlled. This leads to slightly more acidic conditions at the metal surface and consequently the supersaturation and the precipitation of iron carbonate decreases.

The above phenomenon can be simulated using the OU MULTICORP model. The model was run for 15 hours under the following conditions: pH 6.60,  $\text{Fe}^{++}$  concentration

of 50 ppm, SS = 150, T = 80 °C. One simulation was run each with inhibitor (assuming 99% efficiency) and without inhibitor. It is seen that in the presence of the inhibitor the  $\text{Fe}^{++}$  concentration (Figure 58) as well as the pH (Figure 59) near the surface of the metal is lower than that in the absence of the inhibitor. This would lead to a lower supersaturation and a slower precipitation rate near the metal surface when the inhibitor is added. From the comparison of the scales obtained using the model (Figure 60), it is seen that the thickness of the iron carbonate scale formed in the presence of the inhibitor is about 25% of the scale thickness formed in the absence of the inhibitor.

Hence, in the absence of corroding conditions at the metal surface, there would be less or no scale formed at the surface. Similar phenomenon was also observed in a series of experiments performed at the corrosion center, on stainless steel (Sun, 2004). At a supersaturation of 30, it was found that even after 3 days no iron carbonate scale was formed on the surface of steel. In an experiment done at supersaturation of 150, scale precipitated on stainless steel was approximately 50% of that compared to corroding mild steel.

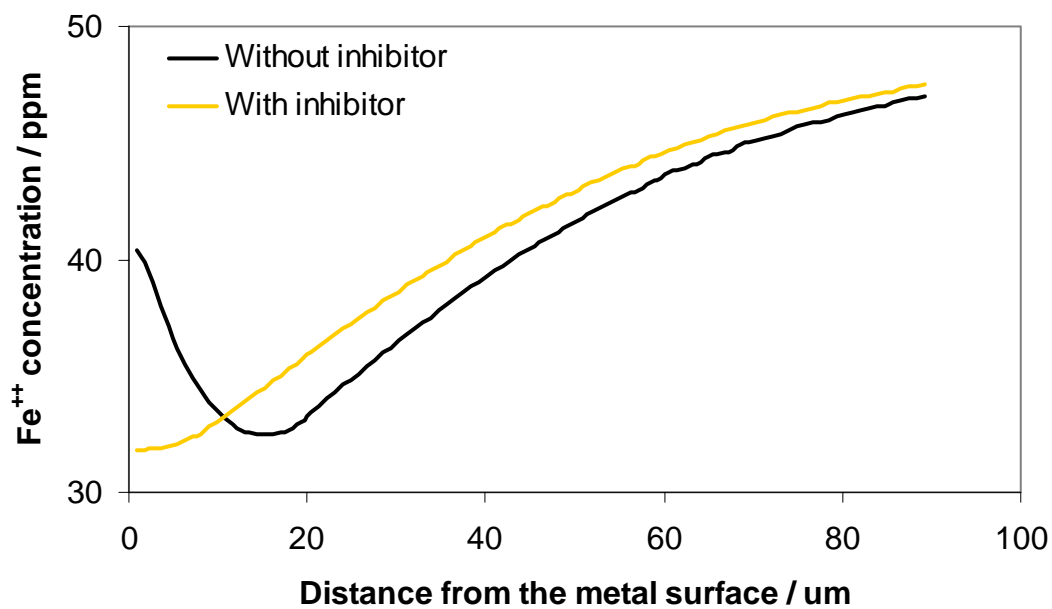


Figure 58. Fe<sup>++</sup> concentration profile with and without the inhibitor obtained using the OU model at pH 6.60, Fe<sup>++</sup> = 50 ppm, SS = 150, T = 80 °C.

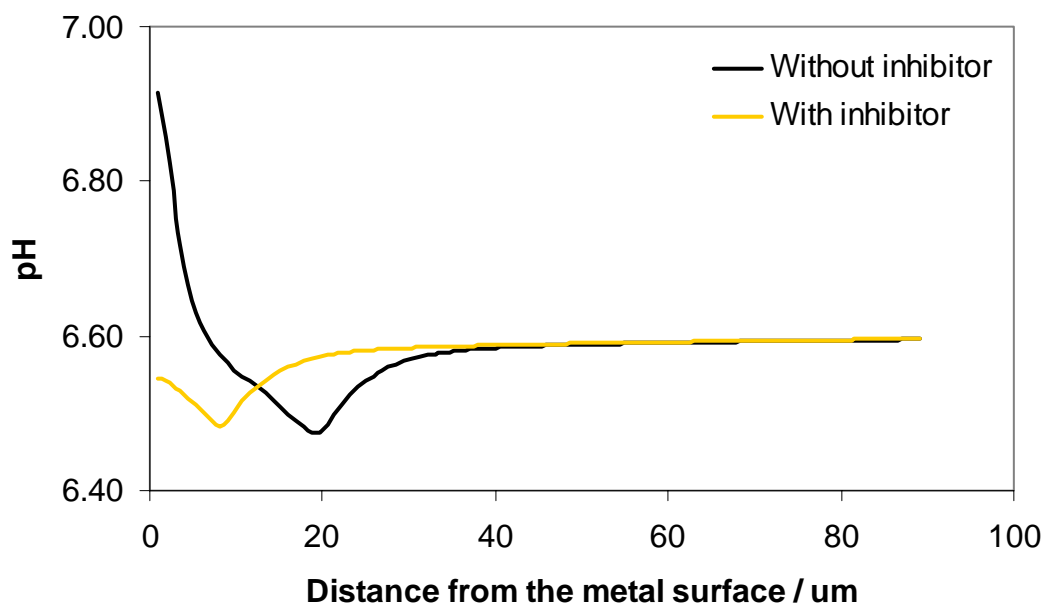


Figure 59. pH profile with and without the inhibitor obtained using the OU model at pH 6.60, Fe<sup>++</sup> = 50 ppm, SS = 150, T = 80 °C.

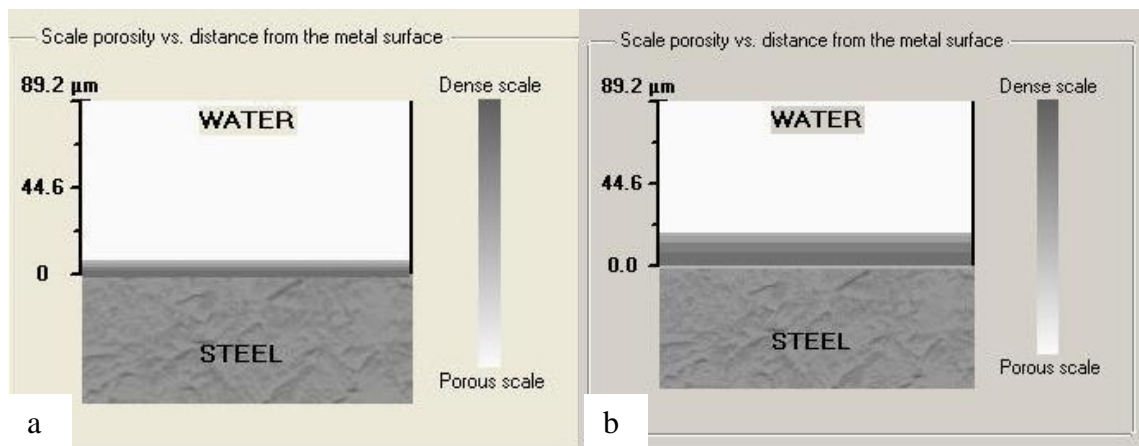


Figure 60. Comparison of the iron carbonate scale obtained (a) with and (b) without inhibitor using the OU model at pH 6.60,  $Fe^{++} = 50$  ppm,  $T = 80$  °C.

From the above analysis, it is deduced that scarcity of  $Fe^{++}$  at the metal surface might be the primary reason the growth of scale is hampered. However, since the model predicts formation of some scale on the metal surface in the presence of the inhibitors, and there was no scale formed on the metal surface. Hence it was speculated that hampering of scale formation could also be due to the scale inhibition properties of the inhibitor.

Hence, the poisoning of the growth of iron carbonate scale after addition of the inhibitor might be due to scarcity of  $Fe^{++}$  at the metal surface and/or scale inhibition properties of the inhibitor.

## CHAPTER 6: CONCLUSIONS

The interaction between the inhibitor film and the iron carbonate scale has been studied in a glass cell under scaling conditions. The interaction was tested using various concentrations of two imidazoline-based inhibitors between the supersaturation ranges of 7 – 150. Based on the experimental conditions, the main research findings of both the experimental work and modeling work are:

- Both inhibitor A and inhibitor B function by slowing down anodic as well as cathodic reactions, although the anodic more than the cathodic.
- Above a certain threshold concentration, both inhibitors hamper the growth of the iron carbonate scale. This could be a result of scarcity of  $\text{Fe}^{++}$  at the surface of the metal and/or scale inhibition properties of the inhibitor.
- No conditions under which inhibitor and scale interacts in an antagonistic manner were found. i.e. under none of the conditions investigated, did a combination of inhibitor and iron carbonate scale fail to reduce the corrosion rate.
- The experiments done in the absence of inhibitors was simulated using the OU model. The OU model was found to be in good agreement with the experiment results. The OU model was also able predict the thickness of the iron carbonate scale formed on the surface of the metal very well.

## CHAPTER 7: FUTURE WORK

Some suggestions for the future work to refine and extend the current research are as follows:

- Experiments done by keeping the pH and the  $\text{Fe}^{++}$  concentration in the bulk solution constant, instead of initially fixing the pH and the  $\text{Fe}^{++}$  concentration and allowing it to drift with time. This could lead to a better understanding of the precipitation kinetics of the iron carbonate film.
- Formation of the iron carbonate scale and the inhibitor –scale interaction could be monitored *in-situ* adapting the system and by inserting an optical microscope in the system.
- This work could be extended to lower pH where iron carbide films could be dominant. This could help in studying the interaction of the inhibitor with the iron carbide as well as iron carbonate films, under controlled environments.
- The interaction of the inhibitor and the sulfide film could also be tested. These experiments could be interesting since the sulfide film is conductive and could lead to change in the coverage of the inhibitor.

## REFERENCES

1. Arieh Ben-Naim, *Hydrophobic interactions*, Plenum press, 1980, p.164.
2. Amjad Z., "The influence of Polyphosphates, Phosphonates, and Poly(carboxylic acids) on the crystal growth of Hydroxyapatite," *Langmuir*, 3, (1987): p. 1063.
3. V. J. Drazic and D. M. Drazic, "Influence of the metal dissolution rate on the Anion and inhibitor adsorption", *Proc. 7<sup>th</sup> European Symposium on Corrosion Inhibitors (7SEIC): Ann. Univ. Ferrara, N.S., Sez. V, Suppl. N. 9, 1990 (Ferrara, 1990)*, p.99.
4. Dugstad Arne, "The importance of  $\text{FeCO}_3$  supersaturation on the  $\text{CO}_2$  corrosion of carbon steels," *CORROSION/92*, paper no.14, (Houston, TX: NACE International, 1992).
5. Dugstad Arne, Lunde L., Videm K., "Parametric testing of  $\text{CO}_2$  corrosion of carbon steel," *CORROSION/94*, paper no.14, (Houston, TX: NACE International, 1994).
6. Durnie W. H., B.J. Kinsella, R. De Marco and A. Jefferson, "A study of the adsorption properties of commercial carbon dioxide corrosion inhibitor formulations," *Journal of Applied Electrochemistry*, 31 (2001): p.1221.
7. Edwards A., C. Osbourne, S. Webster, D. Klenerman, M. Joseph, P. Ostovar and M. Doyle, "Mechanistic studies of the corrosion inhibitor oleic imidazoline", *Corrosion Science*, Vol.36, No.2, (1994): p.315.
8. Glasner A. and S. Skurkik, "Speculations on a new mechanism of crystal growth from aqueous solutions," *Israel J. Chem*, Vol. 7, (1969), p. 633.
9. Gulbrandsen E., S. Nestic, A. Stangeland, T Buchardt, B. Sundfaer, S. M. Hesjevik, S. Skjerve "Effect of precorrosion on the performance of inhibitors for  $\text{CO}_2$  corrosion of carbon steel," *CORROSION/1998*, paper no. 013, (Houston, TX: NACE International, 1998).
10. Israelachvili J, *Intermolecular and surface forces*, Academic press, 1985, p. 249.
11. Johnson M. L., M. B. Tomson, "Ferrous carbonate precipitation kinetics and its impact on carbon dioxide corrosion", *CORROSION/91*, paper no.268. (Houston, TX: NACE International, 1991).
12. Kermani M. B. and A. Morshed, "Carbon dioxide corrosion in oil and gas production-a compendium," *Corrosion*, Vol.59, No. 8, (2003): p.659.

13. Malik H., "Influence of C16 Quaternary amine on surface films and polarization resistance of mild steel in carbon dioxide saturated 5% sodium chloride," *Corrosion*, Vol.51 (1995): p.321.
14. Mansfeld F, *Corrosion Mechanisms*, Marcel Dekker, New York, 1987, p. 119.
15. R. De Marco, W. Durnie, A. Jefferson, B. Kinsella and A Crawford, "Persistence of carbon dioxide corrosion inhibitors," *Corrosion*, Vol.58, (2002): p.354.
16. Miura M., S. Otani, M. Kodama and K. Shinagawa, *J. Phys. Chem*, 66, (1962): p. 252.
17. Mueller E., C.S. Sikes, and B. J. Little, "Peptide interactions with steel surfaces: inhibition of corrosion and calcium carbonate precipitation," *Corrosion Science*, Vol. 49, No. 10, (1993): p. 829.
18. Nafday Omkar, "Film formation and CO<sub>2</sub> corrosion in the presence of acetic acid," Sep. 2003, Board meeting report, Ohio University.
19. Naono H., *Bull. Chem. Soc. Japan*, 40, (1967): p. 1104.
20. Nestic S., W. Wilhelmsen, S. Skjerve and S. M. Hesjevik "Testing of inhibitors for carbon dioxide corrosion using the electrochemical techniques," *Proceedings of the 8<sup>th</sup> European Symposium on Corrosion Inhibitors*, Ann. Univ. Ferrara, N.S., Sez. V, Suppl. N. 10, (1995): p.1163.
21. Nestic S. Lee K.L.J., Ruzic V, "A mechanistic model of iron carbonate film growth and the effect on CO<sub>2</sub> corrosion of mild steel," *Corrosion/2002*, paper no. 02237, (Houston, TX: NACE International, 2002).
22. Otani S., *Bull. Chem. Soc. Japan*, 33, (1960): p. 1549.
23. Porter M. R., *Handbook of surfactants*, Chapman and Hall, New York, 1991, p. 25.
24. Ramachandran S., Bao-Liang Tsai, Mario Blanco, Huey Chen, Yongchun Tang and William A. Goddard, "Self-Assembled monolayer mechanism for corrosion inhibition of iron by imidazolines," *Langmuir* 12, (1996): p. 6419.
25. Ramachandran S., Bao-Liang Tsai, Mario Blanco, Huey Chen, Yongchun Tang and William A. Goddard, "Atomistic simulations of oleic imidazolines bound to ferric clusters," *J. Phy. Chem.* Vol.101, (1997): p. 83.

26. Ramachandran S., V. Jovancicevic and Y. S. Han, "Using Reaction engineering to compare corrosion inhibitor performance in laboratory and field experiments," CORROSION/2001, paper no. 01027, (Houston, TX: NACE International, 2001).
27. Roberge Pierre, *Handbook of corrosion Engineering*, McGraw Hill. 1999.
28. Sarig S. and M. Raphael, "The inhibiting effect of Polyphosphates on the crystallization of strontium sulfate," *J. Crystal growth*, 16, (1972): p. 203.
29. Sarig S., "Crystal habit modification by water soluble polymers," *J. Crystal Growth*, 24/25, (1974): p. 338.
30. Sun Wei, "Kinetics of scale formation in CO<sub>2</sub>/H<sub>2</sub>S solution," Sep. 2003, Board meeting report, Ohio University.
31. Tan Y. J., S. Bailey and B. Kinsella, "An investigation of the formation and destruction of corrosion inhibitor films using electrochemical impedance spectroscopy (EIS)," *Corrosion Science*, Vol.38, No. 9, (1996): p. 1545.
32. Van Hunnik E.W.J, B.F.M. Pots and E.L.J.A. Hendriksen, "The formation of protective FeCO<sub>3</sub> corrosion product layers in CO<sub>2</sub> corrosion," CORROSION/96, paper no. 6, (Houston, TX: NACE International, 1996).
33. Jovancicevic V., S. Ramachandran, and P. Prince, "Inhibition of Carbon Dioxide Corrosion of Mild Steel by Imidazolines and their precursors," *Corrosion*, Vol.55, 1999, p. 449.
34. Shiliang H., A. T. Kan, M. B. Tomson, "Inhibition of Calcium carbonate precipitation in NaCl brines from 25 to 90 °C," *Applied Geochemistry*, 14, (1999): p. 17.
35. Shiliang H., J. Oddo and M. B. Tomson, "The nucleation kinetics of Strontium Sulfate in NaCl solutions up to 6 m and 90 °C with or without inhibitors," *Journal of Colloid and interface science*, 174, (1995): p. 327.
36. Sun W., *personal communication*. Ohio University. (2004)
37. Xyla. G., Giannimaras. E, and Koutsoukos. P, "The precipitation of calcium carbonate in aqueous solutions," *Colloids and Surfaces*, 53, (1991): p. 241.
38. Zhang. J. W, Nancollas G. H, In *Mineral-Water Interface Geochemistry*; Hochella. M. F, Jr., White. A. F, ;Eds.; Reviews in Minerology; Mineralogical Society of America: Washington DC. 1990; Vol. 23, p. 365.

39. Zhang X., F. Wang, Y. He, Y. Du, "Study of the inhibitor mechanism of imidazoline amide in carbon dioxide of Armco iron," *Corrosion Science*, Vol.43, (2001): p.1417.
40. Zieba A., G. Sethuraman, F. Perez, G.H. Nancollas and D. Cameron, " Influence of organic Phosphonates on Hydroxyapatite crystal growth kinetics," *Langmuir*, 12, (1996): p. 2853.
41. Zielinski S., " Kinetic aspects of  $\text{CaSO}_4 \cdot 2\text{H}_2\text{O}$  crystallization in wet-phosphoric acid process," *Scientific papers of the institute of Inorganic Technology*, Monographs No. 20, Technical university of Wroclaw, Poland. (1981).

### APPENDIX A: METHOD OF ADDITION OF Fe<sup>++</sup>

1. Deionized water (DI water) (100mL) was deoxygenated in a small beaker for forty minutes.
2. 1.78 g FeCl<sub>2</sub>.4H<sub>2</sub>O was weighed in a weighing dish.
3. FeCl<sub>2</sub> was added into the deoxygenated DI water.
4. After FeCl<sub>2</sub> was dissolved, the required amount of solution was removed out of the glass cell using a syringe and was added to the test solution by piercing the needle through the septum on the glass cell.
5. The amount of iron chloride solution added to the test solution to achieve a required concentration of Fe<sup>++</sup>, when 1.78 gm of FeCl<sub>2</sub>.4H<sub>2</sub>O is dissolved in 100 ml deoxygenated solution is given by the equation:

$$V(ml) = \frac{[Fe^{++}] * V_{Total} * 100 \left( \frac{M * l * ml}{Mol} \right)}{\left( \frac{W}{MW} \right)_{FeCl_2.4H_2O}} \quad (A-1)$$

where,

V is the volume needed to add in the test solution, V<sub>Total</sub> is the total volume of the test solution, in liters (2 l), W is the weight of FeCl<sub>2</sub>.4H<sub>2</sub>O added, in grams (1.78g), MW is the Molecular weight of FeCl<sub>2</sub>.4H<sub>2</sub>O. (198)

Simplifying the above equation, we get

$$V(ml) = \frac{Fe^{++} (ppm)}{MW_{Fe^{++}} * 1000} * \frac{V_{Total} (l) * 100(ml)}{\left( \frac{W}{MW} \right)_{FeCl_2.4H_2O}} \quad (A-2)$$

Substituting the known values, we get

$$V(ml) = \frac{Fe^{++}(ppm)}{56 * 1000} * \frac{2(l) * 100(ml)}{\left(\frac{1.78}{198}\right)_{FeCl_2.4H_2O}} \quad (A-3)$$

Hence, from the above equation, if a concentration of 50 ppm of  $Fe^{++}$ , is needed, a volume of 20 ml of the prepared  $FeCl_2.4H_2O$  solution is needed to be added.

6.  $FeCl_2.4H_2O$  solution was always added before the metal sample was inserted in the solution.

### APPENDIX B: TAFEL SLOPE ANALYSIS

The anodic and cathodic Tafel slopes  $\beta_a$  and  $\beta_c$  are the function of temperature. They can be expressed as:

$$\beta_a = \frac{2.303RT}{\alpha_a F} \quad (\text{B-1})$$

$$\beta_c = \frac{2.303RT}{\alpha_c F} \quad (\text{B-2})$$

where,

T is Absolute temperature in K, R is the universal gas constant (8.314 J/mol K),  $\alpha_a$  and  $\alpha_c$  are the symmetry factors for anodic and cathodic reaction. The values of  $\alpha_a$  and  $\alpha_c$  are typically 1.5 and 0.5 respectively. F is Faraday's constant (96,500 coulombs/equivalent).

From the above equations the 'B' value can be calculated by using the following expression:

$$B = \frac{\beta_a \beta_c}{2.303(\beta_a + \beta_c)} \quad (\text{B-3})$$

From the above equations (B-1, B-2, B-3), the average value of the 'B' value (B) in the temperature range of 20 °C - 100 °C was calculated to be 14.3 mV.

After the formation of a inhibitor film or a iron carbonate scale, the cathodic reaction might become diffusion- controlled. Hence, under those conditions the cathodic tafel slope ( $\beta_c$ ) could be assumed to become infinite. This is not strictly speaking correct, however a more rigorous analysis leads to the same result. Therefore, by substituting the above value of  $\beta_c$  as infinity in the equation (B-3) and evaluating the 'B' value in the temperature range of 20 °C - 100 °C, the constant was calculated to be 19.1 mV.

Since, the under actual test conditions there would be film-forming as well as non film-forming conditions, an average value of the 'B' value was taken. The average value was found to be 16.7 mV.

The 'B' value for inhibitor A and inhibitor B, measured with the help of potentiodynamic sweeps were 16.4 mV and 17.36 mV respectively. Hence, a value of 17 mV was taken for all the LPR experiments for calculating the corrosion rate.

### APPENDIX C: CORROSION RATE MEASUREMENT

The corrosion rate was monitored using the linear polarization resistance (LPR) technique. From the basic electrochemical theory, the corrosion current density  $i_{corr}$  ( $A/m^2$ ) can be described as:

$$i_{corr} = B \times \frac{1}{R_p} \times \frac{1}{A} \quad (C-1)$$

where,

B is the 'B' value (explained in Appendix B),  $R_p$  is the corrosion resistance in Ohm, A is the working electrode surface area in  $m^2$ .

The corrosion rate (CR) in mm/yr can then be calculated according to the following equation:

$$CR = \frac{m}{At\rho} = \frac{i_{corr}M_w}{\rho nF} = 1.16i_{corr} \quad (C-2)$$

where,

m is the metal loss in kg, t is the time in seconds,  $\rho$  is the density of the material in  $kg/m^3$ ,  $M_w$  is the molecular weight of iron, F is the Faraday constant, n is the number of electrons exchanged in the electrochemical reaction.

## APPENDIX D: EXPERIMENTAL UNCERTAINTY ANALYSIS

### D.1 Uncertainty in the corrosion rate measurement due to the type of instrumentation.

The factors that affect the accuracy of the LPR corrosion rate measurements include temperature, applied current, applied potential and the working electrode area.

According to the Appendix C, corrosion rate can be written as,

$$CR = 1.16i_{corr} \quad (D-1)$$

where corrosion rate (CR) is expressed in mm/yr, and  $i_{corr}$  is in A/m<sup>2</sup>

Substituting (C-1) and (B-3) into (D-1) we get,

$$CR = 0.505 \frac{\beta_a \beta_c}{(\beta_a + \beta_c)} \times \frac{1}{R_p} \quad (D-2)$$

Since,  $\beta_a$  and  $\beta_c$  are only dependent on temperature and vary linearly with temperature (Equation B-1, B-2), they can be rewritten as the following equations:

$$\beta_a = \beta_{a0} + m_1 T \quad (D-3)$$

$$\beta_c = \beta_{c0} + m_2 T \quad (D-4)$$

where,  $\beta_{a0}$  and  $\beta_{c0}$  are the base anodic and cathodic Tafel constant at a suitable reference temperature. The slope  $m_1$  and  $m_2$  can be easily obtained by plotting the equation (B-1) and (B-2). The values obtained are  $m_1 = 0.14$  mV/K and  $m_2 = -0.4$  mV/K.

In equation (D-2),  $R_p$  can be expressed as follows:

$$R_p = \frac{dE}{di_{app}} \quad (D-5)$$

where,  $i_{app}$  is the applied current density in A/m<sup>2</sup>

$$i_{app} = \frac{I_{app}}{a} \quad (D-6)$$

where,  $I_{app}$  is the applied current in A and  $a$  is the working area in  $cm^2$

Substituting equation (D-3) to (D-6) in equation (D-2), we get

$$CR = 0.505 \frac{(\beta_{a0} + m_1 T)(\beta_{c0} + m_2 T)}{\beta_{a0} + \beta_{c0} + (m_1 + m_2)T} \times \frac{\Delta I_{app}}{\Delta E \Delta a} \quad (D-7)$$

Above equation can then be written in the following form:

$$CR = 0.505(\beta_{a0} + m_1 T)(\beta_{c0} + m_2 T)[\beta_{a0} + \beta_{c0} + (m_1 + m_2)T](\Delta I_{app})(\Delta E)^{-1}(\Delta a)^{-1} \quad (D-8)$$

The sensitivity of small changes in the corrosion rate to small changes in each variable is expressed by taking partial derivatives of the corrosion rate with respect to each variable. The errors in  $\beta_{a0}$ ,  $\beta_{c0}$ ,  $m_1$  and  $m_2$  are assumed to be negligible. Thus, the absolute uncertainty in the measurement of corrosion rate because of uncertainties in the system variables can be expressed as follows:

$$\frac{\delta(CR)}{CR} = \left[ \frac{\partial(CR)}{\partial T} \right] \frac{\delta T}{CR} + 2 \left[ \frac{\partial(CR)}{\partial E} \right] \frac{\delta E}{CR} + 2 \left[ \frac{\partial(CR)}{\partial I_{app}} \right] \frac{\delta I_{app}}{CR} + 2 \left[ \frac{\partial(CR)}{\partial a} \right] \frac{\delta a}{CR} \quad (D-9)$$

Deriving the partial derivatives of each item above according to equation (D-8) and then substituting into (D-9), the following equation is obtained:

$$\frac{\delta(CR)}{CR} = \left( \frac{m_1}{\beta_a} + \frac{m_2}{\beta_c} \right) \delta T - \frac{2}{E} \delta E + \frac{2}{I_{app}} \delta I_{app} - \frac{2}{a} \delta a \quad (D-10)$$

Therefore, the corrosion rate uncertainty above can be considered an overall uncertainty through the experiment for LPR technique. It considers the uncertainties due to the temperature, due to instrumentation (potential and applied current), and due the working electrode surface area. The contribution of each item in (D-10) to the corrosion rate uncertainty measurements is calculated as follows:

### *Temperature*

The temperature during the experiment was maintained at  $80\text{ }^{\circ}\text{C} \pm 2.2\text{ }^{\circ}\text{C}$ , thus  $\delta T=1$ . Tafel slopes calculated at  $80\text{ }^{\circ}\text{C}$  are,  $\beta_a = 46\text{ mV}$  and  $\beta_c = 140\text{ mV}$ . Hence the first part on the right hand side of the equation (D-10) is:

$$\left( \frac{m_1}{\beta_a} + \frac{m_2}{\beta_c} \right) \delta T = \left( \frac{0.14}{46} + \frac{-0.4}{140} \right) \times 2.2 = 4.09 \times 10^{-4} \quad (\text{D-11})$$

### *Potential*

According to Gamry, the DC accuracy in voltage measurement is  $\pm 0.3\%$  range  $\pm 1\text{ mV}$ . During the experiment, the applied potential was  $\pm 5\text{ mV}$  over the open circuit potential. Thus the uncertainty in the potential would be  $\delta E = 1.03\text{ mV}$ . The error in the potential could be different for measurements before and after formation of the iron carbonate scale or the inhibitor film. Before the formation of the scale, the  $R_p$  was determined over the entire applied potential since there was a linear relationship between the potential and the current, as shown in Figure 61. Hence, the absolute uncertainty due to the potential in equation (D-10) can be described as:

$$\frac{2}{E} \delta E = \frac{2}{10} \times 1.03 = 0.206 \quad (\text{D-11})$$

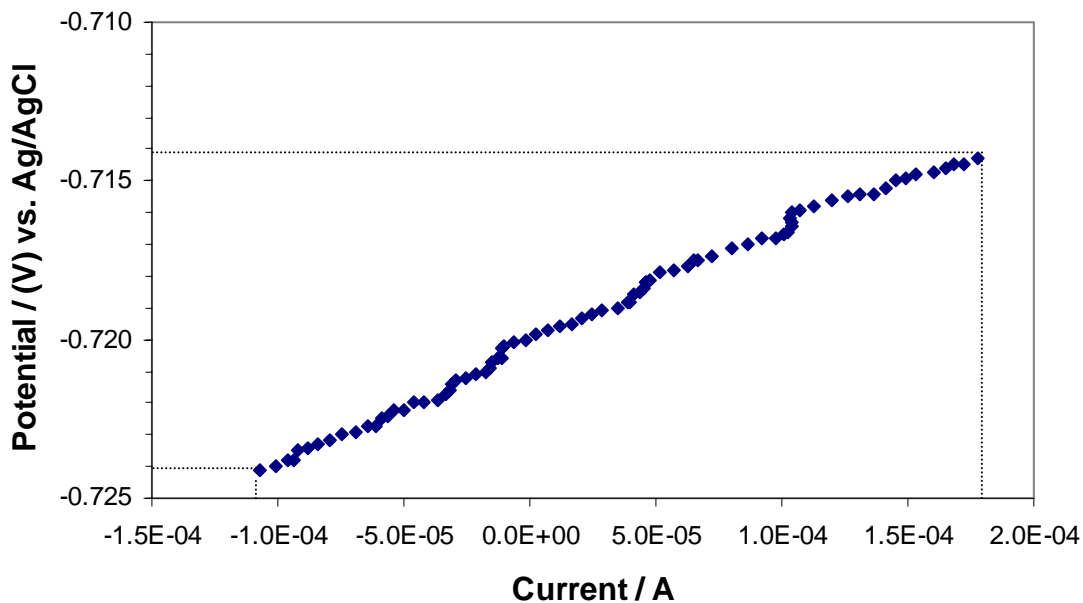


Figure 61. A typical linear polarization curve obtained in experiments before scale formation

However, after the scale or inhibitor film was formed on the metal surface, the linear relationship did not exist over the entire applied potential, as indicated in Figure 62. The actual potential used to get the  $R_p$  was only taken from the linear region, which was a 6 mV range. Thus the absolute uncertainty after the scale formation is:

$$\frac{2}{E} \delta E = \frac{2}{6} \times 1.03 = 0.343 \quad (\text{D-12})$$

Hence, depending on when the LPR was taken, the error due to the potential measurement should be somewhere in between with and without scale formation

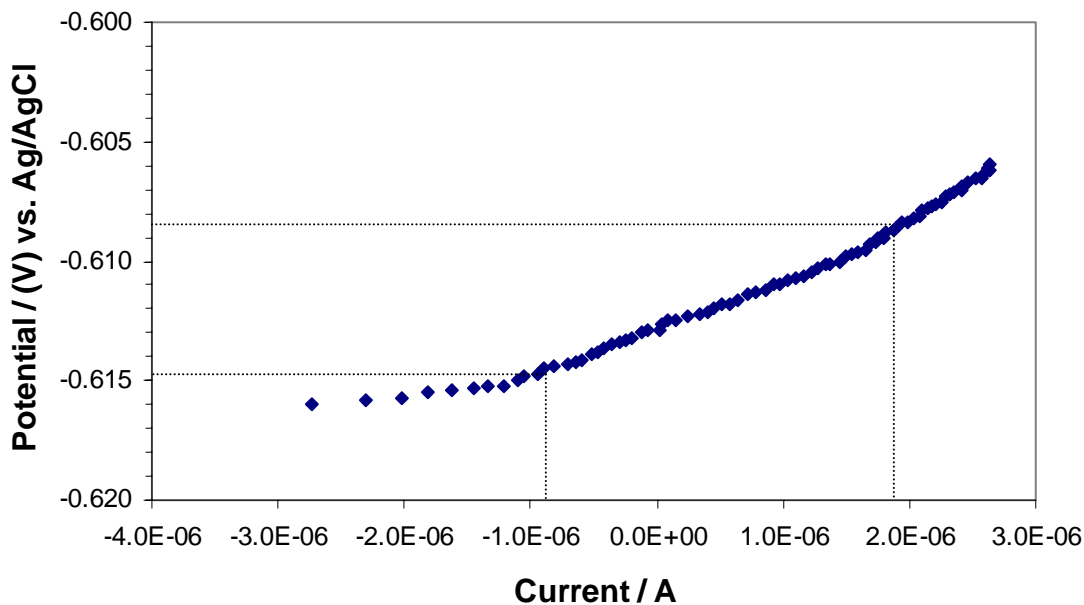


Figure 62. A typical linear polarization curve obtained in experiments after scale formation

### *Current*

According to Gamry, the DC accuracy in current measurement is  $\pm 0.3\%$  range  $\pm 50$  pA. The current range was different for different experiments, and varied with time because of the change in the corrosion rate. During the start of the experiment, the applied current range is usually around  $400 \mu\text{A}$ . Thus the uncertainty in the current would be:

$$\delta I_{app} = 4 \times 10^{-4} \times 0.003 = 1.2 \times 10^{-6} \text{ A} \quad (\text{D-13})$$

Hence, the absolute uncertainty in the equation (D-10), due to the current would be:

$$\frac{2}{I_{app}} \delta I_{app} = \frac{2}{4 \times 10^{-4}} \times 1.2 \times 10^{-6} = 6.0 \times 10^{-3} \quad (\text{D-14})$$

After the formation of the scale or the inhibitor film, since the corrosion rate reduced, the applied current was reduced to about 4  $\mu\text{A}$ . Thus the uncertainty in the current would be:

$$\delta I_{app} = 1.2 \times 10^{-8} \text{ A} \quad (\text{D-15})$$

Hence, the absolute uncertainty in the equation (D-10), due to the current would be:

$$\frac{2}{I_{app}} \delta I_{app} = \frac{2}{4 \times 10^{-6}} \times 1.2 \times 10^{-8} = 6.0 \times 10^{-3} \quad (\text{D-16})$$

Hence, from the above equation, the error in corrosion rate due to the current is found out.

### *Electrode Area*

The uncertainty in the area was due to the accuracy of the measuring instrument, the loss of area due to the polishing of the sample and corrosion loss of the reused sample. It was estimated to be 0.01  $\text{cm}^2$ . Therefore, the absolute uncertainty due to the surface area in equation (D-10) is:

$$\frac{2}{a} \delta a = \frac{2}{5.4} \times 0.01 = 3.7 \times 10^{-3} \quad (\text{D-17})$$

Thus the uncertainties in the corrosion rate measurement from the LPR technique for the specified experiment are expressed as:

$$\frac{\delta(CR)}{CR} = \pm \left( 4.09 \times 10^{-4} - \frac{0.206 + 0.343}{2} + 6.0 \times 10^{-3} - 3.7 \times 10^{-3} \right) = \pm 27.2\% \quad (\text{D-18})$$

From the above equations, it can be concluded that in the LPR measurement technique, the uncertainty in the potential is a major source of error in corrosion rate. The error calculated in equation (D-18) would be the average error over entire length of the experiment. Hence, at the beginning of the experiment, the error could be about 20% while, towards the end of the experiment, after formation of the iron carbonate scale or the inhibitor film the error could be 34%.

## D.2 Uncertainty in the corrosion rate measurement due to initial conditions

Error in the initial conditions, like pH and  $Fe^{++}$  concentrations could have an effect on the precipitation rate of iron carbonate. Since corrosion is affected by the precipitation of the scale, this could lead to uncertainty in the corrosion rate.

The uncertainty in the added  $Fe^{++}$  concentration is due to the error associated with the syringe. The syringe used to inject  $Fe^{++}$  has an accuracy of  $\pm 0.1$  ml. Since the least amount of  $Fe^{++}$  used for an experiment was 4 ml, the absolute error due to  $Fe^{++}$  is given by:

$$\frac{\delta Fe}{Fe} = \frac{0.1}{4} = 0.025 \quad (D-19)$$

The pH meter has an accuracy of  $\pm 0.01$  pH units. At a pH of 6.60, a change in the pH by  $\pm 0.01$  units could cause a change in the  $CO_3^{2-}$  ion concentration by  $\pm 0.0004$  M. Since at pH 6.60, the  $CO_3^{2-}$  ion concentration is 0.0178 M, the absolute error due to the pH meter is given by:

$$\frac{\delta CO_3^{2-}}{CO_3^{2-}} = \frac{0.0004}{0.0178} = 0.022 \quad (D-20)$$

The error caused in the measurement of the pH meter ( $\text{CO}_3^{2-}$  ion concentration) and the  $\text{Fe}^{++}$  concentration, leads to the uncertainty in the supersaturation (SS). Supersaturation is related to  $\text{Fe}^{++}$  concentration and  $\text{CO}_3^{2-}$  ion concentration by equation (2-10). If the error in solubility product due to the temperature is negligible, the uncertainty in the supersaturation can be found out by the following equation:

$$\frac{\delta(SS)}{SS} = \frac{\delta Fe}{Fe} + \frac{\delta \text{CO}_3^{2-}}{\text{CO}_3^{2-}} = 0.025 + 0.022 = 0.047 \quad (\text{D-21})$$

The supersaturation was varied from 7 – 150. Hence, the errors at different supersaturations are as follows:

$$\text{At SS} = 7, \delta(SS) = 0.047 * 7 = 0.32$$

$$\text{At SS} = 30, \delta(SS) = 0.047 * 30 = 1.41$$

$$\text{At SS} = 150, \delta(SS) = 0.047 * 150 = 7.05$$

This error in the supersaturation could affect the precipitation rate that in turn affects the corrosion rate. However, there is no explicit equation showing the relation between precipitation rate and the corrosion rates. Due to this implicit error, the uncertainty in the corrosion rates for the precipitation experiments could be more than that calculated from the Appendix D.1.

### D.3 Comparison of the experimental and the calculated error

The absolute error of the experiments shown in Figure 18 and Figure 23, is calculated and compared to the error calculated in appendix D.1. The comparison is shown in Figure 63 and Figure 64. From the graphs, it is seen that as calculated, before

the formation of the scale, the experimental error is similar to the calculated error. However, after the scale is formed, the experimental error jumps about 2-3 times the calculated error. High error in the experiments, after scale formation was an implicit error due to uncertainty in the initial conditions that lead to error in the precipitation rate. This was discussed in the Appendix D.2.

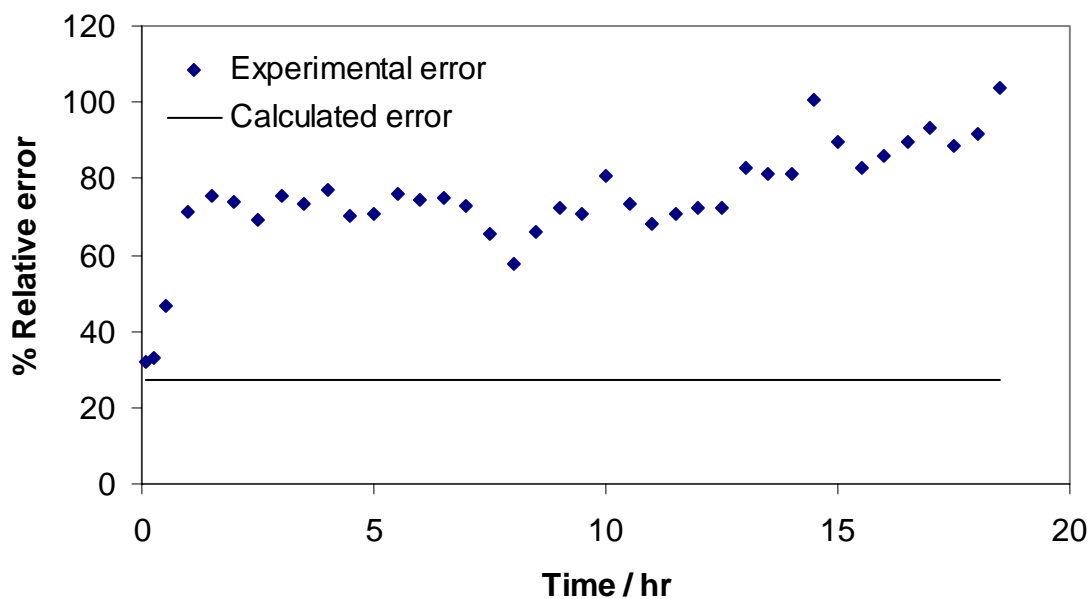


Figure 63. Comparison of the calculated and the experimental error at supersaturation of 150 and  $T = 80$  °C.

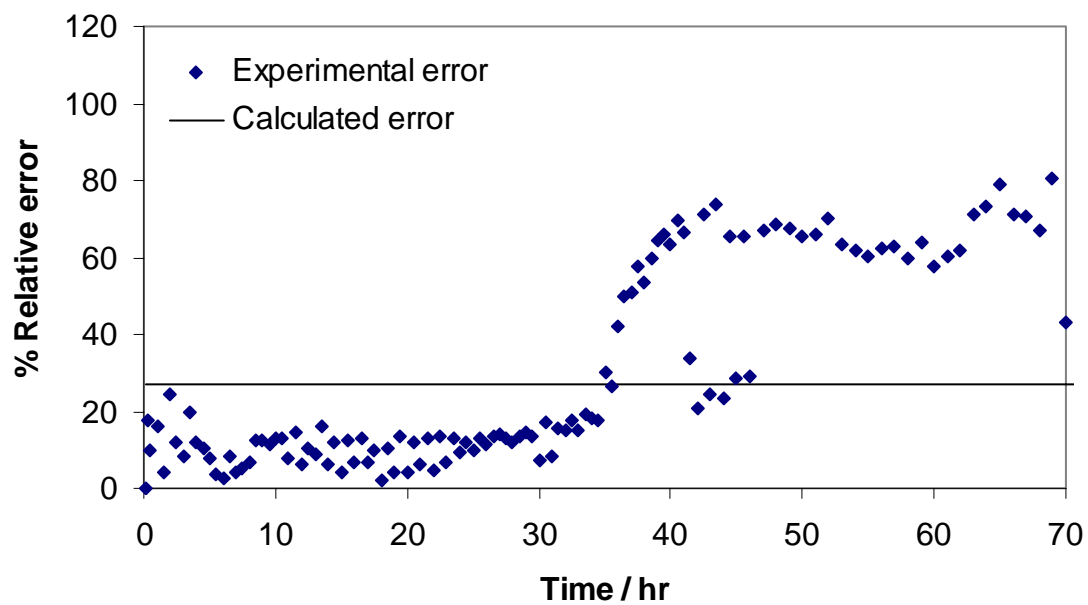


Figure 64. Comparison of the calculated and the experimental error at supersaturation of 30 and  $T = 80\text{ }^{\circ}\text{C}$ .